January 2010

Electrical And Magnetic Separation Of Particles

Lin Li
Washington University in St. Louis

WASHINGTON UNIVERSITY IN ST. LOUIS

School of Engineering and Applied Science

Department of Energy, Environmental & Chemical Engineering

Dissertation Examination Committee:
Da-Ren Chen, Advisor, Chair
Richard Axelbaum
Pratim Biswas
Jay Turner
Younan Xia
Lan Yang

ELECTRICAL AND MAGNETIC SEPARATION OF PARTICLES

by

Lin Li

A dissertation presented to the
Graduate School of Arts and Sciences
of Washington University in
partial fulfillment of the
requirements for the degree
of Doctor of Philosophy

December 2010

Saint Louis, Missouri

Abstract

Electrical and Magnetic Separation of Particles

by

Lin Li

Doctor of Philosophy in Energy, Environmental, & Chemical Engineering

Washington University in St. Louis, 2010

Professor Da-Ren Chen, Advisor

Particle separation technologies have been utilized in many industrial fields, such as pigment and filler production, mineral processing, environmental protection, the food and beverage industry, and the chemical industry, as well as in biomedical application, such as cell biology, molecular genetics, biotechnological production, clinical diagnostics, and therapeutics. A lot of particle separation technologies using various mechanics in terms of the differences in the physical or physico-chemical properties of the particles have been developed. Among these categories, electrical and magnetic separations are of great interest in recent researches. The overall objective of this dissertation is to advance our current knowledge on these two particle separation technologies. Accordingly, it has two major parts: (1) Charge Conditioning for Particle Separation, and (2) Magnetic Filtering for Particle Separation. In the first part, a new DC-corona-based charge conditioner for critical control of electrical charges on particles and a UV aerosol charger for fundamental investigation particle photocharging process were developed. The chargers' performances including charging efficiencies and charge

distributions were evaluated upon different operational conditions such as aerosol flow rates, corona operations, and ion-driving voltages for the charge conditioner, particle material and irradiation intensity for the UV charger. The birth-and-death charging model with the Fuchs limiting sphere theory for calculating the ion-particle combination coefficient was applied to obtain the charging ion concentration inside the charge conditioner. The UV charging model with the photoemission rely on the Fowler-Nordheim law was applied to predict the charging performance of the UV charger. In the second part, a magnetic filter system has been constructed, and its performance has been investigated. To retrieve the magnetic property of characterized particles from the measured penetration data, a numerical model was further developed using the finite element package COMSOL Multiphysics 3.5. The numerical model was first validated by comparing the experimental penetration with the simulation results for the cases of 100, 150, and 250 nm γ-Fe_2O_3 particles having the magnetic susceptibility characterized by Vibrating Sample Magnetometer (VSM). The magnetic susceptibilities of other sizes from 100 to 300 nm were then derived from this model according to the measured penetration data. To control or remove the lunar dust through a magnetic approach, eight samples (three JSC-1A series lunar dust simulants, two NU-LHT series lunar dust simulants, and three minerals) in the size range from 150 to 450 nm were characterized. Magnetic susceptibilities were obtained from the difference in particle penetration through magnetic mesh filters with and without an applied external magnetic field.

Acknowledgement

I wish to express my sincere appreciation to my advisor, Professor Da-Ren Chen, for his excellent guidance and never-ending support. His encouragement of independent thinking, his advice and patience were always invaluable and inspirational. I would like to acknowledge members of my committee, Dr. Pratim Biswas, Dr. Richard L. Axelbaum, Dr. Jay R. Turner, Dr. Younan Xia, and Dr. Lan Yang for taking an interest in my work, examining my dissertation, and providing useful comments.

I would like to thank all members and alumni in the Particle Nanotechnology Lab, Weiling Li, Chaolong Qi, Fan Mei, Ta-Chih Hsiao, Huijing Fu, Marit Meyer, Yi-Hsuan Lee, and my colleagues in the Department of Energy, Environmental and Chemical Engineering for their assistance and discussions. I am very grateful to Dr. Anup K. Gangopadhyay for valuable discussion on magnetic property measurement and for helping me to obtain data from my samples. Financial support from the Charles Buescher Jr. Scholarship and NASA are gratefully acknowledged. Many thanks go to the department staff, Kim Coleman, Rose Baxter, Patricia Wurm, Beth Mehringer, Mindy Price, and Trisha Sutton for their consistent assistance.

Finally, my genuine gratitude goes to my parents, and my wife, Huijing Fu, for their support during my study and research at Washington University. I am especially grateful to my wife, since without her companionship, support and encouragement, this work could not be completed.

Dedicated to my parents, Guoqiang Li and Cuiying Dong,

my wife, Huijing Fu, and my approaching daughter.

Table of Contents

List of Figures

List of Tables

Chapter 1

Introduction and Overview

1.1 Introduction to Particle Separation Technology

Separation processes are widely used in the petroleum, chemical, forest, pharmaceutical, mineral, and materials processing industries, where physical or chemical forces are applied to isolate the selected substances from a mixture. In fact, it is difficult to find any important engineering corporation that does not use them. Base on the energy analysis by the Department of Energy (DOE ITP Report, 2005), separation technologies account for approximately 4,500 trillion Btu/yr, about 14% of energy use in the industrial sector, which is over one-third of the total energy consumption in the United States in 2001. Furthermore, 40% to 70% of capital and operating costs in industry are from separation processes every year (Legault and Rivero, 2008). Hence, improvement on separation technologies is essential to energy saving, to operating expenses, and consequently to corporate profitability of related industries. Moreover, the application and improvement of existing separation technologies, as well as the development of novel techniques, are necessary to meet the requirement in new environments such as biomedicine and electronics (Rousseau, 1987).

Based on the phase of the mixture, separation can be categorized into separation of homogeneous solids, liquids, gases, or supercritical fluids, and separation of heterogeneous systems containing any combination (Lu et al., 2005). For instance, mass transfer operations in the liquid phase, such as absorption, distillation, and extraction, are typical examples of separation of homogeneous mixtures. The separation processes of heterogeneous mixtures, such as sedimentation and filtration to remove the solid particles suspended in the fluid, perhaps are even more commonly encountered everywhere.

As particles become key technological components in many modern industrial applications and fundamental research, purification and separation of particles according to their physical or chemical properties are constantly needed. The solid-particle separation methods can be further classified into two major groups (Lu et al., 2005): (1) solid-liquid or solid-gas separation, in which suspended particles are removed, separated, or concentrated from the mixture, and (2) solid-solid separation, where particles are separated according to the differences in the physical or physico-chemical characteristics, such as size, shape, density, electrical or magnetic properties, surface wettability or the solubility of particles, etc.

Based on their separation mechanisms, particle separation techniques can be distinguished as sedimentation (settling, flocculation, and centrifuge), inertial deposition (cyclone, scrubber, impingement, and impactor), Brownian diffusion (diffusion batteries), particle migration in an electric or magnetic field (electrostatic precipitator, dynamic mobility analyzer, magnetic separator), thermophoresis (thermal precipitator), filtration (filter and membrane for particle collection by combined mechanisms), and others. Among all these categories, electrical and magnetic separations are of great interest in recent research. These two methods have higher resolution and efficiency than others in particle separation processes. For example, monodisperse particles can be achieved through a classification process using a differential mobility analyszer (DMA) as an electrical separator. A magnetic separator can be considered as a plus to traditional filtration, in which the attractive magnetic force between particle and filter fiber play an important role in addition to the inertial impaction, diffusion, and interception in particle

filtration process. Moreover, magnetism and electricity are closely related and regarded by physicists as two expressions of a single force, called "electromagnetism".

The overall objective of this dissertation is to advance our current knowledge on these two particle separation technologies: electrical and magnetic. Accordingly, it has two major parts: (1) Charge Conditioning for Particle Separation, and (2) Magnetic Filtering for Particle Separation. The motivation for each part is explained in the following sections.

1.2 PART I: Charge Conditioning for Particle Separation

Electrically charged particles, especially for particles in submicrometer and nanometer size ranges, are often required in many aerosol studies and applications. Examples of applications via charged particles are the synthesis of unagglomerate particles (Adachi et al., 2003; Jiang et al., 2007a), particle separation and removal (Parker, 1997), particle collection (Cheng et.al., 1981), enhanced particle dispersion (Mazumder et. al., 2007), structured patterning (Jacobs and Whitesides, 2001; Fissan et al., 2003; Kim et al., 2006), micro-contamination control (Zhuang et al., 2000), and particle instrumentation (Keskinen et. al., 1992; Chen et al., 1998; Kaufman et. al., 2002; Friedlander and Pui, 2003; Shin et. al., 2007; Wang et. al., 2010). Particle deposition in the human lung was also found to be dramatically enhanced by electrical charges on particles (Melandri et al., 1983; Yu, 1985; Cohen et al., 1995, 1998). Using inhalation for rapid drug absorption in the lung and subsequently systemic transport to secondary body organs can be efficiently achieved by the administration of charged aerosol medications. To condition electrical charges on particles for making the previously mentioned

processes efficient, a particle charge conditioner, often called a particle charger, is necessary.

On the other hand, the charging efficiency of unipolar corona chargers decreases significantly for particles in the diameters less than 20 nm. To further improve the efficiency of charging nanoparticles, researchers have used direct irradiation methods such as Ultraviolet (UV) (Burtscher et al., 1982; Hontañón and Kruis, 2008; Jung et al., 1988; Kogelschatz, 1992; Matter et al., 1995; Maisels et al., 2003; Mohr et al., 1996, 1997) and soft x-ray irradiation for nanoparticle charging (Han et al., 2003; Jiang et al., 2007b; Kulkarni et al., 2002, Shimada et al., 2002). Different from ion diffusion chargers, the performance of photo chargers strongly depends upon the particle composition. For electron escape from the particle surface, the kinetic energy of escaping electrons must be greater than a given threshold, which is the function of the work function of both the particle material and the particle size. Note that most of previous UV charging studies were focused on metal particles, auto exhaust particulate, and atmospheric aerosol. For the general application of aerosol photocharging, it is thus important to investigate its applicability for particles made of other materials, for example, organics, salts, and metal oxides. Further, after passing through a UV charger, limited particle charge distribution data has been reported at the present. Finally, the verification of existing photocharging models in previous studies was primarily done by comparing the model results with the measured charge efficiency of UV chargers. More detailed comparison with particle charge distribution data is thus needed to confirm existing photocharging models.

For the first half of the dissertation, charge conditioning for particle separation, there are two major objectives:

1. To develop a unipolar corona charger with high charging efficiency and well-adjustable ion concentration for particle charge conditioning.
2. To investigate particle photocharging process, focusing on the effect of particle material and irradiation intensity.

1.3 PART II: Magnetic Filter for Particle Separation

Magnetic particles are of great interest in fundamental research and industrial applications. They are used in a wide range of applications in catalysis (Noronha et al., 1997), magneto-cooling (Roy et al., 1993), recording devices (Prinz, 1998), purification of enzymes and other biotical substances (Airapetyan et al., 2001), as well as water purification devices (Kobe et al., 2001). Many medical applications need submicron- and nanometer-sized magnetic particles (Hafeli et al., 1999) for drug delivery via biocompatible magnetic substances, cell separation, hyperthermia, cancer therapy, and aneurysm treatment, to name just a few examples.

Fine particles can also display different forms of magnetism (Young and Freedman, 2003): ferromagnetism, ferrimagnetism, paramagnetism, diamagnetism, and superparamagnetism, distinguished by the influence of the external magnetic field on their magnetic moment, which also depends on the raw material and the generation conditions. Additionally, in the size range from submicrometer down to nanometer, the magnetic properties change very strongly with particle diameter. One key characteristic of magnetic particles is the magnetic moment. Hence, the determination of the particles' magnetic moment is an important problem from both scientific and engineering point of view.

As NASA prepares for future exploration on the Moon, it must address many of the problems faced by the original Apollo astronauts. One major problem is controlling the lunar dust (<20 μm) that makes up a large portion of the lunar surface (~20 weight %). Most lunar dust (60 - 80%) is composed of broken pieces of agglutinitic glass, which contains abundant nanometer-sized metallic Fe grains (np-Fe^0) (Taylor et al., 2005). To control or remove the lunar dust, a magnetic approach has thus been proposed. To determine the feasibility of the proposed method, it is necessary to measure the magnetic properties of lunar dust and related simulants.

For the second half of the dissertation, magnetic filtering for particle separation, there are three objectives:

1. To develop a magnetic filter system for particle magnetic moment measurement.
2. To develop a numerical model to simulate the magnetic particle capture process in the magnetic filter.
3. To obtain the calibration curves for prototype system.
4. To measure the magnetic properties of lunar dust and related simulants.

1.4 Dissertation Structure

In addressing the two major components, the whole dissertation contains eight chapters. The first part, including chapters 2, 3 and 4, focuses on the design and evaluation of a unipolar corona charger and a UV charger. The second part, including chapters 5, 6, and 7, focuses on the performance and model of magnetic filter system. Brief descriptions of each chapter follow.

In chapter 1, an overview of particle control technologies and their needs, applications, and challenges is presented. A general introduction, background information, and research objectives for the charge conditioning and magnetic filtering for particle separation are given.

PART I:

In chapter 2, particle charging mechanics and several unipolar chargers developed in the past are reviewed and summarized. The review on the development of the corona chargers is followed by a description of the design of the new corona charger in this work. The review of the previous UV charger studies leads to the fundamental investigation of dependence the effect of particle material and irradiation intensity for particle photocharging.

In chapter 3, a new DC-corona-based charge conditioner was developed for the processes in which electrical charges on particles are critical to successful operations. The chargers performance is optimized under different operational conditions such as aerosol flow rates, corona operations, and ion-driving voltages. Charging efficiencies are measured and compared with the results from other corona discharge based unipolar chargers. A tandem-DMA technique was utilized to characterize extrinsic charge distributions of particles with various sizes. The birth-and-death charging model with the Fuchs limiting sphere theory for calculating the ion-particle combination coefficient was applied to obtain the charging ion concentration under the various operations of the prototype.

In chapter 4, an aerosol charger utilizing pen-type Hg lamps was constructed to investigate the fundamental process of particle charging under UV irradiation. The

performance of the prototype UV charger at 5 lpm flow rate with four UV lamps was evaluated using monodisperse silver (Ag) and various metal oxide particles with diameters ranging from 7 to 30 nm and from 50 to 200 nm, respectively. To evaluate the effect of irradiation intensity on particle photocharging, the charging efficiencies and charge distributions for Ag particles ranging from 7 to 30 nm were characterized when the prototype was operated at an aerosol flow rate of 5 lpm for the cases of one, two, and four lamps turned on. The UV charging model with the photoemission based on the Fowler-Nordheim law was further applied to predict the charging performance of the UV charger at different operational conditions.

PART II:

In chapter 5, a few characterization techniques of particle magnetic moment are reviewed and summarized. Concepts and methods are applied to analyze and model our experimental data on magnetic filters.

In chapter 6, a magnetic filter system has been constructed, and its performance has been investigated. The particle concentrations upstream and downstream of the magnetic filter element were measured by an Ultrafine Condensation Particle Counter (UCPC, TSI model 3025A). To retrieve the magnetic property of characterized particles from the measured penetration data, a numerical model was further developed using the finite element package COMSOL Multiphysics 3.5. The numerical model was first validated by comparing the experimental penetration with the simulation results for the cases of 100, 150, and 250 nm γ-Fe_2O_3 particles having the magnetic susceptibility characterized by a Vibrating Sample Magnetometer (VSM). The magnetic susceptibilities

of other sizes from 100 to 300 nm were then derived from this model according to the measured penetration data.

In chapter 7, to investigate the control or removal of lunar dust through a magnetic approach, eight samples (three JSC-1A series lunar dust simulants, two NU-LHT series lunar dust simulants, and three minerals) in the size range from 150 to 450 nm were characterized using the magnetic filter system described in chapter 6. Magnetic susceptibilities were obtained from the difference in particle penetration through magnetic mesh filters with and without an applied external magnetic field.

In chapter 8, the accomplishments of this dissertation are summarized, and the issues and challenges that deserve future research efforts are addressed.

Chapter 2

Review of Unipolar Chargers

2.1 Introduction

A variety of aerosol charging methods have been studied for different applications in the past three decades. The ion-attachment method and the photo-ionization method are the two main approaches used for charging particles (Chen and Pui, 1999), and both charging processes can be modeled and predicted (Fuchs, 1963; Maisels et al. 2002). The former charges particles by random collisions with ions in an ion-rich environment. The latter ionizes particles using photons emitted from UV or soft X-ray light sources.

The ion-attachment method attaches ions on particles by using field or diffusion charging processes. Field charging is the dominant mechanism for particles larger than 1.0 μm, and diffusion charging is the dominant mechanism for particles less than 0.1 μm, even in the presence of an electric field (Hinds, 1999).

In the diffusion charging process, particles can be exposed to either bipolar or unipolar ion environments to accomplish various charging tasks required by applications (Marquard et. al., 2006a, 2006b). Several bipolar chargers have been studied, with bipolar ions usually produced by radioactive decay of isotope, such as Kr^{85} or Po^{210} in Scanning Mobility Particle Sizer (SMPS, TSI model 3936, Wang and Flagan, 1990), by corona discharge, such as an AC corona with a sonic jet (Stommel and Riebel, 2005) and dual electrode corona (Romay et al., 1994), or by soft X-rays (Shimada et al., 2002). In all the bipolar chargers, the neutral particles can acquire charge while the charged particles may discharge themselves by capturing ions of the opposite polarity (Pui et al., 1988). This feature makes bipolar chargers more suitable for applications that require the neutralization of highly charged particles. However, because of the competition of the two processes, as described earlier, the bipolar chargers give very low charging efficiency

for nanoparticles, which limits their applications in aerosol processes (Adachi et al., 1985; Reischl et al., 1996). In general, charging particles by unipolar ions offers higher charging efficiency than by bipolar ions, especially for particles in submicrometer and nanometer sizes.

2.2 Review of Corona Chargers

Unipolar particle chargers can in general be classified into two types based on the sources of unipolar ions. One type of charger obtains unipolar ions through the separation of bipolar ions, often produced by either radioactive or soft X-ray sources via the use of a designed DC-electrical field. Recently, however, the use of these irradiation sources is undesirable because of more and more stringent safety regulations, and increasing license costs for the source usage. The other type of charger utilizes corona discharge to directly generate unipolar ions. For general applications, it is not recommended to pass aerosol through the corona-discharge zone (Stommel & Riebel, 2005). Instead, unipolar ions are often directed to the charging zone in an aerosol charger by either a sonic jet flow or a weak electric field (i.e, ion-driving voltage). Examples of chargers using the ion-driving electrical field are the EAA (Electrical Aerosol Analyzer) charger (Liu & Pui, 1977), the miniature aerosol charger for a personal particle sizer (Qi et al., 2008), and Hewitt-type chargers (Büscher et al., 1994; Kruis & Fissan, 2001; Biskos et al., 2005). The perpendicular arrangement in the directions of ion-driving electrical and aerosol flow fields, however, leads to serious electrostatic loss once nanoparticles are electrically charged (Chen & Pui, 1999). Marquard et al. (2006b) further concluded that chargers employing an AC electrical field to bring ions in contact with particles do not generally

improve the compromise between the charging efficiency and electrostatic loss for nanoparticles. Whitby (1961) first introduced the concept of applying a sonic jet flow to direct unipolar ions out from the corona discharge zone in the development of an ion generator. Medved et al. (2000) used a similar principle in the design of a unipolar charger, which was later modified and used in the Electrical Aerosol Detector (EAD, TSI model 3070A; Kaufman et. al., 2002) and Nanoparticle Surface Area Monitor (NSAM, TSI model 3550; shin et. al., 2007). The issue of particle loss in ion-particle flow mixing was often encountered in these chargers. With careful flow mixing arrangement, Qi et al (2007) recently investigated a DC-corona-based, mixing-type unipolar aerosol charger. As a result, Qi's charger provides higher extrinsic charging efficiency than other existing corona-based unipolar chargers. The control of ion concentration in the charging zone proved difficult in Qi's chargers. It was further found for Qi's charger that the extrinsic charging efficiency via negative ions is much lower than that via positive ions. This is because of the high electrical mobility of negative ions and a much smaller opening of orifice nozzles used for ion jets in Qi's charger.

In addition to the charging efficiency for nanoparticles, the issue of overcharge for large particles in unipolar chargers has not been substantially addressed in the literature. Particles larger than 20 nm in diameter can easily acquire more than one charge in a unipolar charger. Multiple charges on particles influence the precision of particle separation based on the electrical mobility of particles. The potential breakup of highly-charged, liquid droplets may be a disadvantage for some particle applications. Vivas et al. (2008) optimized the performance of an existing corona diffusion charger (Büscher et al., 1994) with the objective of reducing multiple charges on submicrometer particles. A

positive-zero rectangular-wave voltage was applied to the inner electrode of the charger, and the charging ion concentration was controlled by changing the duty cycle of pulsed voltage. In addition to more electrostatic loss for charged nanoparticles, the spatial and temporal variation of ion concentration in the charging region made it difficult to estimate the charging efficiency and charge distribution of particles through the unipolar charger. Moreover, multiple charges on particles with diameters less than 20 nm are often encountered in other processes, for example, electrospray ionization. Severe particle loss due to the space charge effect of highly charged particles is experienced during aerosol transport. The conditioning of charges on particles is often needed in the above described scenarios. Laschober et al. (2006) used a DC-corona-based, unipolar charging unit to minimize loss of highly charged particle produced by a commercial electrospray aerosol generator (TSI, model 3480) for particles with sizes ranging from 5 to 18 nm. At the optimal corona discharge settings, the yield of singly charged particles by the charge conditioning process was found to be two to four times higher in concentration than those of bipolar charging units.

2.3 Review of UV Chargers

Diffusion charging has been predominantly used for nanoparticle charging, as the charging dynamics can be accurately predicted by the Fuchs limiting sphere theory (Fuchs, 1963). However, the extrinsic charging efficiency of existing unipolar chargers significantly decreases as the particle size reduces, especially for particles with diameters less than 20 nm (Chen and Pui, 1999).

To further improve the efficiency of charging nanoparticles, researchers have used direct irradiation methods such as Ultraviolet (UV) (Burtscher et al., 1982; Hontañón and Kruis, 2008; Jung et al., 1988; Kogelschatz, 1992; Matter et al., 1995; Maisels et al., 2003; Mohr et al., 1996, 1997) and soft x-ray irradiation for nanoparticle charging (Han et al., 2003; Jiang et al., 2007b; Kulkarni et al., 2002, Shimada et al., 2002). Under UV exposure, electrons can be emitted from the particle surface once irradiated, and irradiated particles thus become positively charged if the incident photon energy exceeds the particle work function potential barrier. In soft-X-ray irradiation, carrier gas molecules can be further ionized in addition to direct photoionization due to the high incident photon energy (~10^3 eV). As a result, diffusion charging rates are enhanced in soft-X-ray irradiation when compared to UV irradiation (~5 eV). However, the high cost and limited lifetime of soft X-ray light sources make them not widely used.

Schmidt-Ott and Siegmann (1978) investigated photoemission from small particles suspended in a gas due to the irradiation of UV light. Two different UV light sources were used later in the research related to aerosol charging. One is low pressure mercury lamps (Burtscher et al., 1982; Jung et al., 1988) and the other the excimer lamps (Kogelschatz, 1992; Maisels et al., 2003).

Burtscher et al. (1982) designed an apparatus using a monochromatic low pressure Hg arc ($h\nu$ = 4.9 eV) for the measurement of electric mobility and electrical charges of particles in the atmosphere. Three different particles, i.e., silver particles, auto exhaust particulate and atmospheric aerosol, were used for the evaluation of Burtscher's apparatus. Jung et al. (1988) designed a photoelectric charger to achieve high particle charging efficiency, resulting in the reduction of particles which are not precipitated by

electrostatic fields due to the charge reduction by reattachment of negative ions to the positively charged particles. Jung's charger consists of a quartz tube with two metallic grids separately laid along the inner wall of the tube. The innermost metallic grid is on the electrical ground, and the outer one is on a DC voltage. Three advantages can be recognized with the above grid configuration. One is that the photoemission from the tube walls is eliminated, another that negative ions diffusing towards the tube walls can easily be removed, and the other that the charger core is free of an external electrical field. For these existing chargers, the fraction of particles remaining electrically neutral was approximate 2% for the 16 nm and 10% for the 10 nm.

Using the apparatus developed by Kogelschatz (1992), charge distributions of particles were investigated by a tandem differential mobility analyzer (TDMA) as a function of particle size (i.e., 60, 75, 90, and 120 nm in diameter) and relative intensity of the irradiation (i.e., for two photo energies: $h\nu$ = 5.6 and 6 eV) (Mohr et al., 1996). For diesel particles with a diameter of 100 nm, an average charge of up to 25 elementary units was obtained for each particle. The mean charge and mobility distribution of the particles after passing through the same device were determined experimentally as a function of particle concentration (Mohr and Burtscher, 1997). According to the study, particles can be either unipolarly positive or bipolarly charged depending upon the concentration of ions present in the carrier gas. This is because in the device, the aerosol becomes positively charged when electrons are emitted from the particle surface as a result of UV irradiation. Meanwhile, negative ions are formed when photoelectrons attach instantaneously to gas molecules. Positively charged particles may thus have the chance to be discharged by negative ion attachment and even become negatively charged.

Hence, a reduction in charging efficiency is observed when the particle concentration is in the range of 10^5~10^6 #/cm^3 and the residence time of the ions in the aerosol exceeds a few tens of milliseconds (Mohr and Burtscher, 1997). Further, the aerosol can be unipolarly charged when negative ions are removed from the carrier gas faster than the diffusion of ions to particles. Current studies of UV chargers reduce the issue of ion diffusion discharging by either using diluted aerosol or removing negative ions in the irradiation-free region by an ion trap (Burtscher, 1992; Matter et al., 1995; Mohr et al., 1996).

Particle charge distribution as a function of particle number concentration and irradiation intensity was studied using a UV-charger with Xe excimer radiators with the wavelength of 172 nm (Maisels et al., 2003). In the above charger, highly positive-charged aerosols were obtained for the particle number concentration below 5×10^5 #/cm^3, and approximately symmetrically bipolar charge distributions of particles were measured for the number concentration of about 2×10^7 #/cm^3. Moreover, the feasibility of UV photoionization for singly unipolar-charged nanoparticles at flow rates up to 100 lpm was demonstrated using the same device (Hontañón and Kruis, 2008). The charging level of aerosol particles can be varied by adjusting the intensity of UV radiation. For monodisperse particles from 5 to 25 nm and at the number concentration between 10^4 and 10^5 #/cm^3, the output aerosol concentration of the above UV photoionizer was better than that of the radioactive ionizer (Kr^{85}) when an increased gas flow rate was used. The above UV photocharger behaved as a quasi-unipolar charger for polydisperse aerosols for sizes less than 30 nm and at number concentrations of 10^7 #/cm^3.

The performance of photo-chargers is quite different from ion diffusion chargers as the process strongly depends upon the particle composition. For electron escape from the particle surface, the kinetic energy of escaping electrons perpendicular to the particle surface must be greater than a given threshold, which depends on the work function of both the particle material and the particle size. Based on the Fowler-Nordheim equation (Fowler, 1931), a theoretical expression for photoionization charging was established, which is often incorporated in models describing the evolution of particle charge distribution. Since ion diffusion charging often occurs in photo-charging systems, charging models, including both photoionization and ion diffusion charging mechanisms, were developed in the studies of Maisels et al. (2002) and Jiang et al. (2007a).

Chapter 3

Particle Charge Conditioning by a Unipolar Corona Charger

3.1 Introduction

In this study, we first describe the design of a DC-corona-based, unipolar aerosol charge conditioner. We then present the result of the performance optimization of the prototype by varying the operational parameters such as the corona current, ion-driving voltage and aerosol flow rate. We further discuss the charging efficiencies and particle charge distributions at various conditions of conditioner operation for both Ag and KCl particles. Last, we apply the birth-and-death charging model with the ion-particle combination coefficient given by the Fuchs limiting sphere theory to predict the charging performance of the prototype (Fuchs, 1963).

3.2 Experimental Apparatus and Procedure

3.2.1 Design of the Unipolar Corona Charger

The schematic diagram of the prototype DC-corona-based, unipolar particle charge conditioner is shown in Fig. 3.1. The dimensions of the prototype are also included in the same figure. The construction of the prototype conditioner consists of (1) a cylindrical metal case with two aerosol inlet tubes at opposite positions of the case wall close to one end, and a single aerosol outlet at the other end of the case; and (2) a corona discharge tube module plugged in the prototype from the case end near the aerosol inlets. The corona discharge tube module, i.e., a metal tube with one end capped with a fine metal screen, is electrically insulated from the outer case. A pointed, solid tungsten needle is coaxially aligned with and electrically insulated from the tube module. The tip of the corona needle faces the center of the metal screen. A positive/negative high voltage is applied to the tungsten needle, producing positive/negative ions for particle charging.

The corona discharge tube module case is on the ion-driving voltage, much lower than that applied to the needle. When the electrical field strength at the needle tip is raised to a sufficiently high level (e.g., approximately 2.5 kV for 2 μA), surrounding air molecules are ionized, resulting in corona discharge. Ions produced in the tube module are driven through the metal screen by a weak electrical field (i.e., ion-driving field) into the charging zone, the space defined by the metal screen (at ion-driving voltage) and the charger case (electrically ground). Generally, the charging space is a cylindrical shape with the diameter of 5/16 in. and height of 1/2 in.. The geometrical arrangement of the tube module and the aerosol exit section allows establishing the ion-driving field approximately in the longitudinal direction. The charging ion concentration in the charging zone can be controlled by varying the strength of the ion-driving field. The arrangement of the ion-driving field and the aerosol exit section in the charger allows particles to quickly exit once they are electrically charged, thus reducing the loss of charged particles. No sheath air is used in this conditioner. The aerosol flow is directed into the charger via the aerosol inlet tubes. The annular spacing between the prototype body and tube module cases and the opposite injection of split aerosol stream enable the flow to be uniformly distributed in the circumferential direction upon entering the prototype. The aerosol flow is then converged to the particle charging zone at a 45^{o} angle relative to the conditioner axis. The design of aerosol transport in the conditioner minimizes the possibility of particles entering the tube module, resulting in a long lifetime of the corona needle used.

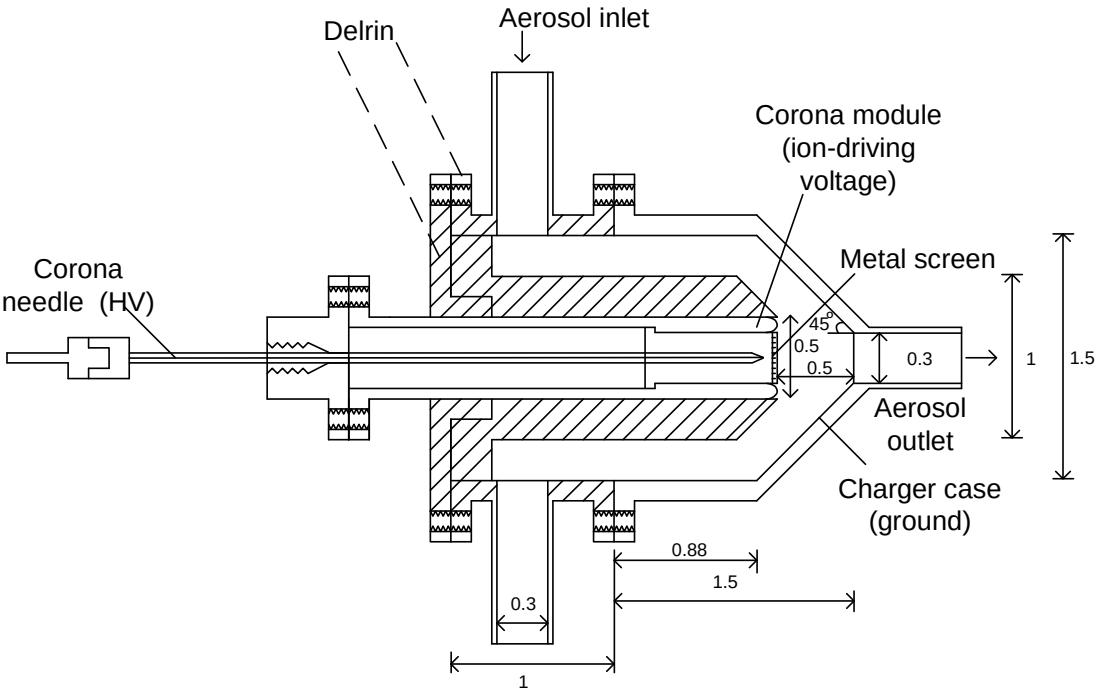

Figure 3.1 Schematic diagram of prototype DC-corona-based, unipolar particle charge conditioner (units in inch)

3.2.2 Experimental Setup for Evaluating the Unipolar Corona Charger

The experiment to characterize the performance of the prototype charge conditioner includes measuring the charging efficiency and charge distribution. Both intrinsic and extrinsic charging efficiencies are key parameters for performance evaluation of aerosol charge conditioners. The definition and measurement setups for charging efficiency vary in the literature, which was recently reviewed by Marquard et al. (2006a). In our study, the intrinsic charging efficiency is defined as the percentage of neutral particles entering the conditioner acquiring electrical charges in the process disregarding their final fates (either penetrating through or losing in the charger). Extrinsic charging efficiency describes the percentage of neutral particles which acquire

charges in the conditioner and make the exit. The difference between the intrinsic and extrinsic charging efficiencies represents the loss of charged particle in the conditioner (Qi et al., 2007).

As shown in Fig. 3.2, two different aerosol techniques were used to produce test aerosols. In one technique, polydisperse silver (Ag) particles with electrical mobility sizes ranging from 5 to 50 nm were generated by the evaporation-and-condensation method (Scheibel and Porstendörfer, 1983). Ag powder was placed in a ceramic boat, located in a high temperature tube furnace (Lindberg/Blue Model CC58114A-1). Nitrogen at the flow rate of 1.5 lpm (liters per minute) was used as the vapor carrier gas in the tube furnace. The flow rate of the carrier gas was regulated and monitored by a needle valve and a laminar flowmeter prior to its introduction to the ceramic tube used in the furnace. The Ag powder in the ceramic boat was evaporated at high temperature, and its vapor was carried out by the nitrogen flow. At the exit of the tube furnace, polydisperse nanoparticles were produced by mixing the hot, vapor-rich carrier gas with particle-free air at room temperature. A constant-output, home-made atomizer was used in the other technique to produce monodisperse KCl particles with electrical mobility sizes from 50 to 120 nm (Liu and Pui, 1974a). The operational flow rate of the atomizer was 4.0 lpm when the compressed air pressure was at 30 psig. Droplets produced by the atomizer were directed through a Po^{210} radioactive neutralizer to remove electrical charges on the particles, and diffusion dryer with silicone gel as the desiccant to remove the solvent in droplets.

At the downstream of the above described polydisperse aerosol generation systems, a differential mobility analyzer (DMAs, either TSI Model 3081 or 3085) was

used to classify monodisperse particles with the desired sizes. Prior to the DMA classification a Kr^{85} radioactive particle charger was used to achieve a well-defined charge distribution for input polydisperse particles (Knutson and Whitby, 1975). The DMA was operated at the aerosol flow rate of 1.5 lpm and sheath flow rate of 15.0 lpm. To obtain electrically-neutral particles for the experiments, DMA-classified particles were directed through a Po^{210} radioactive particle neutralizer and an electrostatic condenser.

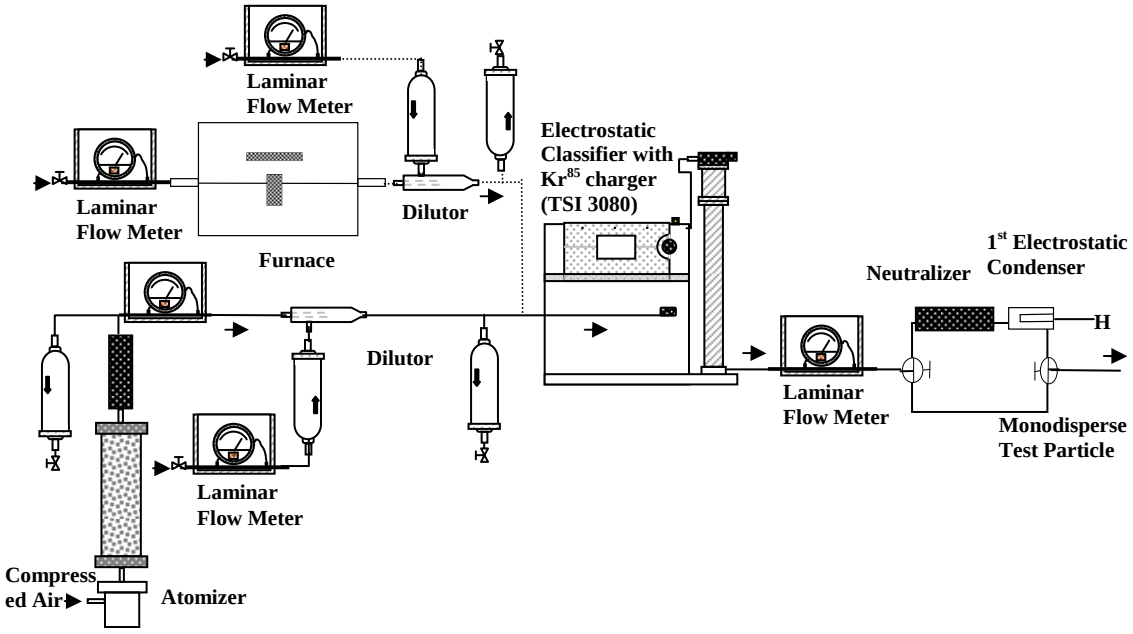

Figure 3.2 Aerosol generation systems to produce neutral monodisperse test particles

Shown in Fig. 3.3 is the experimental setup for the performance evaluation of the prototype. For the charging efficiency measurement, the charged fraction of particles exiting the prototype was then measured via passing the aerosol flow through a second electrostatic condenser to remove all charged particles, and then directed to an ultrafine condensation particle counter (UCPC TSI model 3025A) for counting the number

concentration of neutral particles in the flow. During the measurement, the aerosol flow rate through the prototype was controlled by both the UCPC pump operated at high flow mode (i.e., 1.5 lpm) and the house vacuum line in which the flow rate was regulated by a laminar flow meter and a needle valve.

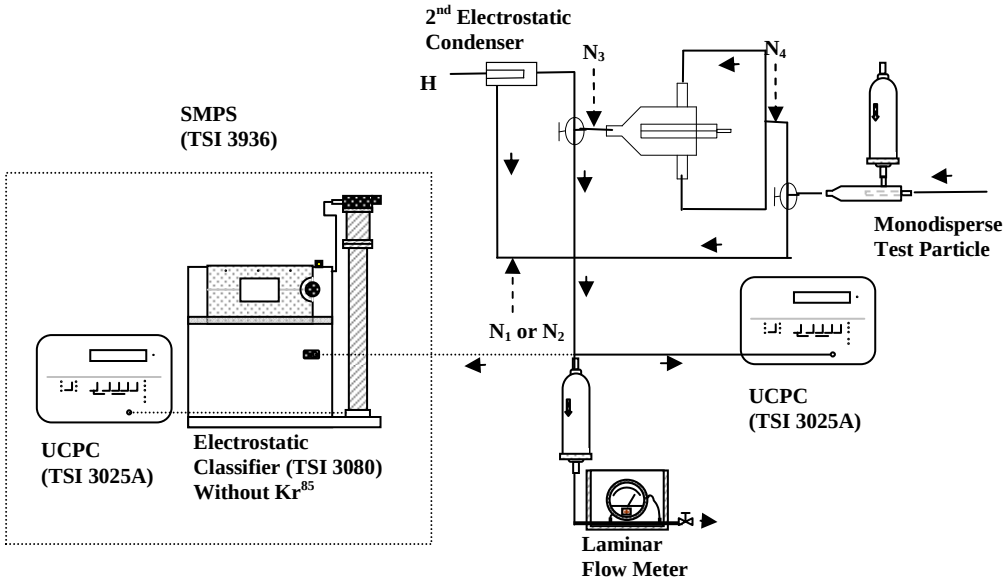

Figure 3.3 Experimental setup for the performance evaluation of the prototype

3.2.3 Charging Efficiency and Charge Distribution

The intrinsic charging efficiency was calculated by the method of Romay and Pui (1992):

$$\eta_{in} = 1 - \frac{N_1}{N_2}, \tag{3-1}$$

where η_{in} is the intrinsic charging efficiency; N_1 and N_2 are the particle number concentrations measured at the downstream of the second electrostatic condenser with applied high voltage turned on and off, respectively. The extrinsic charging efficiency was evaluated by the method described by Chen and Pui (1999):

$$\eta_{ex} = \frac{N_3 - N_1 / P_{ec}}{N_4}, \tag{3-2}$$

where η_{ex} is the extrinsic charging efficiency; N_3 the number concentration of particles exiting the prototype when it is turned on; N_4 the number concentration of particles entering the prototype; and P_{ec} the penetration of neutral particles through the second electrostatic condenser.

Particle charge distribution after they passed through the prototype was further characterized in this study. The tandem DMA technique was used to measure the particle charge distribution of monodisperse test particles at different sizes. The particle generation systems for this part of the experiment were the same as those described previously. The electrical mobility distribution of particles leaving the charger was directly measured by SMPS without the Kr^{85} particle neutralizer in place. For the measurement of negatively charged particles, the DMA was connected to an external high voltage power supply. Since test particles entering the prototype are monodisperse in size, the electrical mobility distribution of the particles, measured by the SMPS, indicates the charge distribution of test particles exiting the prototype. Note that the charge distribution measured in our study is for particles at the exit of the prototype charge conditioner, not in the charging zone of the prototype.

3.3 Unipolar Charging Model

To solve the problem of unipolar diffusion charging, a birth-and-death model was developed, which consists of an infinite set of differential equations with the assumption that ion concentration N_i is constant and much higher than the total particle concentration

(Boisdron and Brock, 1970). The solution of the equations provides the charging efficiency and charge distribution for a given $N_i t$ condition.

$$\frac{dN_0}{dt} = -\beta_0 N_0 N_i, \tag{3-3}$$

$$\frac{dN_1}{dt} = \beta_0 N_0 N_i - \beta_1 N_1 N_i, \tag{3-4}$$

……

$$\frac{dN_n}{dt} = \beta_{n-1} N_{n-1} N_i - \beta_n N_n N_i, \tag{3-5}$$

where N_n is the particle number concentration with n elementary charges, t is the particle residence time, and β_n is the combination coefficient between particles with n elementary charges and ions, which can be calculated by Fuchs limiting sphere theory (Fuchs, 1963) in the transition regime. It assumes that the space around a particle is separated into two regions by an imaginary sphere concentric to the particle. Outside the limiting sphere, the motion of ion is determined by the macroscopic diffusion mobility theory; between the sphere and the particle, ion movement is described by the thermal speed and interaction potential with the particle. Matching of the flux of ions at the surface of the limiting sphere, the combination coefficient is calculated.

$$\beta = \frac{\pi \theta c_i \delta^2 \exp(-\frac{\varphi(\delta)}{kT})}{1 + \frac{\theta c_i \delta^2}{4 D_i} \exp(-\frac{\varphi(\delta)}{kT}) \int_\delta^\infty \frac{1}{r^2} \exp(\frac{\varphi(r)}{kT}) dr} \tag{3-6}$$

where $\delta = \frac{a^3}{\lambda_i^2}\left[\frac{1}{5}\left(1+\frac{\lambda_i}{a}\right)^5 - \frac{1}{3}\left(1+\frac{\lambda_i^2}{a^2}\right)\left(1+\frac{\lambda_i}{a}\right)^3 + \frac{2}{15}\left(1+\frac{\lambda_i^2}{a^2}\right)^{5/2}\right]$, (3-7)

$$\phi(r) = \int_r^{\infty} F dr = K_E \left[\frac{ne^2}{r} - \kappa \frac{a^3}{2r^2\left(r^2 - a^2\right)} \right]. \quad (3\text{-}8)$$

Here, θ is the probability of an ion entering the limiting sphere to collide and transfer its charge to particles, δ is the limiting-sphere radius, which is a function of particle radius a and the ion mean free path λ_i, c_i and D_i are the mean thermal velocities and the diffusion coefficients of the ion, respectively, k is the Boltzmann's constant, T is the temperature of the system, and $\varphi(r)$ is the potential energy at the distance r from the center of particle, in which F is the ion-particle interaction force (the Coulomb force and the image force), K_E is coulomb constant in the form of $K_E = 1/4\pi\varepsilon_0$ with the vacuum permittivity ε_0, e is the elementary unit of charge, κ is the image force parameter in the form of $\kappa = \frac{(\varepsilon - 1)}{(\varepsilon + 1)} e^2$ with particle dielectric constant ε.

Without the electrical force, the collision probability θ is the square of the ratio of the particle radius to the limiting sphere radius ($\theta = \frac{a^2}{\delta^2}$). For a charged particle, θ is calculated by the minimum collision parameter (Natanson, 1960),

$$b^2 = r^2 \left[1 + \frac{2}{3kT} [\phi(\delta) - \phi(r)] \right]. \quad (3\text{-}9)$$

By setting $db^2 / dr = 0$, the collision probability θ is calculated as

$$\theta = \frac{b_m^2}{\delta^2}, \quad (3\text{-}10)$$

where b_m is the minimum collision parameter.

In equation (3-6) and (3-7), to calculate the combination coefficient β the mean thermal velocity c_i, diffusivity of ions D_i, and mean free path λ_i are used, which can be

estimated based on the electrical mobility Z_i and molecular weight M_i of ions as follows, (Kennard, 1938; Einstein, 1956)

$$c_i = \sqrt{\frac{8kTN_a}{\pi M_i}}, \tag{3-11}$$

$$D_i = \frac{kTZ_i}{e}, \tag{3-12}$$

$$\lambda_i = 1.329\frac{Z_i}{e}\sqrt{\frac{kTM_iM_g}{(M_i + M_g)N_a}}, \tag{3-13}$$

where N_a is Avogadro's number and M_g is the molecular weight of background gas.

3.4 Results and Discussion

3.4.1 Optimization of the Operational Condition for the Prototype

First, the penetration of uncharged particles through the prototype without any applied voltage was measured and shown in Fig. 3.4. Monodisperse Ag particles in the diameters ranging from 5 to 20 nm were used for the measurement at different aerosol flow rates. The standard deviation for each data point includes the UCPC fluctuation. As expected the loss of uncharged particles in the prototype increases as the particle size and aerosol flow rate decrease. At the aerosol flow rate of 3 lpm, the uncharged particle penetration of the prototype reduces to 75% at 5 nm. The loss of uncharged particles larger than 20 nm is less than 5% and negligible for aerosol flow rate higher than 3 lpm.

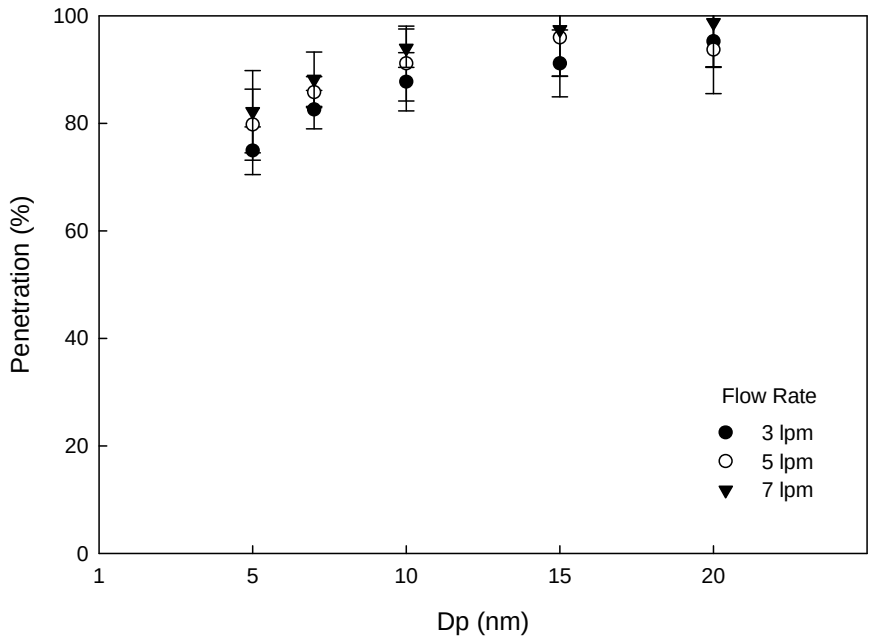

Figure 3.4 Penetration of uncharged particles through the prototype

The optimization of operational settings is required to maximize the performance of an aerosol charge conditioner. Practical applications using the charge conditioners will benefit the most when such optimization is focused on the extrinsic charging efficiency. For an aerosol charger based on the ion attachment technique, the intrinsic charging efficiency is affected mainly by the $N_i t$ (N_i is the ion concentration and t is the particle residence time) value when the charging mechanism is dominated by ion diffusion (Liu and Pui, 1974b), especially for particles in the submicron and nanometer range. For the prototype, the particle residence time in the charging zone can be controlled by the aerosol flow rate. The ion concentration in the charging zone can be controlled by either the corona current or ion-driving voltage. With a higher corona current or higher ion-voltage, the ion concentration in the charging zone of the charger can be increased, which

leads to the increase of intrinsic charging efficiency. However, the increase in ion concentration results in more charged particle loss because of the space charge effects. Thus, the extrinsic charging efficiency of the prototype would not be continuously increased if we simply increased the ion concentration in the charger charging zone. A decrease of the ion-driving voltage reduces the loss of charged particles due to the electrostatic effect. Unfortunately, it also reduces the intrinsic charging efficiency of the prototype, resulting in the decrease in extrinsic charging efficiency. An experiment was thus conducted to optimize the operational setting of the prototype with respect to the extrinsic charging efficiency.

We selected monodisperse Ag particles in the diameter of 10 nm as our test aerosol. Fig. 3.5(a, b) shows the intrinsic and extrinsic charging efficiencies of the prototype charger at various corona discharge currents and ion-driving voltages, respectively. The aerosol flow rate was fixed at 3 lpm. It is evident in Fig. 3.5a that the intrinsic charging efficiency increases with the increase of the ion-driving voltage and/or corona current. However, the data given in Fig. 3.5b shows that the effect of corona current on the extrinsic charging efficiency is not noticeable for the prototype. This implies that the ion-driving voltage is the main parameter for the control of ion concentration in the charging zone. For steady operation, the corona current is thus fixed at 2 μA in the following experiment. Further, the extrinsic charging efficiency increases with an increase of the ion-driving voltage, and remains constant after an ion-driving voltage of 600 V.

10 nm

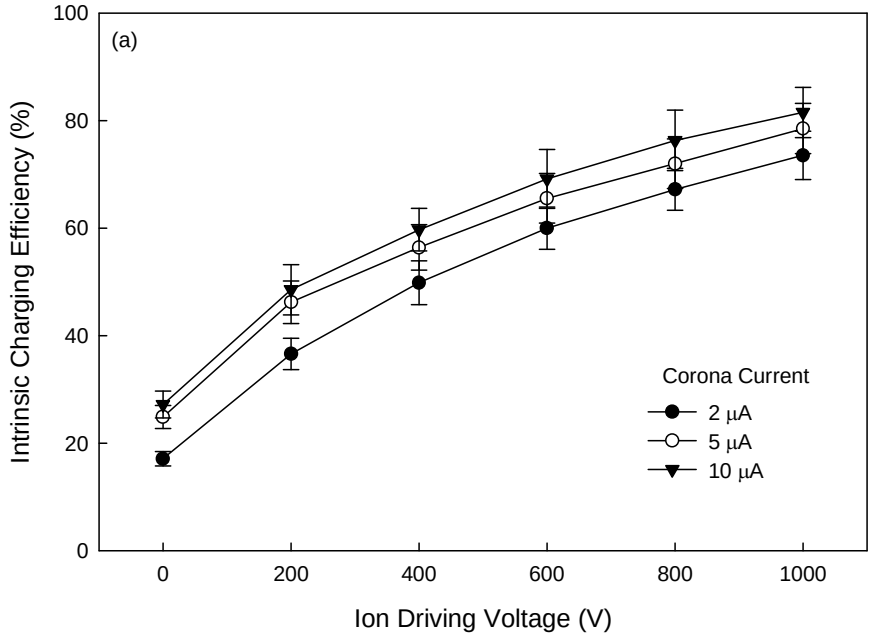

10 nm

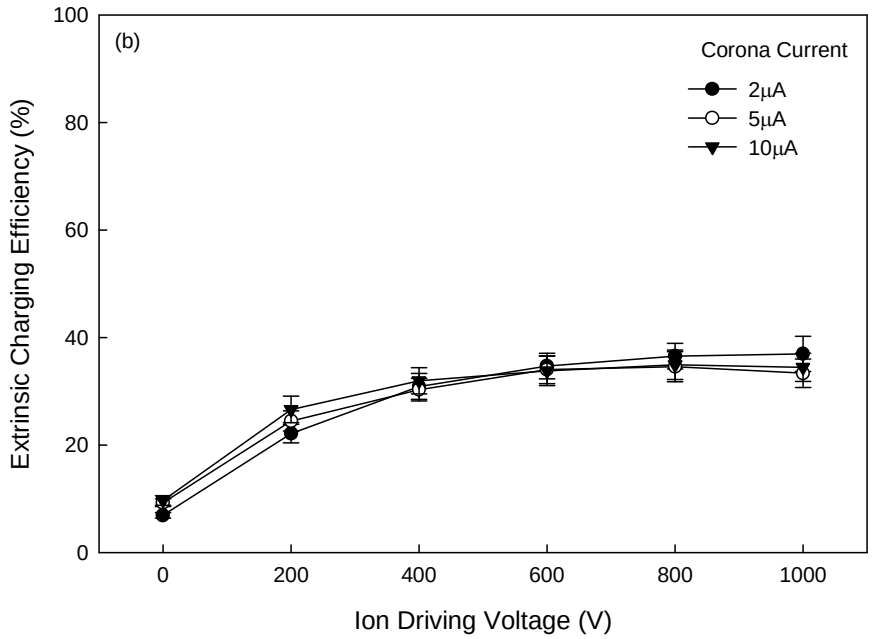

Figure 3.5 Intrinsic and extrinsic positive charging efficiencies of the prototype for 10 nm particles at different corona discharge currents and ion-driving voltages

Fig. 3.6(a, b) shows the intrinsic and extrinsic charging efficiencies of the prototype at different aerosol flow rates and ion-driving voltages, respectively. The corona discharge current was fixed at 2 μA. As expected, the intrinsic charging efficiencies decrease with the increase of aerosol flow rate. For the extrinsic charging efficiency, a higher aerosol flow rate requires a higher ion-driving voltage to achieve the maximum. In the 1 KV ion-driving voltage range, the maximal extrinsic charging efficiency occurred at a 3 lpm aerosol flow rate and an ion-driving voltage of 600 V.

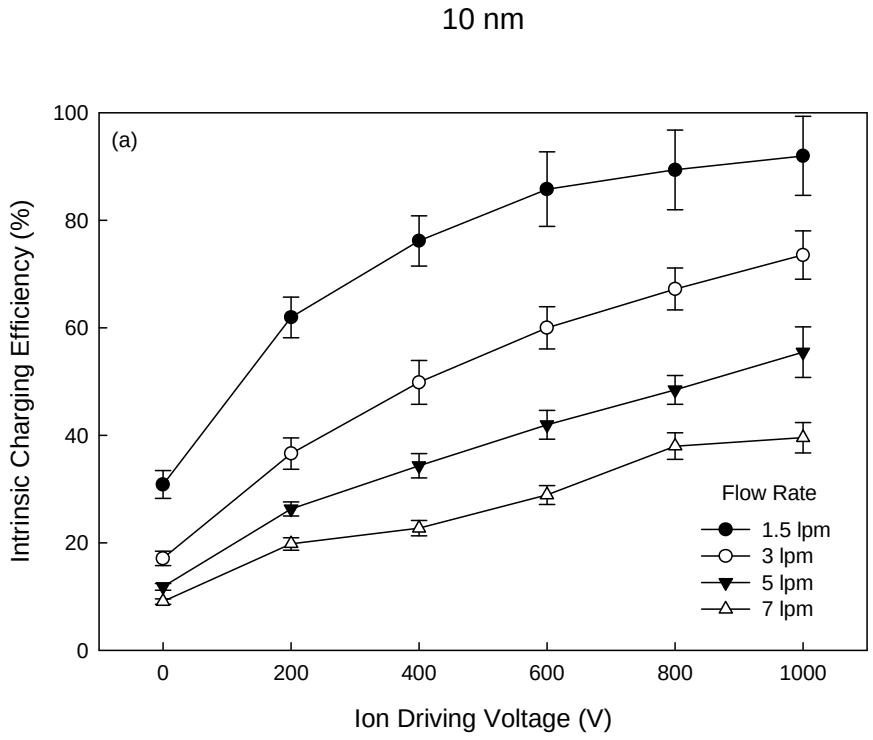

10 nm

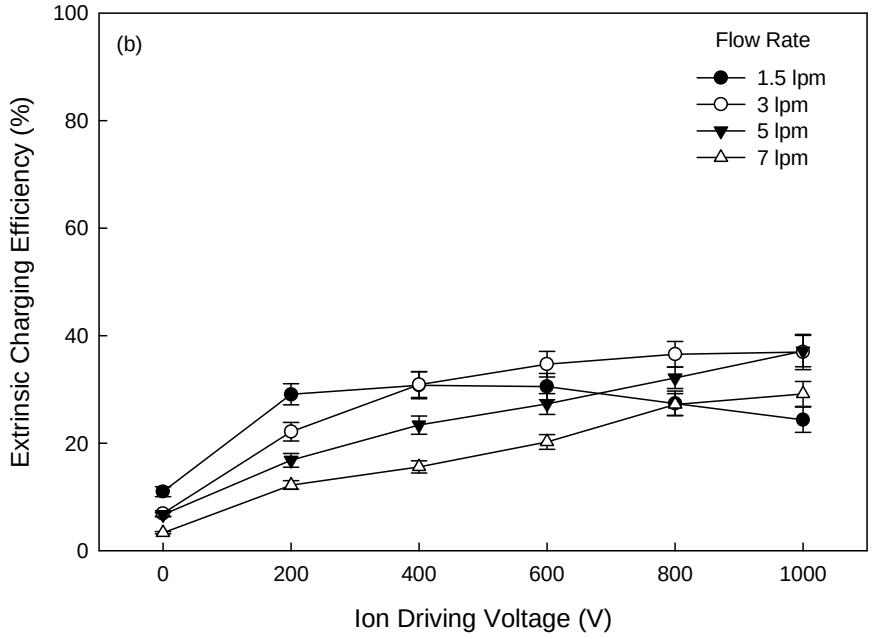

Figure 3.6 Intrinsic and extrinsic positive charging efficiencies of the prototype charger for 10 nm particles at different aerosol flow rates and ion-driving voltages

3.4.2 Charging Efficiency for the Prototype

The intrinsic and extrinsic charging efficiencies of the prototype at an aerosol flow rate of 3 lpm and an ion-driving voltage of 600 V for particles in the size range from 5 to 50 nm are shown in Table 3.1 and Fig. 3.7(a, b). For the comparison, we also include the experimental charging efficiency data of Buscher's charger (Buscher et al., 1994), the twin Hewitt charger (Kruis and Fissan, 2001), the mixing-type charger (Qi et al., 2007), and the miniature charger (Qi et al., 2008) in Fig. 3.7(a, b). For the intrinsic charging efficiency (shown in Fig. 3.7a), the prototype charger gives better performance than mixing-type and miniature chargers. The intrinsic charging efficiency of the prototype is higher than 80% for particles with diameters larger than 15 nm. Among all the corona-

based unipolar chargers, the prototype shows nearly the same extrinsic charging efficiency as twin Hewitt and mixing-type chargers over the studied size range, and better than Buscher's and the miniature chargers. The extrinsic charging efficiency of the prototype is higher than 60% for particles of diameters larger than 15 nm.

Table 3.1 Charging efficiency data for the prototype

Dp (nm)	Intrinsic charging efficiency (%)	Standard deviation (%)	Extrinsic charging efficiency (%)	Standard deviation (%)
5	31.76	2.33	7.14	0.67
7	43.99	1.92	17.85	1.05
10	59.63	3.40	34.53	2.55
15	79.71	5.06	56.32	4.79
20	90.80	6.45	68.85	4.72
30	98.49	6.60	82.08	5.48
40	100.00	-	83.33	3.71
50	100.00	-	88.26	5.39

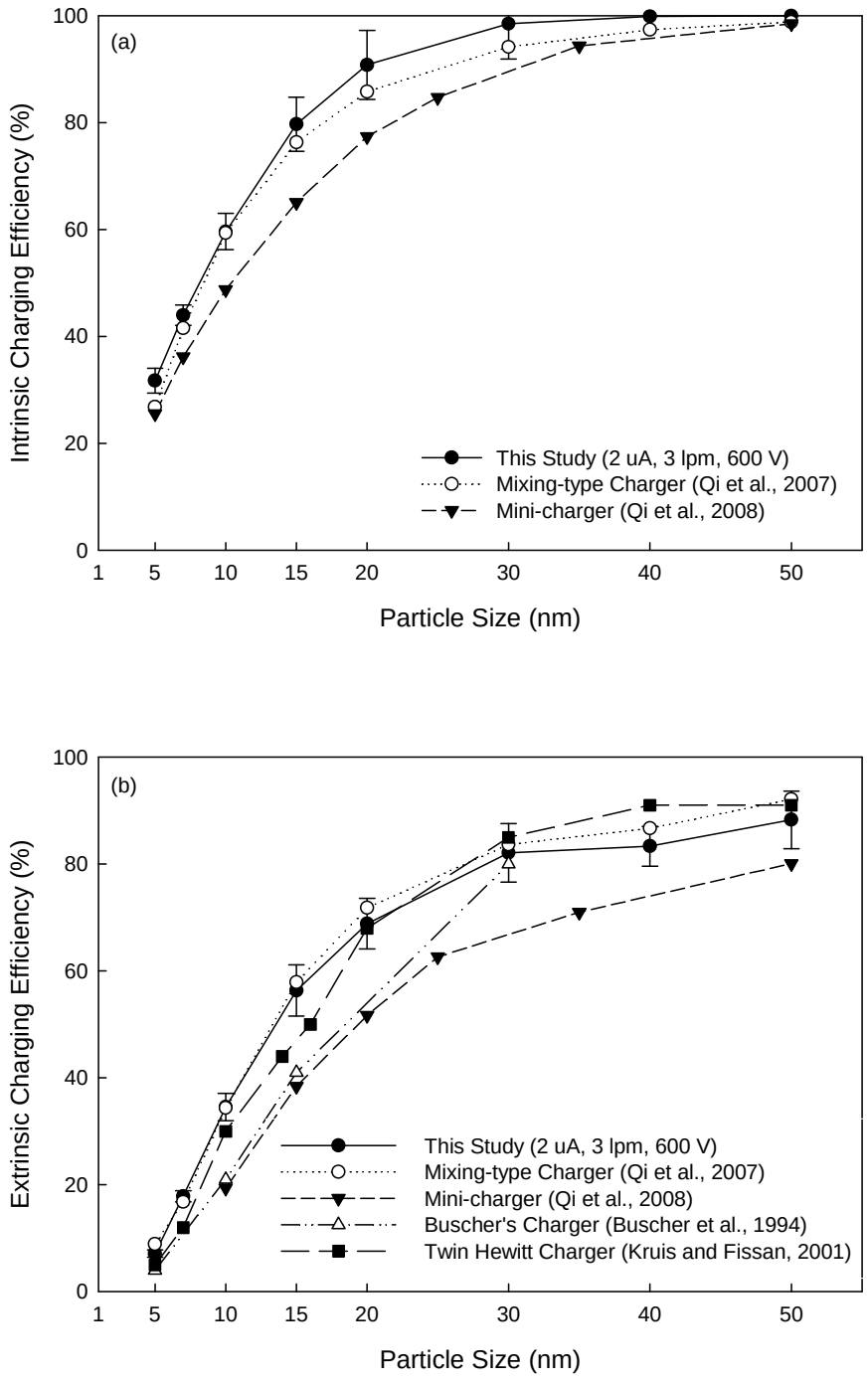

Figure 3.7 Comparison of intrinsic and extrinsic positive charging efficiencies among different chargers for particles in the size range from 5 to 50 nm

3.4.3 Control of Ion Concentration in the Prototype

As discussed above, the ion concentration in the prototype is controlled by the ion-driving voltage. Fig. 3.8 shows the intrinsic charging efficiency of the prototype at various ion-driving voltages when particle concentrations were on the order of 10^3~10^4 #/ cm3. The aerosol flow rate and corona current of the prototype were fixed at 3 lpm and 2 μA, respectively. Further included in Fig. 3.8 are the curves calculated by the birth-and-death particle charging model (Boisdron & Brock, 1970) with the ion-particle combination coefficient calculated by the Fuchs limiting sphere model (Fuchs, 1963). For positive ions, the values of the most probable ion mass and mobility used were 109 amu and 1.4 cm^2/V-s, corresponding to the hydrated proton $H^+(H_2O)_6$ (Pui et al., 1988). The N_it value listed for each ion-driving voltage was obtained by varying N_it to best fit the experimental data. The calculated N_it values were on the order of 10^6~10^7 s/cm^3, 100 times larger than particle concentration. This satisfies the birth-and-death model assumption that the ion concentration should be much higher than that of particles. The charging model assumes that the ion concentration in the charging zone is constant. The discrepancy between the experimental and calculated data might be because of the spatial non-uniformity of the ion concentration in the charging zone of the prototype.

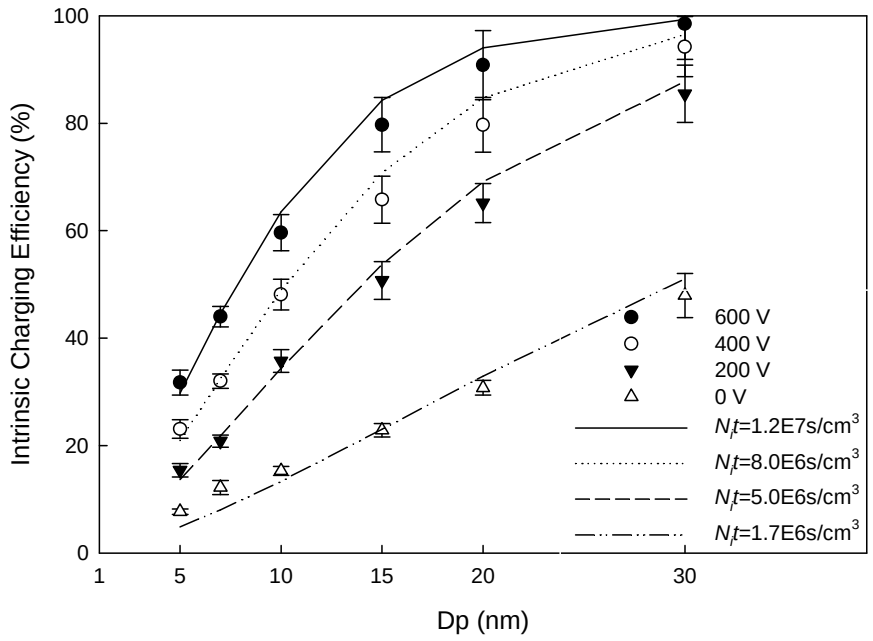

Figure 3.8 Intrinsic positive charging efficiencies of the prototype at different ion-driving voltages

To experimentally estimate the ion number concentration in the charging zone, the charger case was grounded via a resistor. The voltage on the resistor was measured by a multimeter to further obtain the current *I*, which are 17.76, 9.09 and 2.93 nA at the ion-driving voltage of 600, 400, and 200V, respectively. According to the deposition of ions on the charger case, the current *I* can also be calculated as

$$I = eSv_i\overline{N_i}\,, \tag{3-14}$$

where S is the deposition area of ions, $\overline{N_i}$ is the average ion concentration in the charging zone, and v_i is the ion travelling velocity as a function of electrical field E with the expression $v_i=Z_iE$. Since it is difficult to directly obtain the deposition area S from the structure of the charger, we assume that it is located at the corner between the contraction

part and the charger outlet tube. So the deposition area S can be calculated as $S=2\pi rl$, where r is the inner radius of the outlet tube and l is the length of the deposition area at the corner. Due to the non-uniform of the electrical field in the charging zone, there is no simple solution to describe the electrical field. To simplify the calculation, the electrical field is expressed as $E=V_a/d$, where V_a is the voltage applied on the corona module and d is the distance between the screen and the corner.

The average particle residence time in the charging zone is calculated as

$$\bar{t} = \frac{V}{Q}, \tag{3-15}$$

where Q is the aerosol flow rate and V is the volume of the charging zone with the expression $V=\pi r^2 d$, which is defined as the space between the screen of the corona module and the corner. At the aerosol flow rate of 3 lpm, the residence time $\bar{t}$ is estimated to be 12.6ms.

Based on the above description, the product of $\overline{N_i t}$ is expressed as

$$\overline{N_i t} = \frac{I}{eSv_i}\frac{V}{Q} = \frac{Ird^2}{2eZ_i V_a Ql}. \tag{3-16}$$

The unknown variable l can be estimated by matching the $N_i t$ values from the unipolar charging model. At the length l of 0.76 mm, the products of $\overline{N_i t}$ are 1.11E7, 8.52E6, and 5.49E6 s/cm^3 at the ion-driving voltage of 600, 400, and 200V, respectively. The small value of l means that most of ions are deposited at the corner between the contraction and the outlet tube, which also confirms our assumption.

The unipolar ion charging increases the percentage of electrically charged nanoparticles for the size distribution measurement. The information of multiple charges

on particles becomes critical from the viewpoints of particle size distribution measurement and classification. In the experiment measuring the charge distribution on particles, the prototype was operated at 3 lpm aerosol flow rate and 2 μA corona current. Table 3.2 and Fig. 3.9(a-d) show the positive charge distributions of test particles with diameter of 60 nm and at the concentration of approximately 1.3×10^4 #/cm^3 for various ion-driving voltages. Note that the experimental data shown in Table 3.2 and Fig. 3.9 is the extrinsic charge distribution of particles, not the intrinsic one. As a reference, the intrinsic charge distributions calculated by the birth-and-death charging model with the Fuchs limiting sphere theory are also given in Fig. 3.9. The $N_i t$ values best fitted in the prediction of intrinsic charging efficiency (i.e., obtained in Fig. 3.8) were used in this calculation. The agreement between the experimental and calculated charge distributions is very reasonable. The discrepancy between both charge distributions can be attributed to the loss of charged particles and the non-uniform ion concentration in the charging zone. As expected, particle charge distributions move towards singly charged status with the decrease of ion-driving voltage. By varying the ion-driving voltage, we can adjust the ion concentration in the charging zone to control the charge distribution or the mean charges on particles.

Table 3.2 Extrinsic positive charge distributions of test particles with diameter of 60 nm at a concentration of about 1.3×10^4 #/cm^3 for different ion-driving voltages

Number of elementary charges	Fraction (%)							
	Experiment (600V)	Model ($N_i t$=1.2E7 s/cm^3)	Experiment (400V)	Model ($N_i t$=8E6 s/cm^3)	Experiment (200V)	Mode ($N_i t$=5E6 s/cm^3)	Experiment (0V)	Model ($N_i t$=1.7E6 s/cm^3)
1	8.67	4.33	12.87	13.90	31.09	32.30	52.52	58.85
2	44.82	52.38	49.29	60.62	44.41	55.26	20.49	19.78
3	26.45	39.51	20.52	24.08	10.81	11.17	2.90	1.03
4	7.95	3.72	5.96	1.33	1.65	0.34	0.00	0.01
5	1.77	0.05	1.37	0.01	0.06	0.00	0.00	0.00

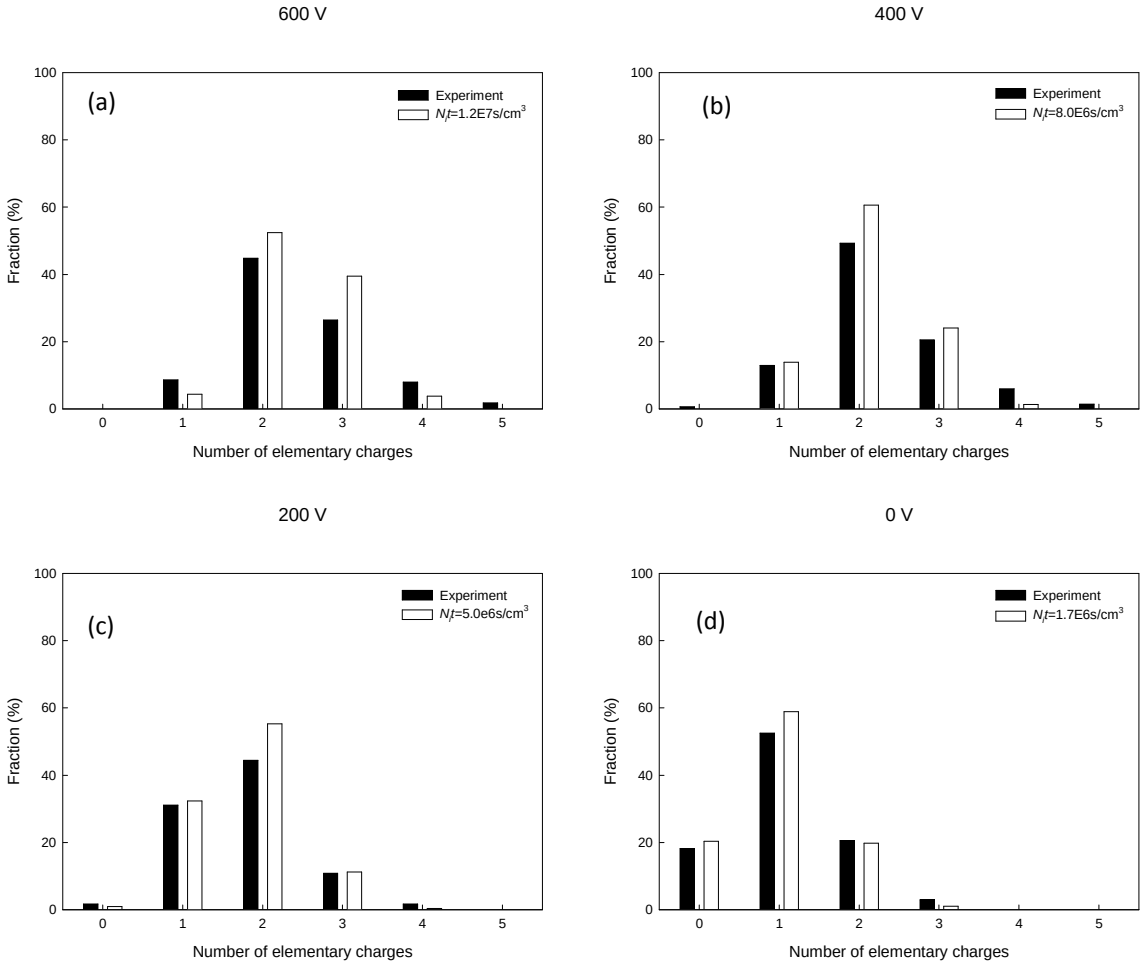

Figure 3.9 Extrinsic positive charge distributions of test particles with diameter of 60 nm at a concentration of about 1.3×10^4 #/cm^3 for different ion-driving voltages

Note that the particle concentration and initial status of charges on particles are also important in the particle charge conditioning process (Adachi et. al., 1989; Qi et. al., 2009). Particle charge distribution may be varied for particles with high concentrations and/or at different initial charge statuses when using the same operational setting for the prototype. Nonetheless, one can always reach the desired charge distribution on particles with the feature of controllable ion concentration built in the prototype.

3.4.4 Comparison of Positive and Negative Charging

In our study, we further evaluated the performance of the prototype for negative charge conditioning. Via the same optimization process as described in section 3.4.1, the optimal operation condition for the prototype via negative ions is the same as that via positive ions. The positive and negative extrinsic charging efficiencies for the prototype in particle sizes ranging from 5 to 50 nm are shown in Table 3.3 and Fig. 3.10. For the comparison, we also include the experimental data of the mixing-type charger and the miniature charger in Fig. 3.10. Note that the operational conditions of the mixing-type and miniature chargers for negative charging were optimized at 5 lpm and 1.5 lpm, respectively. The prototype shows equivalent extrinsic charging efficiencies for both positive and negative charging, which are higher than the other two chargers. Also note that the negative charging efficiency for the mixing-type charger is far lower than its positive one. This is because of much smaller orifices used to limit the sonic jet flow rate for delivering charging ions in the mixing-type charger. With high electrical mobility of negative ions and the presence of a strong corona field, it is difficulty for negative ions to survive through the orifices with much smaller size, resulting in low ion concentration in the charging region of the mixing-type charger. For the miniature charger, the negative charging efficiency is slightly higher than the positive one because of higher electrical mobility of negative ions. However, the negative charging efficiency of the miniature charger remains less than that of the prototype, because the tight charging zone and ion-driving field design of the miniature charger leads to more charged particle loss in the exiting process.

Table 3.3 Comparison of extrinsic charging efficiency of the prototype between positive and negative charging for particles in the size range from 5 to 50 nm

Dp (nm)	Positive extrinsic charging efficiency (%)	Standard deviation (%)	Negative extrinsic charging efficiency (%)	Standard deviation (%)
5	7.14	0.67	8.53	0.74
7	17.85	1.05	16.91	1.38
10	34.53	2.55	32.81	3.05
15	56.32	4.79	59.63	5.21
20	68.85	4.72	71.62	8.56
30	82.08	5.48	81.74	2.10
40	83.33	3.71	86.98	6.10
50	88.26	5.39	92.30	6.39

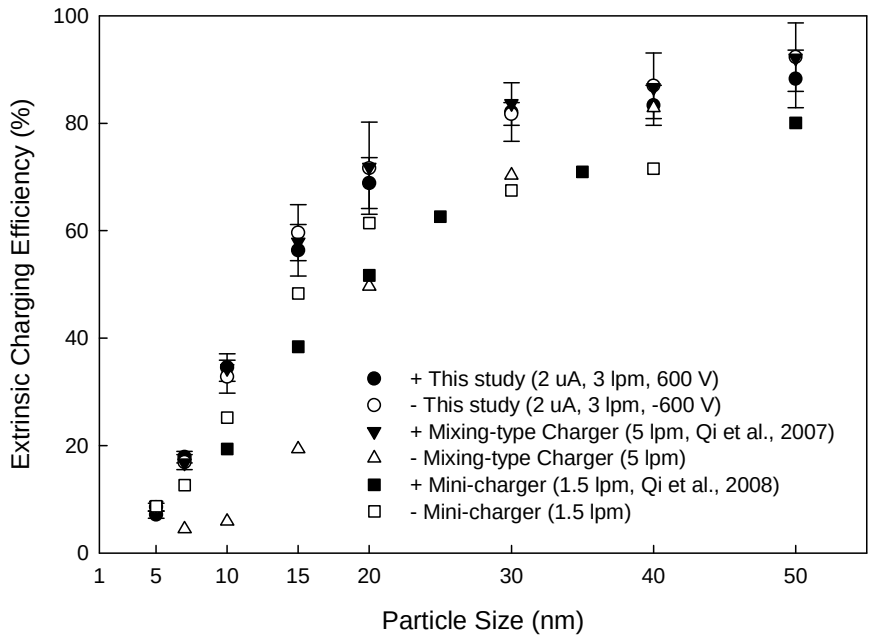

Figure 3.10 Comparison of extrinsic charging efficiency between positive and negative charging for particles in the size range from 5 to 50 nm

3.5 Summary

The performance of a prototype corona-based, unipolar aerosol charge conditioner has been experimentally investigated. The construction of the prototype consists of an outer metal case and a corona discharge tube module with one end capped with a metal screen. Ions produced by the corona discharge module are driven through the metal screen by a weak, biased electrical field between the screen and conditioner case (i.e., ion-driving voltage). The ion concentration in the charging zone can thus be controlled by varying ion-driving electrical field strength. The particle charging zone in the prototype is defined as the space between the metal screen and the aerosol exit channel of the prototype case. The nearly longitudinal electrical field in the charging zone is established

by the geometrical arrangement of outer case and aerosol exit tube (both on the electrical ground), and the tube module (on the ion-driving voltage). The design of the charging zone in the charger also enables the quick exit of particles once they are electrically charged, thus reducing the loss of charged particles. No sheath air was used in this prototype. The aerosol flow is directed into the prototype by two inlets located at opposite positions, and then flown to the charging zone in a 45^{o} direction to the prototype axis. The flow design minimizes the potential contamination of the corona needle tip by particles, thus prolonging the needle's lifetime.

The performance of the prototype was optimized by varying operational parameters (i.e., aerosol flow rate, corona current, and ion-driving voltage) to achieve its maximal extrinsic charging efficiency. The optimization experiment was done with monodisperse Ag particles of 10 nm in diameter. Based on our finding, the corona current had negligible effect on the charging performance of the prototype. The corona current of 2 μA was thus used in the rest of our study. Our study also found that operating the prototype at a 3 lpm aerosol flow and an ion-driving voltage of 600 V offers the maximal extrinsic charging efficiency.

Both intrinsic and extrinsic charging efficiencies of particles in diameters ranging from 5 to 50 nm were measured at the optimal operation condition. This prototype provides higher extrinsic efficiency than other corona-based unipolar chargers for both positive and negative charging. Charge distributions of monodisperse particles at the downstream of the prototype, operating at a 3 lpm aerosol flow rate, a 2 μA corona current and various ion-driving voltages, were measured by the tandem-DMA technique. The charge distribution measurement confirmed that the charge distribution of particles

after passing through the prototype is variable via the control of charging ion concentration with changing the ion-driving voltage. The birth-and-death charging model with the Fuchs limiting sphere theory was used to obtain the $N_i t$ values at different operation conditions via best fitting to the measured intrinsic charging efficiency. The same $N_i t$ values obtained were also used in the birth-and-death charging model to calculate the charge distribution of particles. Reasonable agreement was achieved when the calculated charge distributions of particles were compared with the extrinsic charge distributions measured. The result implies the less loss of charged particles in the prototype than existing unipolar chargers in which the aerosol flow direction is perpendicular to the electrical field direction.

Chapter 4

Investigation of Aerosol Charging Using Pen-type UV Lamps

4.1 Introduction

In this study, a simple UV aerosol charger using pen-type UV lamps was constructed. DMA-classified silver (Ag) and metal oxide particles were used as test particles and the effect of light intensity on particle photocharging was investigated by varying the number of lamps used in the charger. Finally, we applied the existing UV charging model to predict the charging performance of the studied UV charger and verified it by comparing its result with experimental data.

4.2 Experimental Setup and Procedures

4.2.1 Description of Studied UV Charger and Experimental Evaluation

Fig. 4.1 shows the schematic diagram of the investigated UV aerosol charger. The basic configuration of the prototype is a quartz tube of about 7 in. long, which is surrounded by four low pressure Hg lamps (UVP model 96-0004-7). We used a cylindrical aluminum case having aerosol inlet and outlet at the ends to enclose the quartz tube and lamps for preventing operators from being exposed to UV light and for transporting aerosol through the quartz tube without contacting with the lamps. We also designed an ion trap at the quartz tube exit to minimize the recombination of positively charged particles and negative ions.

The experiments to characterize the performance of the UV aerosol charger include the measurements of the charging efficiency and charge distribution of particles existing from the charger. For the particle charging efficiency, both intrinsic and extrinsic efficiencies are key parameters for the performance evaluation of an aerosol charger. In this study, we define the intrinsic charging efficiency as the percentage of entering

neutral particles acquiring electrical charges in the charger disregarding their final fates (i.e., either exiting or lost in the charger), and the extrinsic charging efficiency as the percentage of entering neutral particles which acquire electrical charges in the charger and make their exit. The difference between the intrinsic and extrinsic particle charging efficiencies thus represents the loss of charged particles in the charger (Qi et al., 2007).

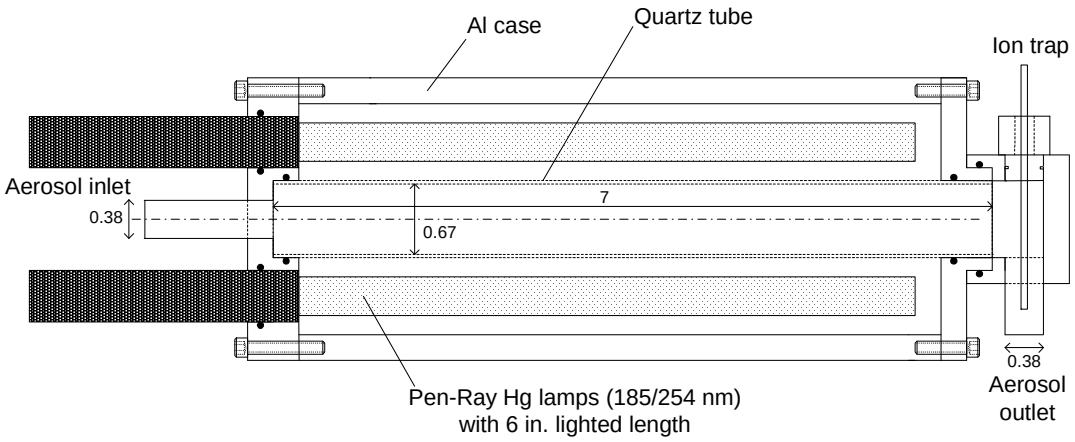

Figure 4.1 Schematic diagram of the studied UV charge (units in inch)

4.2.2 Experimental Setups

The aerosol dispersion system with two generation techniques is the same as shown in Fig. 3.2. In one technique, polydisperse Ag particles with electrical mobility sizes ranging from 7 to 30 nm were generated by the evaporation-and-condensation method (Scheibel and Porstendörfer, 1983). A constant-output, home-made atomizer was used in the other technique to produce monodisperse metal oxide particles with electrical mobility sizes from 50 to 200 nm (Liu and Pui, 1974a). Downstream of the above described polydisperse aerosol generation systems, a differential mobility analyzer (DMAs, either TSI Model 3081 or 3085) operating with the aerosol flow rate of 1.5 lpm and sheath flow rate of 15.0 lpm was used to classify monodisperse particles into the

desired sizes. To obtain electrically-neutral particles for the experiments, DMA-classified particles were directed through a Po^{210} radioactive particle neutralizer and an electrostatic condenser.

Shown in Fig. 4.2 is the experimental setup for the performance evaluation of the UV charger. For the particle charging efficiency measurement, we measured the charged fraction of particles exiting the UV charger by passing the aerosol stream through a second electrostatic condenser to remove all charged particles, and then directed the particles to an ultrafine condensation particle counter (UCPC TSI model 3025A) to count the number concentration of neutral particles in the stream. In the measurement, both the UCPC vacuum pump operated at high flow mode (i.e., 1.5 lpm) and the house vacuum controlled the aerosol flow rate through the UV charger. We used a laminar flow meter and a needle valve in the gas line to control the flow rate of the vacuum source.

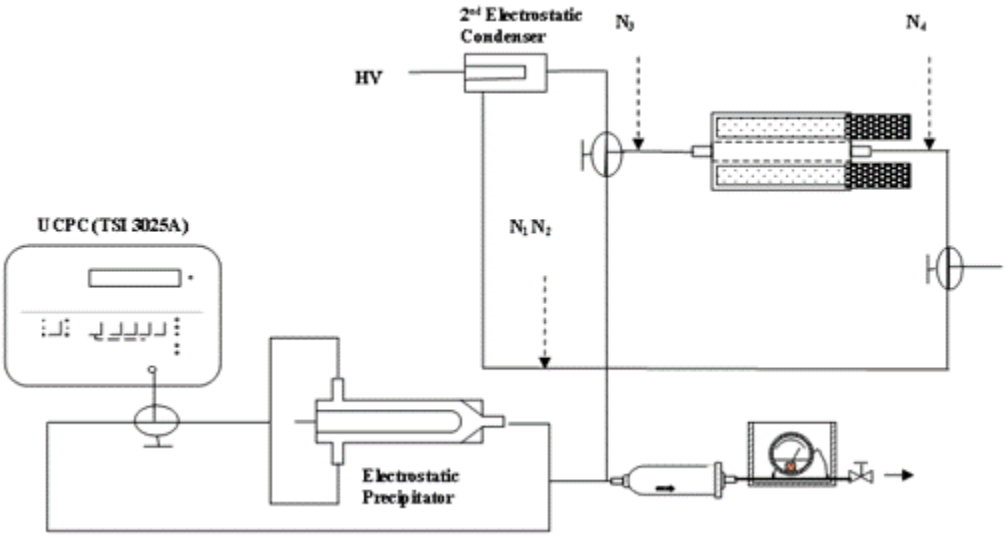

Figure 4.2 Experimental setup for the performance evaluation of the UV charger

We then calculated the intrinsic particle charging efficiency using the method of Romay and Pui (1992):

$$\eta_{in} = 1 - \frac{N_1}{N_2}, \tag{4-1}$$

where η_{in} is the intrinsic charging efficiency; N_1 and N_2 the particle number concentrations measured downstream of the second electrostatic condenser with applied high voltage turned on and off, respectively. We evaluated the extrinsic particle charging efficiency using the method described by Chen and Pui (1999):

$$\eta_{ex} = \frac{N_3 - N_1 / P_{ec}}{N_4}, \tag{4-2}$$

where η_{ex} is the extrinsic charging efficiency; N_3 the number concentration of particles exiting the UV charger when it is turned on; N_4 the number concentration of particles entering the UV charger; and P_{ec} the penetration of neutral particles through the second electrostatic condenser.

This study further characterized particle charge distribution after particles passed through the UV charger. The particle generation systems for this part of the experiment were the same as those described previously. Due to the high charge level on particles, it is difficult to use the TDMA technique to directly measure the charge distribution of particles with high resolution. Instead, we used an electrostatic precipitator technique in this study for the charge distribution measurement (Adachi et al., 1991; Forsyth et al., 1998). The characteristic curve of charge particle penetration through an electrostatic precipitator can be, in general, expressed as

$$P = 1 - \eta_c = 1 - KZ_p \mathrm{V}, \tag{4-3}$$

where K is a function of precipitator dimension; V the applied voltage on the precipitator; and Z_p the particle electrical mobility with the expression $Z_{p,n} = \frac{n_p e C_c}{3\pi\mu d_p}$, in which n_p is the particle electrical charge, C_c the Cunningham correction factor, and μ the gas viscosity.

Assuming the total charge fraction is equal to 1, $\sum F_{n,j} = 1$ (where $F_{n,j}$ is the fraction of particles with n charges), the particle penetration $P_j(d_p, V_m)$ with diameter d_p at rod voltage V_m, is calculated as $P_j(d_p, V_m) = 1 - KV_m \sum F_{n,j} Z_{p,n}$.

In the electrostatic precipitator technique, the penetration of charged particles through the precipitator at different applied voltages was measured with a UCPC. We thus retrieved the electrical mobility distribution of particles leaving the charger by comparing the calculated penetration with collected experimental data using the Bayesian statistic analysis (Ramachandran and Kandlikar, 1996; Hogan et al., 2009). We then derived the charge distribution of particles from the electrical mobility distribution of the particles. Note that the derived charge distribution obtained in our study is for particles at the charger exit (i.e., extrinsic particle charge distribution), not in the UV irradiation zone (i.e., intrinsic charge distribution).

4.3 Photocharging Model

Previous works have addressed modeling of aerosol charging by simultaneous photoionization and gaseous ion diffusion (Maisels et al. 2002; Jiang et al. 2007a; Hontañón and Kruis, 2008). The evolution with time of the concentration of ions and

particles in a gas flow under the exposure of UV radiation is governed by the population balance equations:

$$\frac{dN_i}{dt} = \sum_{R_p} \sum_{q} [\alpha^{q-1\to q} - \beta^{q+1\to q} N_i] N_{R_p,q} - \Delta_i \,, \tag{4-4}$$

$$\frac{dN_{R_p,q}}{dt} = [\alpha^{q-1\to q} N_{R_p,q-1} - \alpha^{q\to q+1} N_{R_p,q}] + N_i [\beta^{q+1\to q} N_{R_p,q+1} - \alpha^{q\to q-1} N_{R_p,q}] - \Delta N_{R_p,q} \tag{4-5}$$

where N_i is the concentration of negative ions in the gas; $N_{Rp,q}$ the concentration of particles with the size of R_p; Δ_i the particle loss to the charger walls; β the ion-to-particle attachment coefficient; and α photoionization rate.

The ion-to-particle attachment coefficients are calculated based on the theory of the limiting sphere by Fuchs (1963)

$$\beta = \frac{\pi \theta c_i \delta^2 \exp(-\frac{\varphi(\delta)}{kT})}{1 + \frac{\theta c_i \delta^2}{4 D_i} \exp(-\frac{\varphi(\delta)}{kT}) \int_{\delta}^{\infty} \frac{1}{r^2} \exp(\frac{\varphi(r)}{kT}) dr} \,, \tag{4-6}$$

where θ is the probability of an ion entering the limiting sphere to collide and transfer its charge to particles; δ is the limiting-sphere radius, which is a function of particle radius and the ion mean free path; c_i and D_i are the mean thermal velocities and the diffusion coefficients of the ion, respectively; $\varphi(r)$ is the potential energy at the distance r from the center of particle; k is the Boltzmann's constant; and T is the temperature of the system.

The photoionization rate α is the photoelectric yield coefficient (the photoelectron yield per time for given particles)

$$\alpha = Y(h\upsilon) \frac{I}{h\upsilon} \pi R_p^{\,2} \,; \tag{4-7}$$

where *Y(hν)* denotes the electron yield per incident photon, h is the Planck's constant, ν is the frequency of UV irradiation, and *I* is the intensity of the radiation. Current models of photoelectric aerosol charging rely on the Fowler-Nordheim law for photoemission from clean surfaces

$$Y(h\upsilon) = K_c (h\upsilon - \Phi)^m \text{ (Fowler 1931),} \tag{4-8}$$

where K_c and m are material-dependent constants and Φ stands for the photothreshold, for metallic spheres, with the form

$$\Phi = \Phi_\infty + \frac{e^2}{4\pi\varepsilon_0}\left(\frac{q+1}{R_p} - \frac{5}{8R_p}\right) \text{ (Wood 1981);} \tag{4-9}$$

where Φ_∞ denotes the work function, i.e., the photothreshold for an infinite planar surface, which is a characteristic of the material, and ε_0 and e are the permeability of vacuum and elementary charge, respectively.

The current data related to the photoemission of nanoparticles is rather limited and mostly on metal nanoparticles. The Fowler-Nordheim law has been successfully used to predict the photoemission yield of a variety of metallic particles (Ag, Cu, Pd, Au), PbS, and SnO with m = 2. However, the photoemission constant K_c is a major unknown of the model. From experimental observation, the value of K_c is in general larger for particles than for flat surfaces (Burtscher et al., 1982; Schleicher et al., 1993). It has been found that the photoemission constant of Ag particles in air increased by a factor of 4 when the particle diameter decreased from 6 to 4 nm (Schmidt-Ott et al. 1980). Moreover, the photoemission constant was approximately constant in experiments with Ag particles of diameters between 5.4 and 10.8 nm in helium (Müller et al. 1988a) and with SnO particles of diameters ranging from 8 to 20 nm in nitrogen (Hontañón and

Kruis, 2008). In experiments where particles of Ag and sucrose were exposed to soft X-ray radiation in the presence of nitrogen, the value of K_c increased by a factor of 2 when the particle diameter was reduced from 15 to 6 nm (Jiang et al., 2007b). In experimental studies for aerosol charging by light irradiation, both the photoemission constant K_c and the intensity of incident light I are often difficult to characterize, and are thus determined empirically (Maisels et al., 2002, 2003; Jiang et al., 2007a, 2007b; Hontañón and Kruis, 2008).

After substituting in Equation (4-7), the photoionization rate α is then expressed as

$$\alpha = K_c \frac{\pi R^2}{h\upsilon}[h\upsilon - \Phi_\infty - \frac{e^2}{4\pi\varepsilon_0 R}(q+\frac{3}{8})]^2. \tag{4-10}$$

This equation shows that, when $h\nu > \Phi$, a sphere can be photoionized up to a maximum charge level at which the process saturates. The maximum can be derived from Equation (4-10):

$$q_{\max} = \frac{4\pi\varepsilon_0}{e^2}(h\upsilon - \Phi_\infty)R - \frac{3}{8}. \tag{4-11}$$

The limiting aerosol charging case in which the photoionization dominates the ion attachment to particles (i.e., $\alpha >> \beta N_i$) is analyzed herein. The ion balance equation is irrelevant in such a case. We assume for simplicity that the aerosol is monodisperse and electrically neutral. We further assume the wall loss of particles is negligible. Using the birth-and-death theory as proposed by Boisdron and Brock (1970), the particle balance equations can be solved and the result is as follows:

$$N_{R_p,q} = \begin{cases} \exp(-\alpha^{0\to 1}t) & for \quad q = 0 \\ -\sum_{j=0}^{q-1} k_{j,q-1} \frac{\alpha^{q-1\to q}}{\alpha^{j\to j+1} - \alpha^{q\to q+1}}[\exp(-\alpha^{j\to j+1}t) - \exp(-\alpha^{q\to q+1}t)] & for \quad 0 < q < q_{\max} \end{cases}$$

,(4-12)

with

$$k_{j,q} = \begin{cases} 1 & for \quad j = q = 0 \\ -k_{j,q-1} \dfrac{\alpha^{q-1 \to q}}{\alpha^{j \to j+1} - \alpha^{q \to q+1}} & for \quad j < q \\ -\sum_{j=0}^{q-1} k_{j,q} & for \quad j = q \neq 0 \\ 0 & for \quad j > q \end{cases} . \qquad (4\text{-}13)$$

Table 4.1 lists the values of the parameters that appeared in the particle photoionization rate α used in our study. The low-pressure Hg lamps used in our study emit light with the wavelength of 185 nm in addition to that at the 254 nm rated by the vendor. From our study we conclude that the photocharging process in the studied UV charger is in fact dominated by the irradiation with the wavelength of 185 nm, not 254 nm. The detailed explanation for the above conclusion is given in the next section.

Table 4.1 Model parameters used in the simulations

Photon energy hν	6.72 eV
Particle work function Φ_∞ (Ag)	4.26 eV
Fowler law power *m*	2
Elementary charge *e*	$1.6 * 10^{-19}$ C
Permittivity of air ε_0	$8.85*10^{-12}$ $C^2/N/m^2$
Simulation time *t*	0.45 s

4.4 Results and Discussion

4.4.1 Charging Efficiency for the UV Charger

The intrinsic and extrinsic charging efficiency of the UV charger at an aerosol flow rate of 5 lpm for four UV lamps and evaluating with monodisperse Ag particles with diameters ranging from 5 to 30 nm are shown in Table 4.2 and Fig. 4.3. For comparison, we also include the experimental charging efficiency of the twin Hewitt charger (Kruis and Fissan, 2001), the mixing-type charger (Qi et al., 2007), the min-charger (Qi et al., 2008), and the charge conditioner. The standard deviation for each data point includes the UCPC fluctuation. For the intrinsic charging efficiency (shown in Fig 4.3a), the UV charger performs better than the mixing-type charger and the charge conditioner. The intrinsic charging efficiency is higher than 90% for particles with diameters larger than 15 nm. For the extrinsic charging efficiency (given in Fig 4.3b), the prototype achieves higher than 80% for particles of diameter larger than 15 nm. Over 90% of the charged particles exit the UV charger, showing negligible particle loss in the aerosol transport process. Further, the UV charger performs much better than existing corona-based aerosol chargers. The above observation could be attributed to different aerosol charging mechanisms used in photo- and corona-based chargers, and the ability of the aerosol to exit directly after the charging zone designed in studied UV charger.

Table 4.2 Charging efficiency data of the UV charger for Ag particles in the size range from 7 to 30 nm at an aerosol flow rate of 5 lpm with four UV lamps

Dp (nm)	Intrinsic charging efficiency (%)	Standard deviation (%)	Extrinsic charging efficiency (%)	Standard deviation (%)
7	44.73	2.15	38.42	1.64
10	74.33	6.15	61.18	4.67
15	96.11	8.30	82.37	6.07
20	99.19	4.57	87.08	3.70
25	99.90	5.21	87.15	4.00
30	99.81	7.14	87.87	8.09

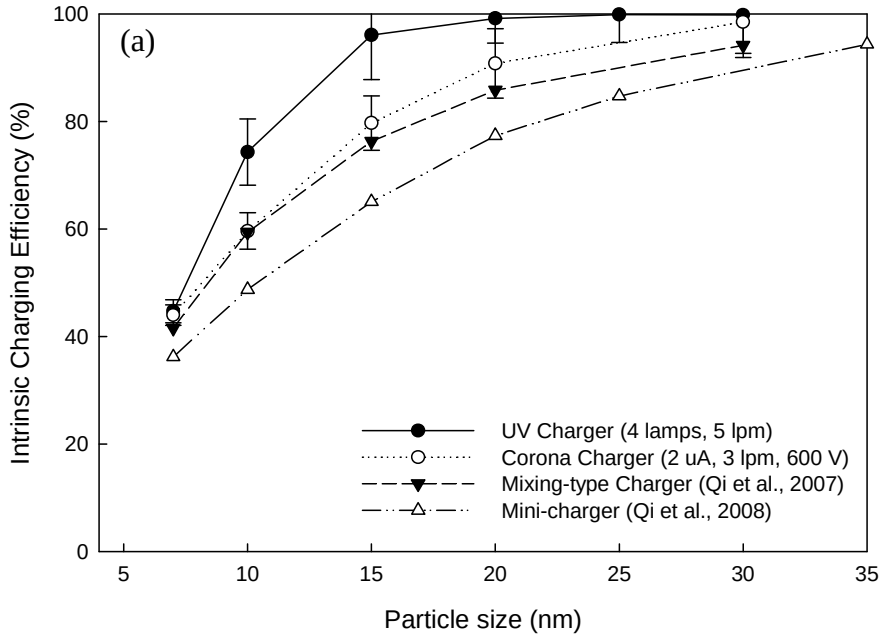

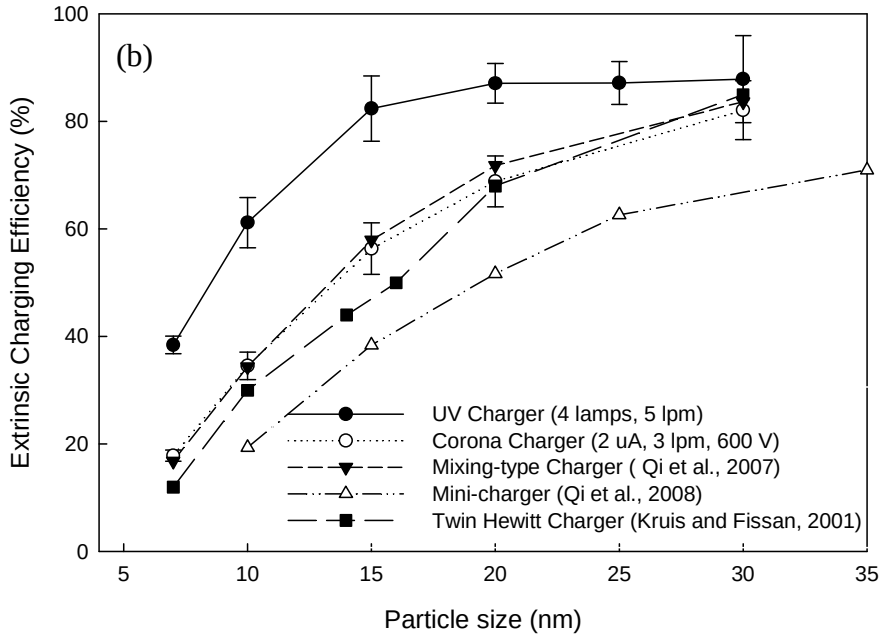

Figure 4.3 Comparison of intrinsic and extrinsic charging efficiency among different chargers for Ag particles in the size range from 7 to 30 nm

A DMA connected to an external positive high-voltage power supply was used downstream of the UV charger to find out if there were any negative ions or particles in the aerosol stream. The absence of negatively charged particles observed indicates that diffusion charging played no role in altering electrical charges on particles after their leaving the irradiation zone in the studied charger. We attribute the above observation to the low ion production in the UV charger because of the low particle concentrations used in our evaluation. Further, in the experiment the quartz tube was in fact heated by the absorption of UV light. The temperature of the tube was higher than that of the test aerosol stream. Thermophoretic forces resulting from the temperature difference between aerosol stream and tube wall may keep particles in the tube core region.

To investigate the material dependence of particle photocharging in the UV charger, monodisperse metal oxide particles (i.e., Fe_2O_3, TiO_2, ZnO, and Co_3O_4) were generated using the second aerosol generation technique described in Fig 3.2. We obtained the former two powders used in this study from Sigma-Aldrich and the latter two from Nanostructured & Amorphous Materials, Inc. The suspension of metal oxide powders was prepared by using the ultrasonic processor from Cole-Parmer for 20 minutes. Fig. 4.4 shows the intrinsic charging efficiencies of the UV charger at the aerosol flow rate of 5 lpm with four UV lamps for tested metal oxide particles in diameters ranging from 50 to 200 nm. The material dependence on the photocharging process is very obvious. The collected efficiency data can be classified into two groups: (1) Fe_2O_3 and Co_3O_4 particles and (2) ZnO and TiO_2 particles. In the former group, particles are all electrically charged after the UV charger for particle diameters larger than 100nm. For the latter group, nearly 30% charging efficiency was achieved for particles of the same diameters as those in the former group. Furthermore, the intrinsic charging efficiencies of metal oxide particles are much lower than those for Ag particles. Other than the different work functions for various particle materials and sizes, the material dependence for particle photocharging is mainly attributed to the photoemission constant K_c. To explain this phenomenon, theoretical models were developed to calculate the photoelectron emissions from small particles (Faraci el at., 1988; Müller et al., 1988b). The possible reasons may be among the effect of surface Plasmon (Aers and Inglesfield, 1983), excitation of electron-hole pairs (Penn and Rendell, 1982), geometrical factors (Chen and Bates, 1986), and escape function (Faraci et al., 1989). Particle shape may also affect the photocharging process. Fig. 4.5 shows the TEM and

SEM pictures of 150 nm metal oxide particles, which consist of primary particles of diameters around 20~30 nm. Generally, the agglomerate metal oxide particles are not perfect spherical. The surface roughness may affect the photo absorption and the electron emission during particle photocharging process.

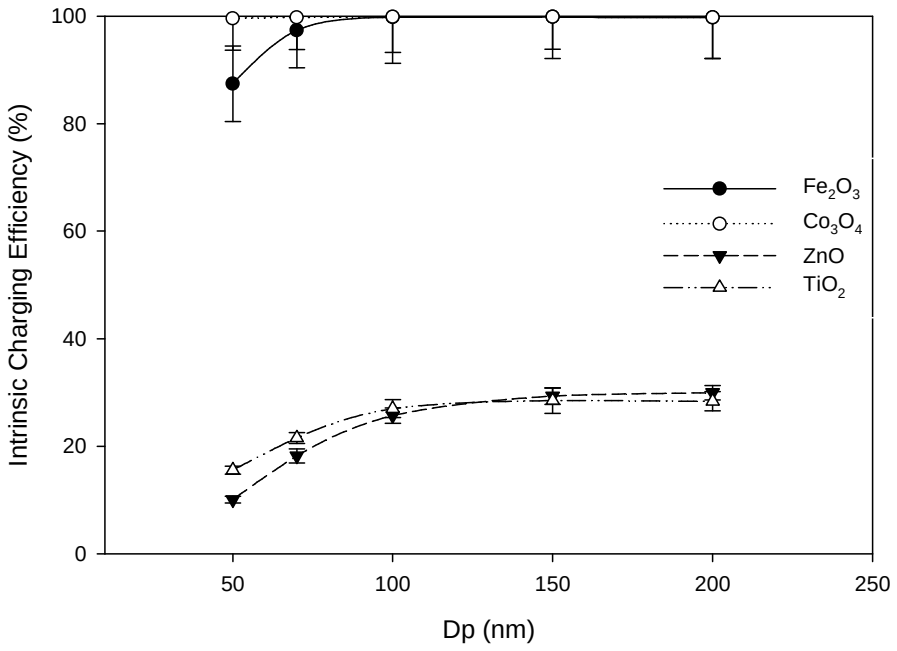

Figure 4.4 Comparison of intrinsic charging efficiencies of the UV charger for different metal oxide particles in the size range from 50 to 200 nm at an aerosol flow rate of 5 lpm with four UV lamps

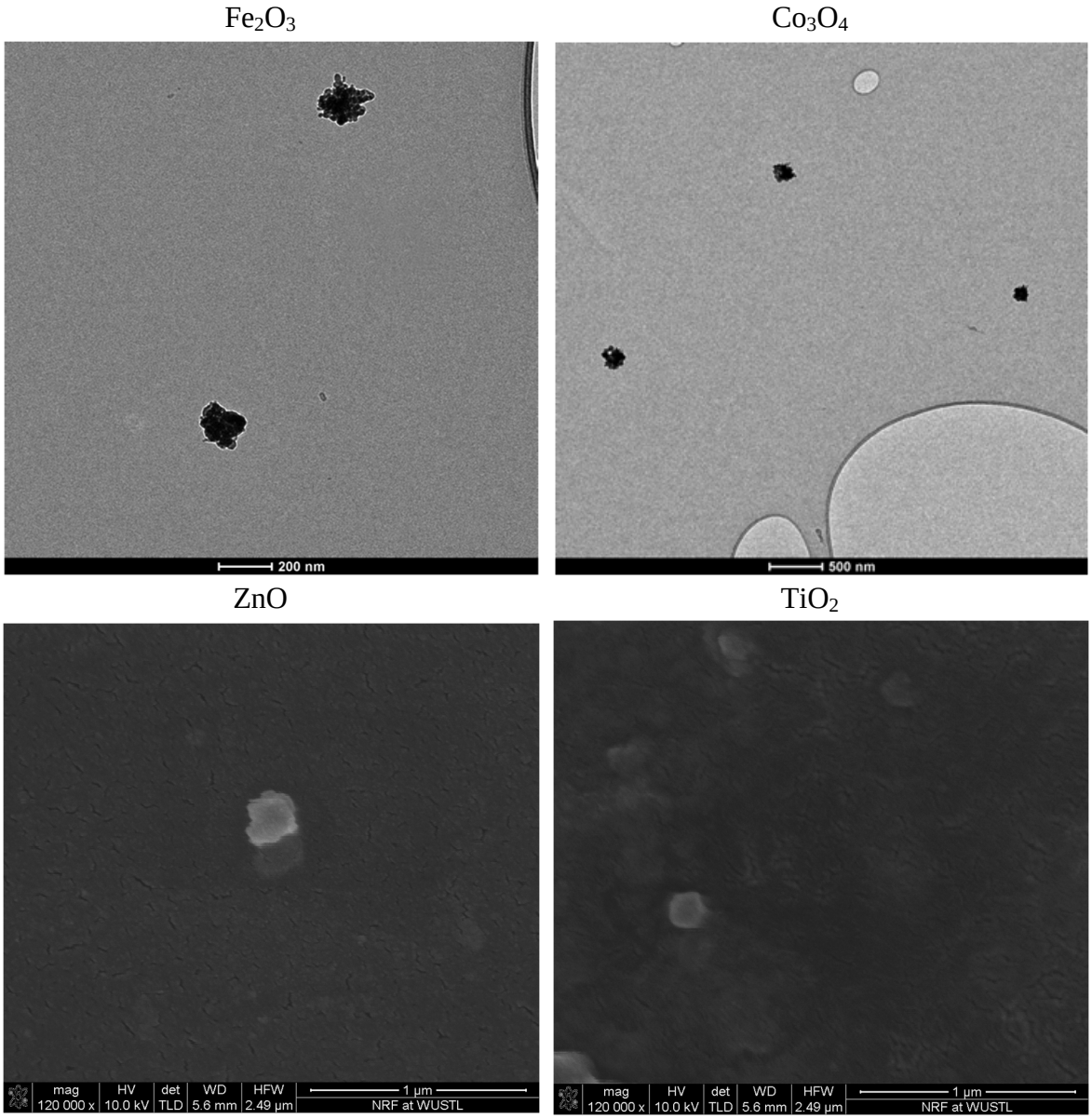

Figure 4.5 TEM and SEM pictures of 150 nm metal oxide particles

4.4.2 Charging Distribution for the UV Charger

We performed the experiment measuring the charge distribution on particles exiting the UV charger with the four UV lamps turned on and operated at 5 lpm aerosol flow rate. Figs. 4.6 and 4.7 are the measured charge distributions for Ag particles with diameters from 7 to 25 nm, and for Fe_2O_3 particles with diameters from 50 to 150 nm,

respectively, after their passing through the UV charger. The concentrations of test particles were kept at the level of $1\times10^3 \sim 2\times10^4$ #/cm^3. Note that the experimental data shown in Figs. 4.6 and 4.7 are in fact the extrinsic charge distribution of particles, not the intrinsic one. As expected, the particle charge distributions move towards the regime of high charges as particle size increases. Note that the charge distribution of 25 nm Ag particles is similar to that of 100 nm Fe_2O_3 particles, again showing the significant material dependence of the photocharging process.

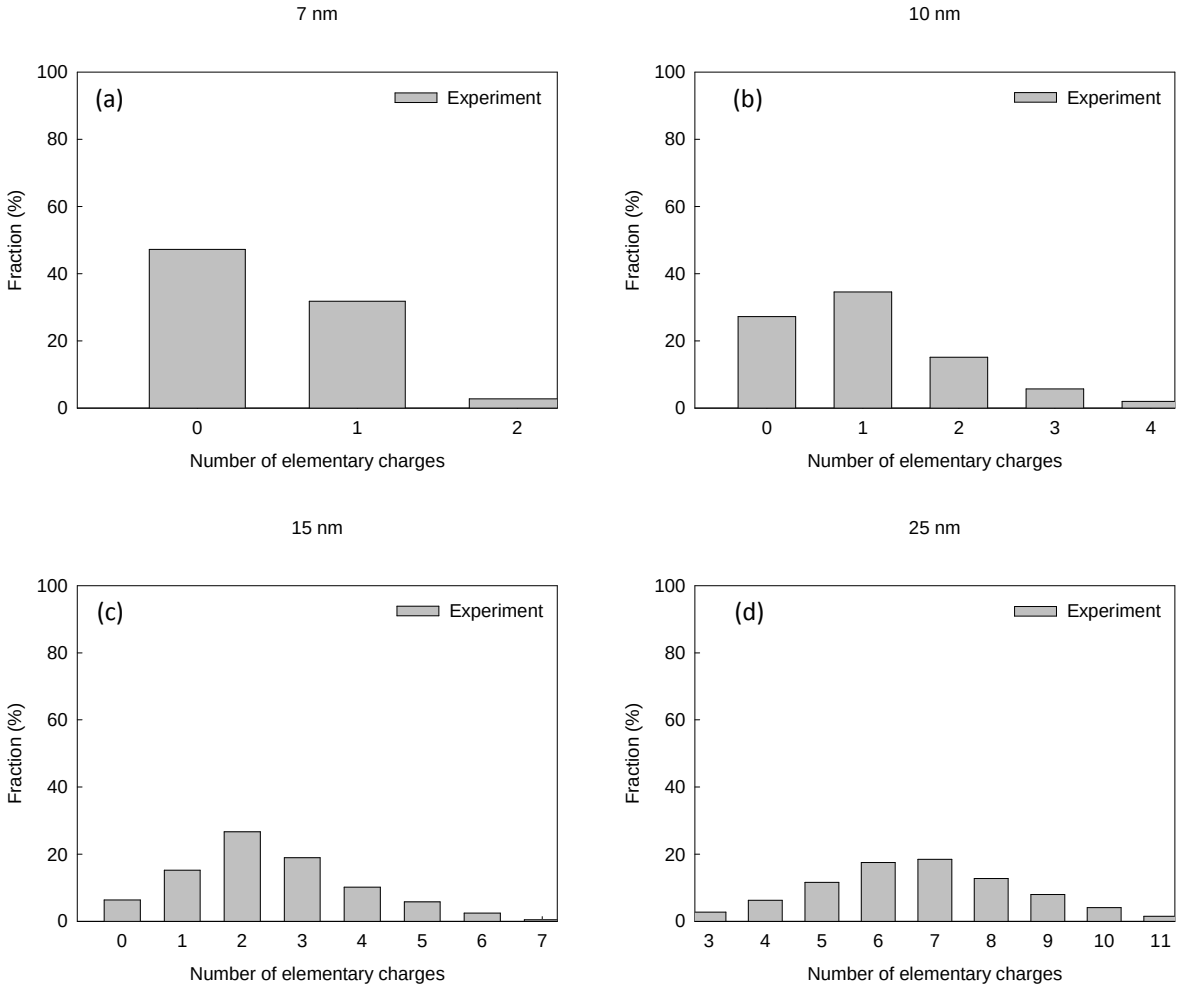

Figure 4.6 Extrinsic charge distributions of Ag particles with diameter from 7 to 25 nm at an aerosol flow rate of 5 lpm with four UV lamps

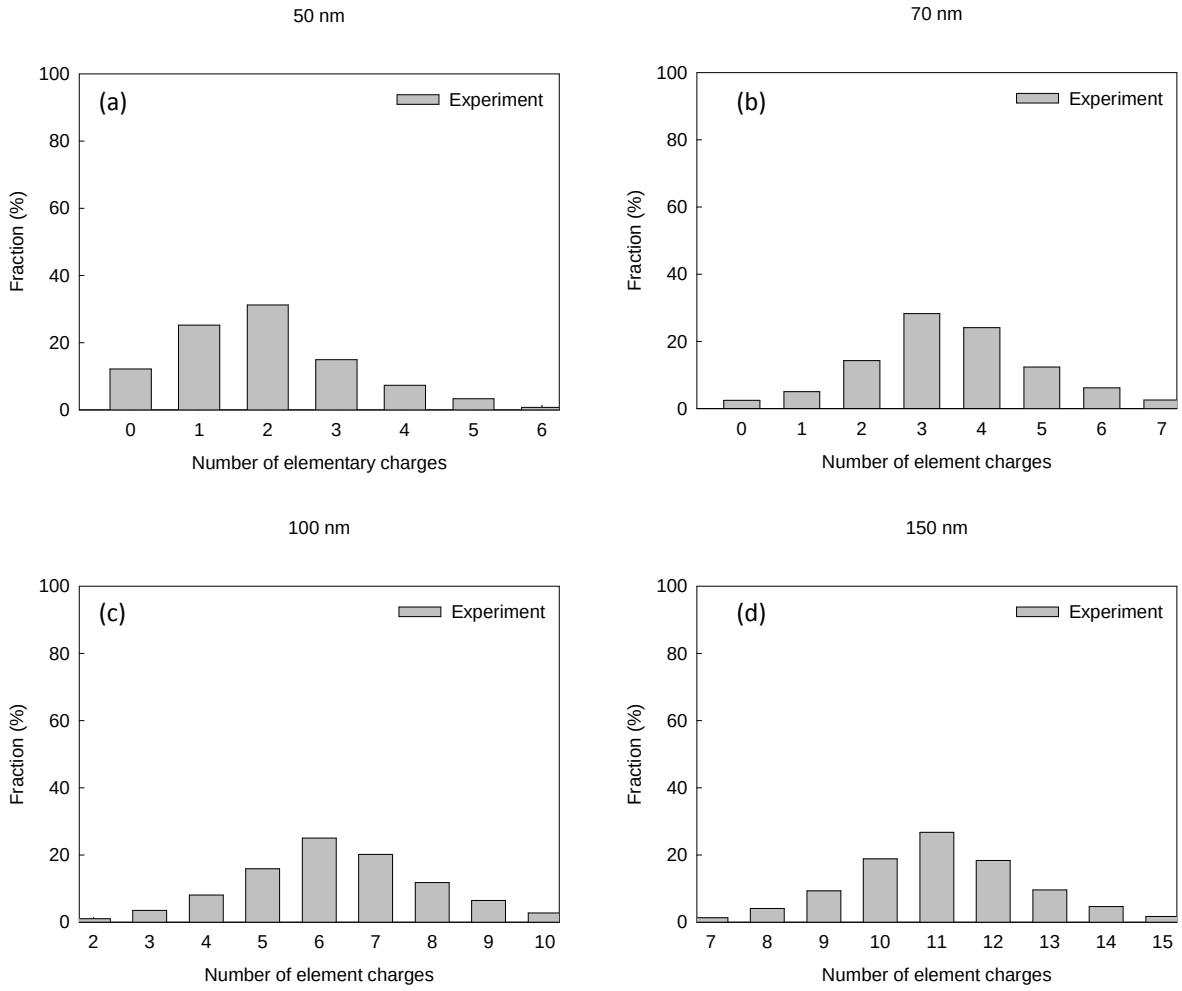

Figure 4.7 Extrinsic charge distributions of Fe_2O_3 particles with diameter from 50 to 150 nm at an aerosol flow rate of 5 lpm with four UV lamps

4.4.3 Effect of Irradiation Intensity

Fig. 4.8 shows the intrinsic charging efficiencies for Ag particles of diameters ranging from 5 to 30 nm, when the UV charger was operated at an aerosol flow rate of 5 lpm with one, two, or four lamps turned on. In all these cases, the diffusion charging is negligible because the ratio of the photionization rate to the diffusion charging rate $\alpha/(\beta N_i)$ is greater than 100. As reference, the intrinsic charge efficiencies calculated by the above discussed photocharging model are also plotted in Fig 4.8. The calculated

curves shown in Fig 4.8 represent the analytical solution to best fit the experimental data by varying the value of K_cI. The best fitted value of K_cI is also given in the legend of the figure. In this calculation, the wavelength of the pen-type UV lamps was set at 185 nm. However, when the wavelength was set at 254 nm, the maximum charge level of 15 and 25 nm Ag particles were 3 and 5 charges, respectively, according to Equation (4-11). However, from Figs 4.5(c) and 4.5(d), the charge status of 15 and 25 nm Ag particles are higher than those calculated using 254 nm wavelength. Thus the photocharging process in the studied UV charger is dominated by the irradiation with the wavelength of 185 nm.

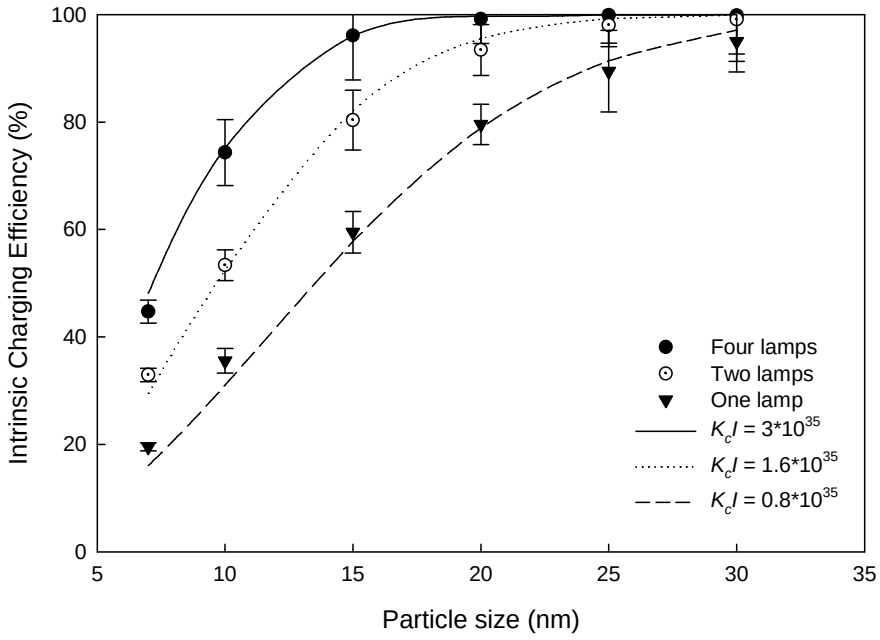

Figure 4.8 Comparison of intrinsic charging efficiencies of the UV charger for Ag particles in the size range from 7 to 30 nm at an aerosol flow rate of 5 lpm with one, two, and four UV lamps

For a given irradiation condition, a constant value of K_cI enables us to get a good fit to the corresponding intrinsic charging efficiency measured for test particles between 7 and 30 nm. We thus concluded that no dependence of the photoemission constant K_c on the particle size was observed for Ag particles in the tested size range. The aerosol photocharging model assumes that the light intensity in the irradiation zone of the UV charger is uniform. The discrepancy between the experimental and calculated efficiency data might be because of the spatial non-uniformity of the light intensity in the irradiation zone. Further, the ratio of the K_cI values at the three light intensity conditions is 3.75:2:1, close to the number ratio of UV lamps (i.e., 4:2:1) used in the corresponding cases. It is thus evident that the photoionization rate α is most likely proportional to the light intensity I.

Table 4.3 and Fig. 4.9(a-c) show the charge distributions of Ag particles with the diameter of 15 nm and at the concentration of approximately 2×10^4 #/cm^3 under the irradiation of various numbers of UV lamps. As reference, the intrinsic charge distributions calculated by the photocharging model are also given in Table 4.3 and Fig 4.9. The best-fitted K_cI values obtained from the intrinsic charging efficiency data were used in this calculation of particle charge distribution. As expected, particle charge distributions move towards the status of single charge with the decrease of light intensity. Reasonable agreement between the experimental and calculated charge distributions was obtained in our study. The discrepancy between measured and calculated charge distributions can be attributed to the loss of charged particles in the charger and the non-uniform light intensity in the irradiation zone.

Table 4.3 Comparison of extrinsic charge distributions of 15 nm Ag particles at the concentration of approximately 2×10^4 #/cm^3 with one, two, and four UV lamps

Number of elementary charges	Fraction (%)					
	Experiment (one lamp)	Model (K_cI=0.8×10^{35})	Experiment (two lamps)	Model (K_cI=1.2×10^{35})	Experiment (four lamps)	Model (K_cI=3×10^{35})
1	32.85	38.93	30.17	35.25	15.25	16.57
2	13.25	15.10	22.97	29.17	26.63	28.88
3	4.91	3.24	10.73	13.30	18.98	27.51
4	1.84	0.43	5.10	3.69	10.26	15.82
5	0.53	0.03	1.95	0.65	5.82	5.72
6	0.00	0.00	0.14	0.08	2.46	1.32

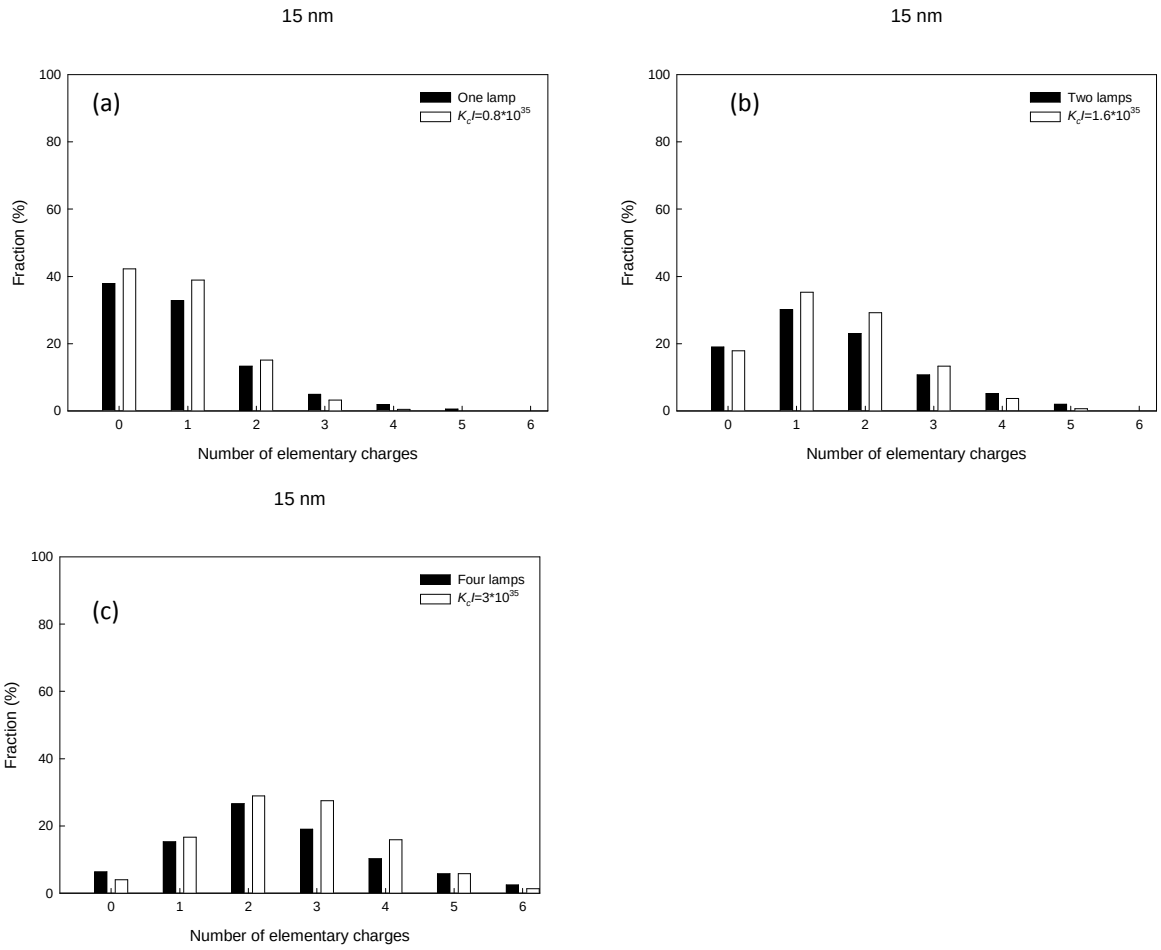

Figure 4.9 Comparison of extrinsic charge distributions of 15 nm Ag particles at the concentration of approximately 2×10^4 #/cm^3 with one, two, and four UV lamps

4.5 Summary

Particle photocharging for particles of various materials (i.e., Ag, Fe_2O_3, Co_3O_4, ZnO and TiO_2) has been investigated through a simple UV charger with pen-type UV lamps. The studied UV charger consists of a quartz tube about 7 in. long as the aerosol irradiation zone, four low-pressure Hg lamps located around the quartz tube, and an outer

cylindrical aluminum case with aerosol inlet at one end and outlet at the other end. The charger also has an ion trap section at the exit of the quartz tube to remove free ions.

We experimentally evaluated the performance of the UV charger operated at 5 lpm flow rate and with four UV lamps using monodisperse Ag with diameters from 7 to 30 nm and metal oxide particles with sizes ranging from 50 to 200 nm. We characterized both extrinsic and extrinsic charging efficiencies of the UV charger, and measured the charge distributions of particles passing through the UV charger using the electrostatic precipitation technique for particles of sizes larger than those studied in previous work. We also compared the performance of the UV charger to existing corona-based chargers. The studied UV charger provides higher extrinsic charging efficiencies than corona-based unipolar chargers for Ag particles. The extrinsic charging efficiency of the prototype is higher than 80% for particles of diameters larger than 15 nm. Depending on the material of test particles, the charging efficiency of the UV charger varies much, showing significant material dependence for the photocharging. Charge distributions of monodisperse Ag and Fe_2O_3 particles at the exit of the UV charger, operating at a 5 lpm aerosol flow rate and with four UV lamps turned on, were measured by the electrostatic precipitation technique. The charge distribution of 25 nm Ag particles is similar to that of 100 nm Fe_2O_3 particles, which further concludes the material dependence of the photocharging process.

To evaluate the effect of irradiation intensity on particle photocharging, we measured the charging efficiencies and charge distributions for Ag particles with sizes from 7 to 30 nm at an aerosol flow rate of 5 lpm, with one, two, or four lamps turned on. This study used the UV charging model with the photoemission following the Fowler-

Nordheim law to obtain the K_cI values at various operational conditions by best fitting to the measured intrinsic charging efficiency. The same K_cI values obtained above were then used in the charging model to calculate the charge distribution of particles. The study achieved reasonable agreement between calculated and measured charge distributions of particles.

Chapter 5

Review of Characterization of Particle Magnetic Moment

5.1 Instrument for Magnetic Moment Measurement

Particle magnetic moments are measured by different types of magnetometers, which are categorized into two groups (Czichos et al., 2006):

- The induction method, where a voltage is induced in an electrical circuit by the motion of the sample, e.g., the vibrating sample magnetometer (VSM), or a superconducting quantum interference device (SQUID) magnetometer for highest sensitivity;
- The force method, where the magnetic force on the sample is measured in a non-uniform magnetic field, e.g., the Faraday balance, or a magnetic force microscope (MFM).

The operations of VSM and SQUID magnetometers are based on the principle of Faraday's Law: any change in the magnetic field around a coil will create a corresponding electric field, which we can measure as an induced signal in the coil. The change can be produced by changing the magnetic field strength, altering the coil position by moving or rotating it in the magnetic field generated by a permanent magnetic material or electromagnetic coil. According to the induced signal, we can retrieve the information about the changing magnetic field.

The VSM is a widely used scientific instrument to determine the magnetic properties of various materials since its invention by Foner (1959). Generally, the VSM uses a stationary pick-up coil and a vibrating sample, but researchers have also proposed the reverse arrangement. A sample is placed in a uniform magnetic field between the poles of the electromagnet and vibrates in sinusoidal motion vertically to the field direction through the use of piezoelectricity, such as an electric motor or a transducer

similar to a loudspeaker system. The induced signal at the frequency of vibration in the suitably placed pick-up coil is proportional to the sample's magnetic moment, independent of the magnetic field (Czichos et al., 2006). Using the VSM, we can measure the magnetic properties of powders, bulk materials, and thin films, and study them as a function of magnetic field (hysteresis curve), temperature (thermomagnetic analysis), angle (anisotropy) and time.

Different from the VSM, the SQUID magnetometer has two superconductors, a superconducting pick-up coil and a superconducting quantum interference device (SQUID), separated by thin insulating layers to form two parallel Josephson junctions as the flux detector. Base on the DC Josephson effect, the input current is equally separated into the two branches without a magnetic field. If there is an external magnetic flux through the superconducting loop, the device will generate a biasing current to provide a magnetic field to compensate for the flux change. If the induced current is larger than the critical current for the Josephson junction, the superconductor becomes resistive, and a voltage is produced. With further increase of the external flux, the measured voltage oscillates with changes in direction at the two junctions. If the original input current is higher than the critical current, the SQUID is always in the resistive mode, and the output signal is proportional to the current, which is a function of the external magnetic field (Clarke, 1994). The SQUID magnetomter is about 1000 times more sensitive than the VSM for the magnetic moment measurement. For example, a commercial VSM system offers measuring capabilities down to approximately 10^{-9} Am^2, while the SQUID magnetometer with a SQUID sensor rather than a pick-up coil reached a detection limit of 10^{-12} Am^2 (Czichos et al., 2006). Similar to the VSM, the SQUID magnetometer can

measure the magnetic moment of a sample, from which the magnetization and magnetic susceptibility can be further retrieved. Moreover, it is definitely a better choice than the VSM when high sensitivity is required for the measurement, e.g., a sample with a low magnetic moment or a low mass.

In the force method, the magnetic force on the sample in a magnetic field, which is a function of the magnetic moment or susceptibility of the sample, is measured by a sensitive balance or a force transducer.

Faraday balance and Gouy balance are similar to each other. A pair of magnets is placed at one end of a balanced system, which generates a magnetic field strength *H*. When a sample is suspended between the poles of the magnets, the magnetic force acting on the sample is proportional to its magnetic susceptibility χ. In the Faraday balance, the force is expressed as $F = V\chi H \frac{dH}{dz}$, where *V* is the volume of the sample. Since the pole caps of the magnets are shaped so that the product *H(dH/dz)* is constant over a considerable range in vertical direction *z* on the symmetry axis of the magnet, it is easy to evaluate the magnetic susceptibility of a sample from the measured force. The Faraday method is suitable for all kinds of materials, especially ferro- and ferrimagentic specimens (Czichos et al., 2006). In the Gouy balance, the sample with long cylindrical shape is suspended from a balance, so that one end is located between the poles of an electromagnet. The other end, outside the poles, is affected by the stray field strength much less than that between the poles. The magnetic force exerted on the sample is in the form of $F \approx \frac{1}{2} A\chi H^2$, where *A* is the cross-sectional area of the sample. The Gouy method is mainly used for para- and diamagnetic materials including liquids and gases.

Recently, magnetic moment per unit mass of magnetic nanoparticles was found by using the atomic force microscope (AFM) (Park et al., 2008). A microfabricated force transducer measured the magnetic force of the tested sample by with the expression $F = M(H)m\frac{dH}{dz}$, where *M(H)* is the magnetization per unit mass of the material, *m* is the mass of sample determined from the resonance frequency shift of the particle-attached AFM probe, and *dH/dz* is the magnetic field gradient. The magnetization curve of the nanoparticles was determined as a function of magnetic field strength.

All these methods are used for off-line analysis, which means it takes significant time to collect samples of sufficient material before the measurements can be performed.

The first measurement technique allowing on-line measurement of particle magnetic properties was introduced by Kauffeldt et al. (1993). It responds to micromagnetism of non-interacting particles rather than the collective magnetization of a powder. This method used a set of wire mesh Nickel screens to establish a high gradient magnetic field for removing magnetic nanoparticles from their carry gas stream. The particle number concentration upstream and downstream of the filter was measured by an Ultrafine Condensation Particle Counter (UCPC). The single fiber efficiency was derived directly from the measured data as a function of particle size, particle magnetic moment and fiber magnetization. A numerical model using particle trajectory analysis was developed, and the magnetic moments of iron/iron oxide particles ranging from 40 to 170 nm with single magnetic domain were obtained (Kauffeldt et al., 1996).

The magnetic filter provides new opportunities for basic research of magnetic particles and is a tool to optimize magnetic particle generation combined with aerosol methods of size classification (Kauffeldt et al., 1997). Agglomerates of oxidized iron

particles were produced in the size range from 10 to 200 nm and investigated with respect to particle size, shape and particle magnetic moment by the above method and scanning transmission electron microscopy (Kauffeldt et al., 1995). The magnetic moment is increased by formation of more chain-like agglomerates due to the aligned coagulation, in which the primary magnetic moments are aligned more in parallel.

This method of using a set of wire mesh magnetic filters to remove nanometer-sized magnetic particles is called high gradient magnetic separation (HGMS). Coupled with novel techniques, e.g., magnetic seeding in which magnetic particles as a coagulant flocculate with non-magnetic materials, and functionalized particles in which magnetic particles have a strong binding to non-magnetic substances, HGMS is widely used in the treatment of biological fluids, of industrial fluids, and of wastewater (Rembaum et al., 1982; Miltenyiet al., 1990; Moeser et al., 2002; Bucak et al., 2003; Chen et al., 2007a; Anand, 1985; Shaikh and Dixit, 1992; Nedelcu and Watson 2002, Newns and Pascoe 2002, Karapinar 2003).

5.2 Modeling of Magnetic Filters

Significant effort has been made to simulate the particle capture process in the magnetic filters since the introduction of HGMS. The technique makes use of small magnetic wires as filter elements, which generate local gradients in a uniform magnetic field. By increasing the magnetic field gradient around the fiber, particles with very weak magnetization can be attracted to its surface through the magnetic force from the carrier fluids, which is impossible in the traditional filtration and magnetic separation methods.

Particle trajectory models, consisting of partial differential equations that dynamically simulate the influence of various forces on the motion of a single particle toward a single fiber, have been use to calculate the capture cross section. In this kind of system, the capture cross section is the maximum perpendicular distance in which the released particles can pass through the fiber and still be retained. It depends on many factors, e.g., the size and magnetic properties of the suspended particle and the wire, the flow and magnetic field, and the physical properties of the liquid, such as density and viscosity. Most of the trajectory models only emphasized two particular configurations: longitudinal when the magnetic field and fluid flow are perpendicular to the fiber and both parallel to each other and transverse when the magnetic field, fluid flow, and fiber are perpendicular to each other (Cowen et al., 1976; Gerber, 1994; Gerber and Birss, 1983; Luborsky and Drummond, 1975; Watson, 1973, 1978b). With the accumulation of particles on the surface of the fiber, the flow and magnetic field may be changed. Moreover, the inter-particle forces may also need to be considered to simulate the loading behavior of the filter (Akoto, 1977; Chen et al., 2007b; Cowen and Friedlaender, 1977; Cowen et al., 1976; Gerber, 1994; Gerber and Lawson, 1989; Gerber and Birss, 1983; Luborsky and Drummond, 1975; Watson, 1978a, Ying et al., 2000).

Watson (1973) developed a trajectory model and found the capture cross section as a function of the ratio of the particle face velocity to the magnetic velocity. It is valid at low magnetic field conditions over a clean wire for both the longitudinal configuration and the transverse configuration (Gerber, 1994; Gerber and Birss, 1983). Later, Luborsky and Drummond (1975) extended this model by considering ribbon and rod-like wires instead of cylindrical ones. Clarkson et al. (1976) improved this model by adding the

gravitational and the inertial forces. However, this trajectory model overlooks the effect of the short-range term ($M_f/2H$) of the radial component of the magnetic force, where M_f and H are the fiber magnetization and applied external magnetic field, respectively. Cowen et al. (1976) made adjustments to this limitation, but only when the fiber and the particles are of equal size. Gerber et al. (Gerber and Birss, 1983; Gerber, 1994) further improved the correlations for a wider spectrum of conditions from analytical approximations of trajectory models for both the transverse and longitudinal configurations. However, the main restriction of these correlations is only suitable for extreme values of the magnetic field (i.e., only at low and high values), and therefore lack the continuity in the middle. Ebner and Ritter (2001) resolved this problem with the introduction of a new parameter. The new correlation covered much wider ranges of operation conditions and physical properties for both the longitudinal and transverse configurations. However, it only considered the situation where the fiber was clean and was appropriate for the early stages of the magnetic filtration process.

For the magnetic filter developed by Kauffeldt et al (1996), particle trajectory models were developed to retrieve the magnetic moment of particles from the measured penetration difference between the case that applied an external magnetic field and the case that did not (Kauffeldt et al., 1996; Zarutskaya and Shapiro, 2000). These models assumed that the particle magnetic moment is independent of the applied external magnetic field. The combined effect of the Brownian motion and particle rotation on the particle capture efficiency does not exceed more than a few percent. Accordingly, in modeling the magnetically assisted capture, we may effectively assume the particles to be diffusionless and to have their magnetic moment vectors oriented along the local

magnetic field. The influence of filtration operating conditions and particle diameters on the particles' behavior and magnetic capture efficiency was investigated numerically. Strong dependence of the capture efficiency on the particle diameter was found for particles with the diameter less than 200 nm.

However, these models were not experimentally validated prior to their use. The actual magnetic moment of the test particles used in the experiment was not characterized by other reference methods (for example, VSM or AFM), nor was it compared with that obtained via the models themselves. Furthermore, these models did not consider the effects of flow and magnetic field variation due to the presence of woven wires, although in reality the magnetic filter is constructed of well-defined mesh screens.

Chapter 6

Calibration and Modeling of a Magnetic Filter

6.1 Introduction

In this study, a magnetic filter consisting of ten SS 430 screens with 200 mesh was designed and tested using monodisperse γ-Fe_2O_3 particles ranging in size from 100 to 300 nm at different flow rates. To obtain the particles' magnetic susceptibility, we developed a particle trajectory model to describe the behavior and collection of magnetic particles from carry gas in the magnetic filter. To validate the proposed model, we compared the magnetic susceptibility of particles obtained from the proposed model to that obtained from VSM. Further, the effects of filtration operation conditions and particle diameters on their behavior and magnetic capture efficiency were numerically investigated.

6.2 Design and Evaluation of Magnetic Filter System

Fig. 6.1 shows the schematic diagram of the studied magnetic filter system, in which a set of parallel screens were used as the filtration element, similar to that used in a screen-type diffusion battery (Cheng and Yeh, 1980). The dimensions of the magnetic filter system are also included in the same figure. The metal mesh screens were made of SS 430 magnetic wires. The carrier gas loaded with magnetic particles flowed through the filter element in the direction perpendicular to the screens. The screens were then magnetized by an external magnetic field, also in the direction perpendicular to the screens. The external magnetic field was generated by an electric coil wound around the case of the filter element holder. With the system configuration, the deposition of particles in the magnetic filter element is governed by the magnetic force experienced by particles when moving nearby the magnetized wires of the screens. The magnetic force

experienced by particles is, in general, a function of the particle size, particle magnetic property, and wire magnetization.

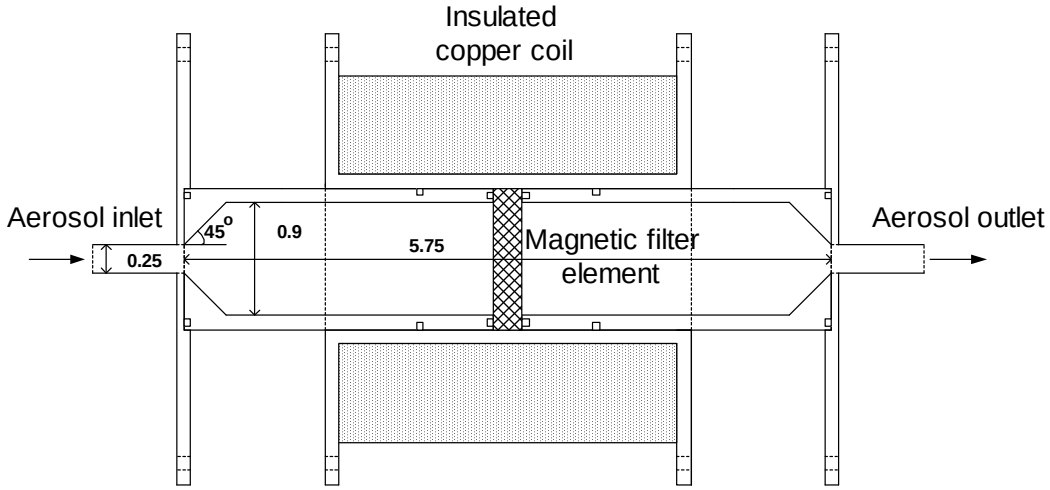

Figure 6.1 Schematic diagram of the studied magnetic filter system

Fig. 6.2 shows the experimental setup for the penetration measurement of the magnetic filter element. Magnetic γ-Fe_2O_3 particles (Sigma-Aldrich 544884) were aerosolized with a home-made Collison atomizer (Liu and Lee, 1974a). The output flow rate from the atomizer was 4.0 lpm at 30 psig for inlet air pressure. Droplets produced by the atomizer were passed first through a Po^{210} radioactive neutralizer to minimize the electrical charges on the particles, and then through a diffusion dryer with silicone gel as the desiccant to remove the solvent in the droplets.

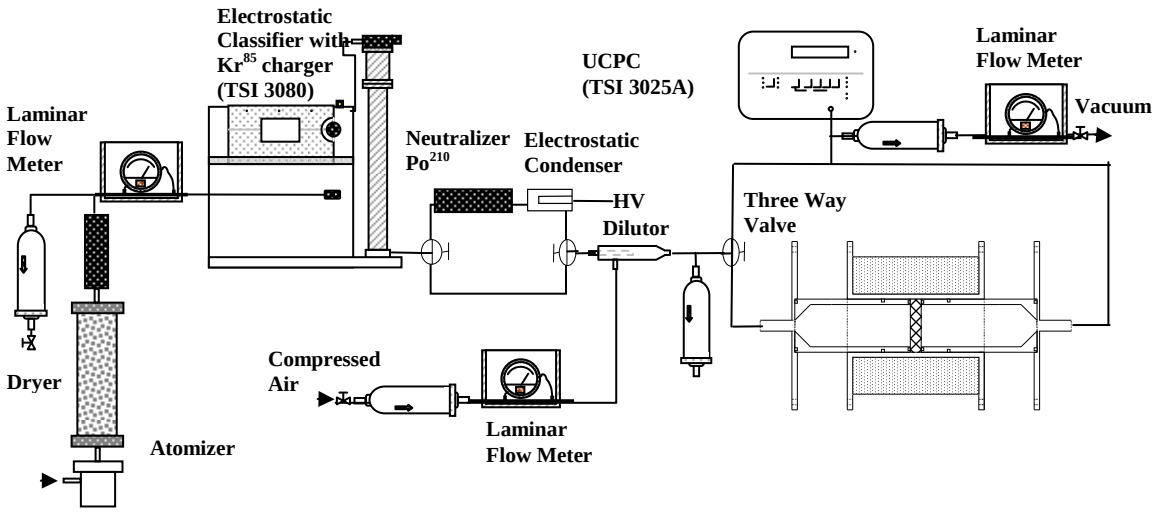

Figure 6.2 Schematic diagram of the experimental setup for the evaluation of magnetic filter system

A differential mobility analyzer (DMA, TSI Model 3081) was used in the downstream of the above-described polydisperse aerosol generation system to classify monodisperse particles ranging in size from 100 to 300 nm. A Kr^{85} radioactive particle charger was used to place a well-defined charge distribution on polydisperse particles prior to the introduction of the DMA. The DMA was operated at an aerosol flow rate of 1.5 lpm and a sheath flow rate of 10.0 lpm. Since the particles exiting from the DMA are electrically charged, a Po^{210} neutralizer and an electrostatic precipitator were utilized at the DMA exit to obtain electrically neutral particles for testing. The total flow rate through the magnetic filter element was controlled by both the pump of the Ultrafine Condensation Particle Counter (UCPC, TSI model 3025A), operated at a flow rate of 1.5 lpm, and a separate vacuum pump with a needle valve to adjust the desired flow rate. The aerosol stream from the three way valve to the UCPC was equally separated into two

pathways: one with the magnetic filter and one without. The tubing length of each pathway was about 20 cm. The particle number concentrations upstream and downstream of the magnetic filter were measured by UCPC. The upstream concentrations of monodisperse test particles were on the order of 10^3~10^4 #/cm^3. Particle coagulation can be neglected during the transportation process. The transmission efficiency, defined as the ratio of downstream concentration to the upstream one without the filter element, was around 98% or even higher. So particle transport loss in the duct wall is negligible. The particle penetration P through the magnetic filter with the element was then obtained by a ratio of the particle downstream concentration N_{dn} to the upstream one N_{up}:

$$Penetration = \frac{N_{dn}}{N_{up}}. \tag{6-1}$$

6.3 Modeling of Magnetic Filter Element

The measured penetration P through the studied magnetic filter element, which is a function of particle size, particle magnetic property, and wire magnetization, could be predicted by calculating the fate of individual particles, and hence the capture of particles in the magnetic filter element. To determine the particle fate in the filter element, the flow and magnetic fields must be first calculated.

6.3.1 Calculation of Flow and Magnetic Fields

The finite element package COMSOL Multiphysics 3.5 was used to numerically solve the flow and magnetic fields in the magnetic filter element. To reduce the geometrical complexity of the filter element, we assume that a single metal screen can be represented by the replica of unit cells, as shown in Fig. 6.3. According to the SEM micrograph, the wire diameter and spacing for the single 200 mesh SS 430 screen are

about 40.5 and 86.5 μm, respectively. A wire cross with the diameter D_f of 41 μm was used in a standard cell. Since the spacing between the two adjacent mesh screens in the filter element was set at 0.5 mm, the volume of the unit cell was set at 130*130*550 μm^3.

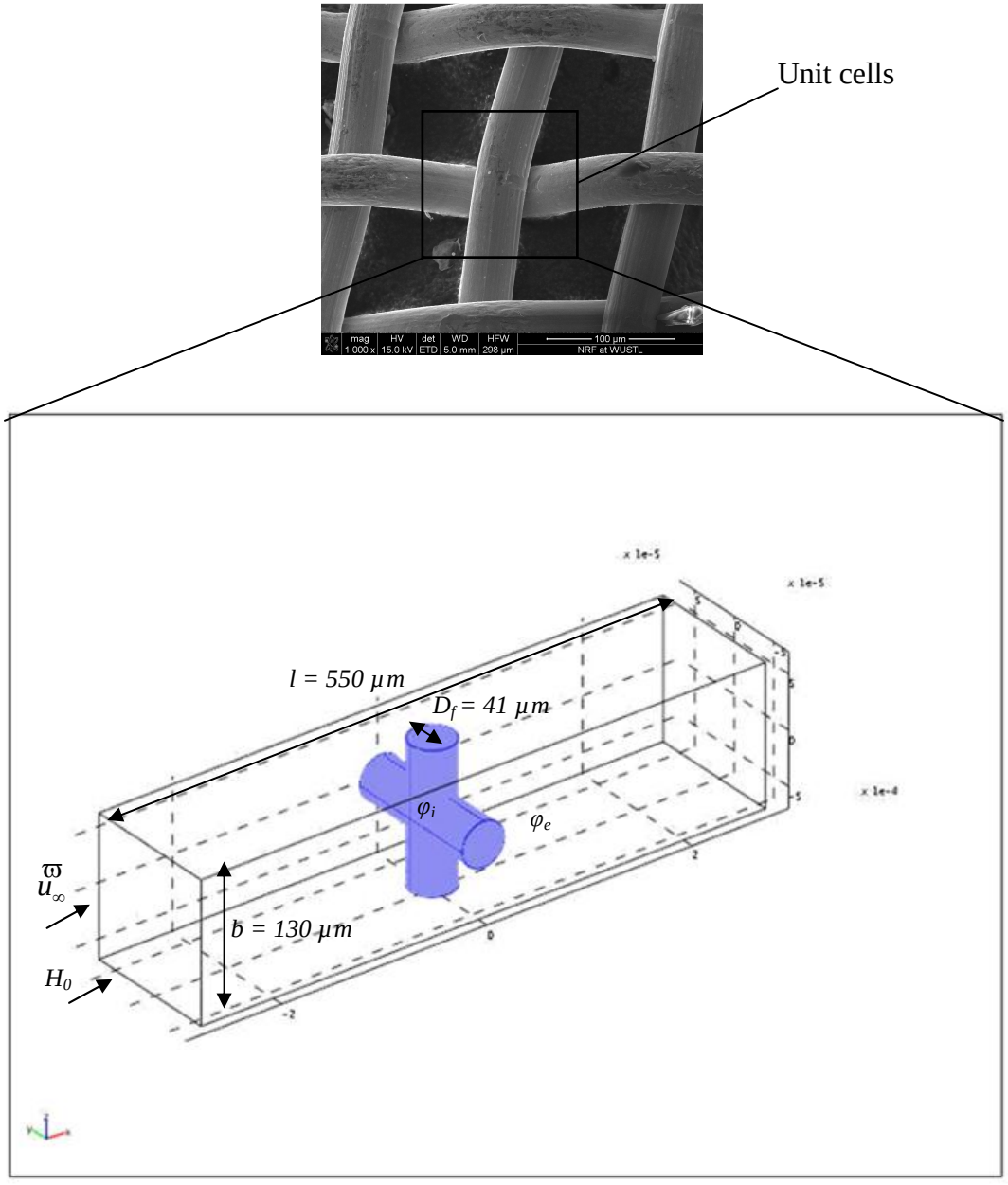

Figure 6.3 Computational domain for a unit cell as the basic elements for a single mesh screen

The flow field in the unit cell was calculated by solving the continuity and 3D Navier-Stokes equations with the assumption of incompressible fluid having density ρ and viscosity η:

$$\nabla \cdot \vec{u} = 0 \tag{6-2}$$

$$\rho[\frac{\partial \vec{u}}{\partial t} + (\nabla \vec{u}) \cdot \vec{u}] = -\nabla P + \eta \nabla^2 \vec{u}. \tag{6-3}$$

The inlet flow velocity was probably constant, uniform and equal to the face velocity $\vec{u}_\infty$ of the filter element, entering the cell in the x-direction. No slip boundary conditions were applied at the wire surface. Symmetric conditions were applied to the surrounding boundaries due to the replica of unit cells. The detail settings of boundary conditions in COMSOL are shown in Table 6.1. A typical example of the calculated flow field in a unit cell is given in Fig. 6.4.

Table 6.1 Settings of boundary conditions in COMSOL

Boundary	Flow field condition	Magnetic field condition
Inlet	Velocity $\vec{u} = \vec{u}_\infty$	Magnetic insulation
Outlet	Pressure, No Viscous Stress	Magnetic insulation
Wire surface	Wall No Slip $\vec{u} = 0$	Continuous
Surrounding	Symmetry boundary	Magnetic insulation

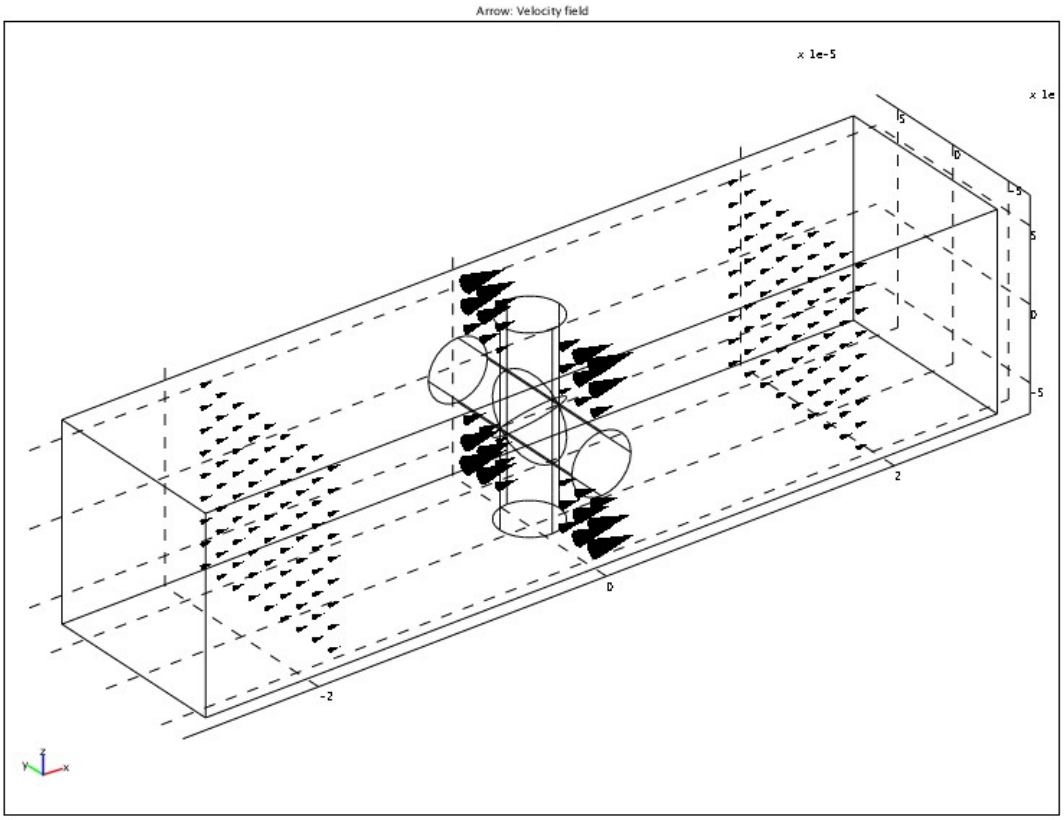

Figure 6.4 Flow field in the unit cell at the aerosol flow rate of 0.06 m/s

The magnetic force upon magnetic particles was determined by evaluating the magnetic field $\vec{H}$ in the unit cell. To calculate the magnetic field in a unit cell, the computational domain was divided into two regions with very distinct magnetic behaviors. One is the non-magnetizable region, which is unoccupied by the wires, and the other is the magnetized region occupied by the wires. The Maxwell equations for conservative magnetic fields were used within these two regions:

$$\nabla^2 \varphi_i = 0 \tag{6-4}$$

$$\nabla^2 \varphi_e = 0, \tag{6-5}$$

where φ_i and φ_e are the scalar magnetic potentials for wire-occupied and non-magnetizable regions, respectively, and are related to the magnetic field strengths $\vec{H}_i$ and $\vec{H}_e$ according to

$$\vec{H}_i = -\nabla \varphi_i \tag{6-6}$$

$$\vec{H}_e = -\nabla \varphi_e . \tag{6-7}$$

Considering the demagnetization factor, when the applied magnetic field $\vec{H}_0$ measured by AlphaLab DC magnetometer is perpendicular to the wire principle axis, the internal magnetic field $\vec{H}_i$ could be expressed as (Watson, 1978b):

$$\vec{H}_i = \vec{H}_0 - \vec{M}_f / 2\mu_0 , \tag{6-8}$$

where μ_0 is the magnetic permeability of free space. The magnetic induction $\vec{B}$ is then expressed as

$$\vec{B}_i = \mu_0(\vec{H}_i + \vec{M}_f) , \tag{6-9}$$

where $\vec{M}_f$ is the wire magnetization, measured by VSM, as a function of the external magnetic field, e.g., the wire magnetization are 83.6 and 160.8 kA/m at the magnetic field of 20 and 40 kA/m, respectively.

At the wire surface, the continuities of magnetic potentials (i.e., φ_i and φ_e) and normal magnetic fluxes (i.e., $\vec{B}_i$ and $\vec{B}_e$) in wire-occupied and un-magnetizable regions were applied. The symmetric conditions were applied to the surrounding boundaries due to cell replication. The detail settings of boundary conditions in COMSOL are shown in Table 6.1. Fig. 6.5 shows a typical example of the normal magnetic field in a unit cell.

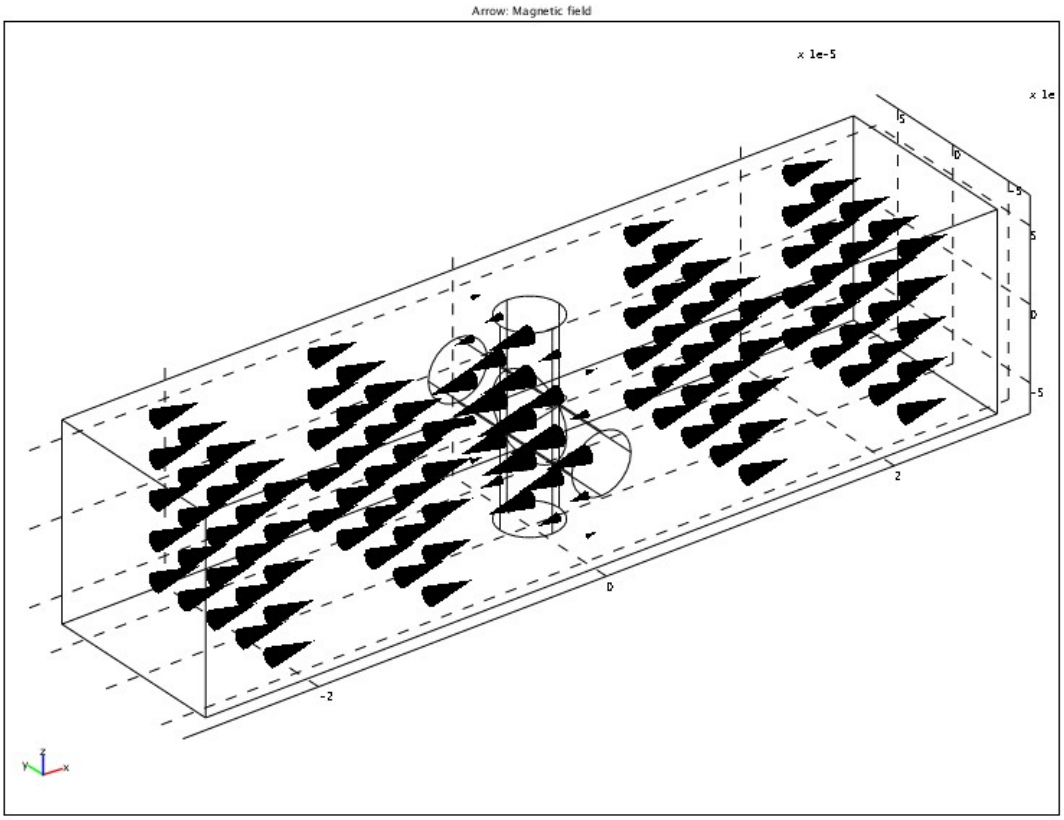

Figure 6.5 Magnetic field in the unit at the external magnetic field strength of 20 kA/m

6.3.2 Calculation of Individual Particle Trajectories

Particle penetration through a unit cell can be calculated by indentifying the limiting trajectory of approaching particles, which can be divided into those that end by colliding on the wire cross surface and those that simply pass the wire cross surface. The above modeling idea is illustrated in Fig. 6.6.

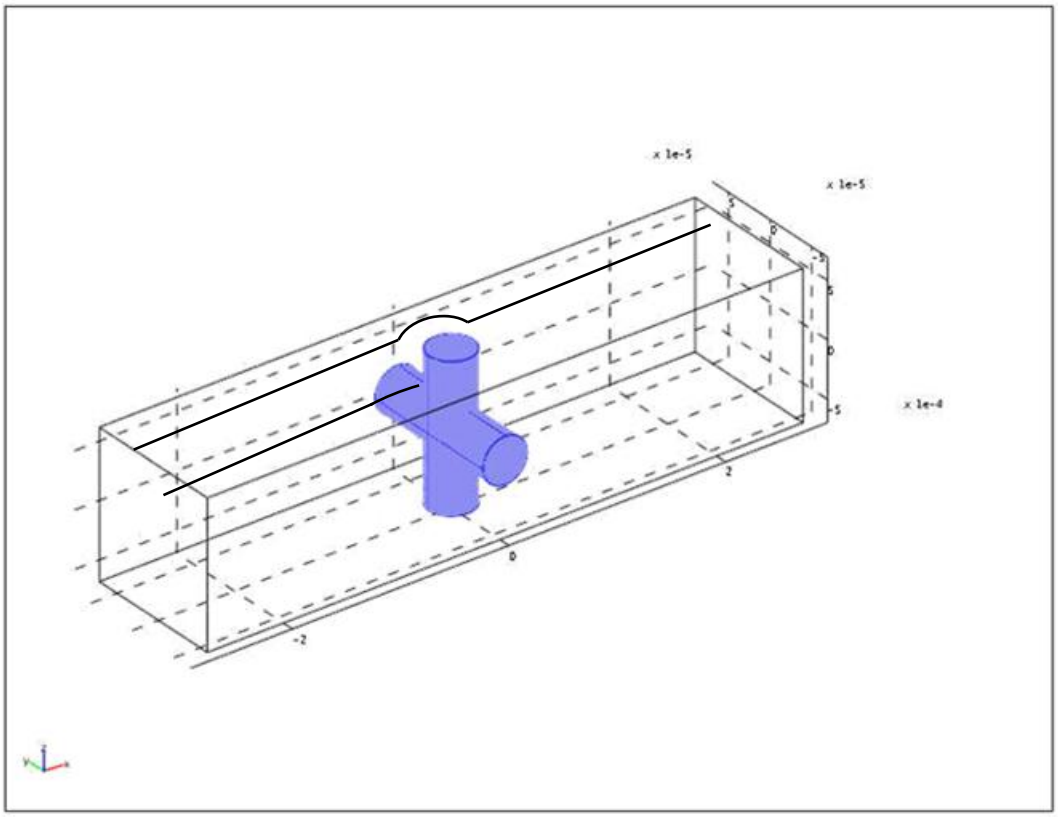

Figure 6.6 Illustration of limiting particle trajectory idea for particle penetration calculation

The following assumptions were used to calculate of individual particle trajectory:

a) According to the previous study of Zarutskaya and Shapiro (2000), particles are spherical in shape, and their rotational effects are negligible. Particles' magnetic susceptibility is assumed to be constant, and their magnetic moments are assumed to be oriented in the direction of the magnetic field.

b) Under a low Reynolds number flow system, the particle trajectory can be calculated by the force balance equation, including gravitational ($\vec{F}_g$), magnetic ($\vec{F}_m$), drag ($\vec{F}_d$), and random ($\vec{F}_{br}$) forces.

c) No particle re-entrainment occurs, and deposited particles do not significantly alter the flow and magnetic fields in the unit cell.

The trajectory of a submicron particle moving in a gas with velocity $\vec{v}$ under the action of gravitational, magnetic, drag, and random forces is determined by the force balance equations based on the Newton's second law.

$$m_p \frac{d\vec{v}}{dt} = \vec{F}_d + \vec{F}_g + \vec{F}_m + \vec{F}_{br} \tag{6-10}$$

Particle drag force $\vec{F}_d$ is expressed as

$$\vec{F}_d = f(\vec{u} - \vec{v}). \tag{6-11}$$

Here, m_p is the particle mass; t the time variable; $\vec{u}$ the flow velocity vector; and f the particle friction coefficient given by the Stokes law as $f = 3\pi\mu d_p/C$ (Friedlander, 2000), where C is the Cunningham slip correction factor, expressed as

$$C = 1 + \frac{2\lambda}{d_p}(1.142 + 0.558 \times \exp(-\frac{0.999 d_p}{2\lambda})), \tag{6-12}$$

where λ is the mean free path.

Because of the small size of particles, the magnetic field in the particle is assumed to be approximately uniform. Further, the magnetic interaction between particles is neglected due to the low concentration of testing particles. The following expression was then used to evaluate the magnetic force $\vec{F}_m$ on a magnetic particle:

$$\vec{F}_m = \mu_0 \nabla(\vec{M} \cdot \vec{H}), \tag{6-13}$$

where μ_0 is the magnetic permeability of free space, $\vec{H}$ the magnetic field strength, and $\vec{M}$ the particle magnetic moment, whose scale is related to the magnetization of particle by

$$M = \frac{\chi}{1+\chi/3} H V_p , \tag{6-14}$$

where χ is the particle magnetic susceptibility, and V_p the particle volume (O'Handley, 2000).

In Brownian motion, a particle at time t and position p will make a random displacement r from its previous point with regard to time and position. The resulting distribution of r is expected to be (1) Gaussian (normal with a mean of zero and a standard deviation of one), (2) to be independent, and (3) have a root mean square displacement of $\sqrt{2Dt}$ in its x, y, and z coordinates. The random displacement *r* in one coordinate can be calculated as

$$r = \frac{\sqrt{2Dt}}{\sqrt{2\pi}} e^{-\frac{\xi^2}{2}} , \tag{6-15}$$

where ξ is a random number.

The trajectory for a given particle was determined by solving Eq. (6-10) using the Runge-Kutta method of the 4^{th} order. As shown in Fig 6.7, the uniform particle concentration profile was assumed at the cell entrance, which was divided into 130*130 squares. A single particle was released from the center of each square up to 100 times. The cell collection efficiency E_c is the ratio of the number of particles *N* captured by the wire cross to the number of particles N_0 entering the cell:

$$E_c = \frac{N}{N_0} \tag{6-16}$$

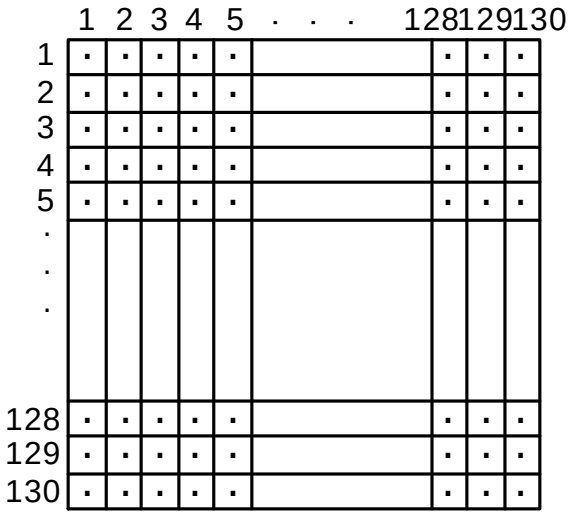

Figure 6.7 Particle release profile at the cell entrance

Since cell efficiency represents the presence of a single mesh screen, the overall penetration P through n screens can then be calculated by (Brown, 1993):

$$P = exp(-nE_c). \tag{6-17}$$

As a summary of all the modeled cases, the values and dimensions of the parameters used in our numerical study are given in Table 6.2.

Table 6.2 Values and dimensions of the parameters used in the modeling

Parameters	Units	Values
Fluid density	Kg m^{-3}	1.2
Fluid viscosity	$Kg(ms)^{-1}$	1.81E-5
Fluid temperature	T	298
Mean fluid velocity	m/s	0.06~0.22
Reynolds number of system		91~332
Reynolds number of wire		0.16~0.6
Fiber diameter	μm	41
Magnetic field strength	kA/m	20, 40
Particle density	Kg m^{-3}	5242 (γ-Fe_2O_3) 1.98 (KCl)
Particle size	nm	100~300 (γ-Fe_2O_3) 50~300 (KCl)

6.4 Model Validation and Analysis

To verify the numerical model, we first compared the calculated penetration with the experimental one for the case of potassium chloride, KCl, particles, in which the particle magnetic force is negligible. Fig. 6.8 compares of the calculated and the experimental penetrations through the magnetic filter element at different carry gas flow rates for KCl particles ranging in size from 50 to 300. The standard deviation for each data point includes the UCPC fluctuation. Good agreement between numerical and experimental penetration data was obtained in the studied size range. For the case of 50

nm particles, the calculated penetration is slightly higher than the experimental. It may be attributed to the pre-set time step for the particle trajectory calculation. The pre-set time step for marching a particle in the unit cell may be large enough that particle collection on the wire cross may be underestimated due to the particle diffusion process.

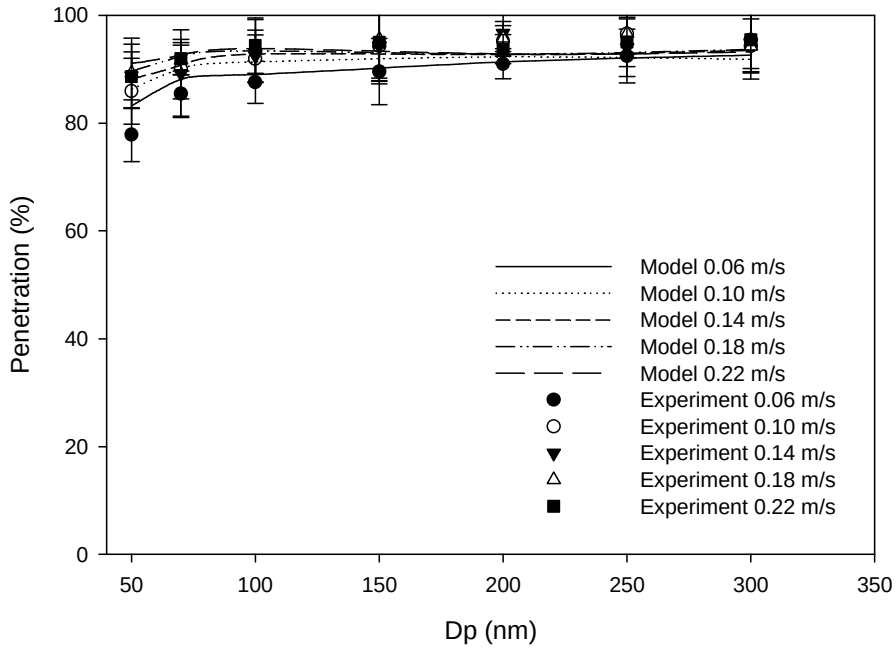

Figure 6.8 Comparison of calculated and experimental penetration through the magnetic filter element at different flow rates for KCl particles in the size range from 50 nm to 300 nm

Before the validation of numerical model with magnetic force, we measured the magnetic susceptibility of 100, 150, and 250 nm γ-Fe_2O_3 particles by VSM. Monodisperse γ-Fe_2O_3 particles downstream of the DMA were collected using a precipitator and filled into a small sealed glass tube for the characterization. Fig. 6.9 shows the magnetization curve of 150 nm γ-Fe_2O_3 particles as an example. The magnetic

susceptibility is defined as the slope of the initial magnetization curve as a function of magnetic field, e.g., 2.6 for 150 nm γ-Fe_2O_3 particles at the magnetic field of 20 and 40 kA/m.

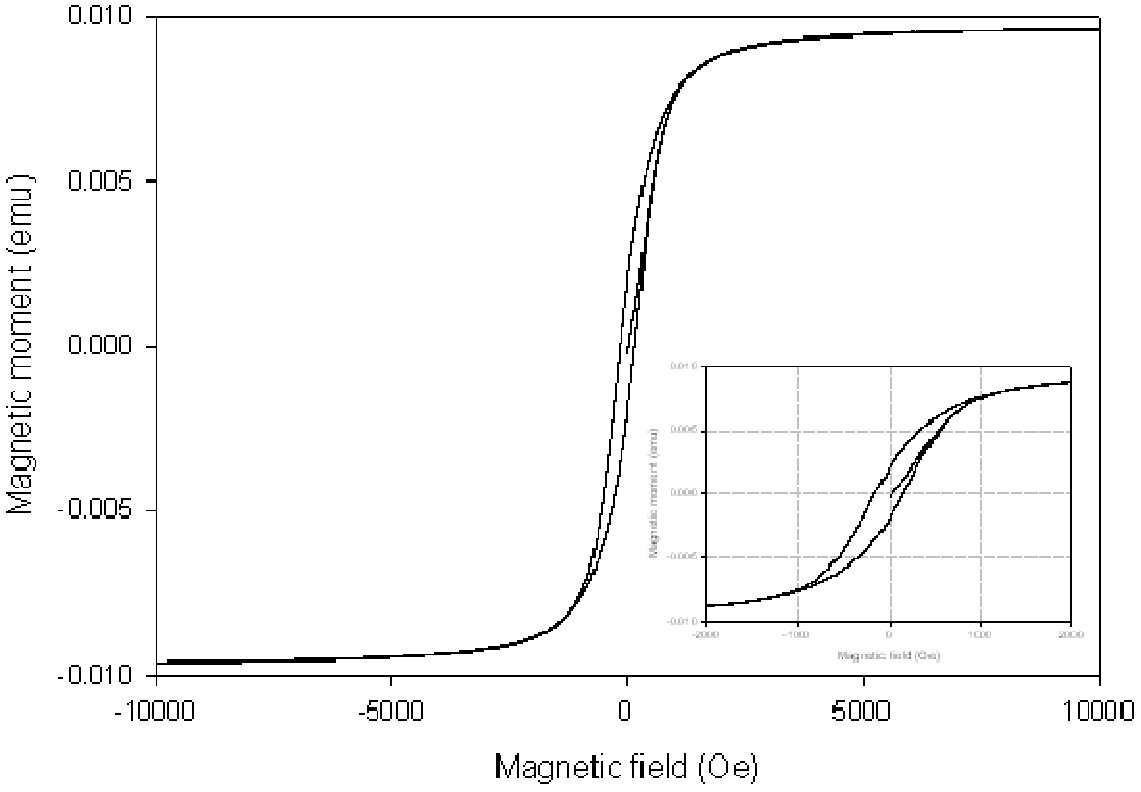

Figure 6.9 Characterization of 150 nm γ-Fe_2O_3 particles by VSM

To further verify the numerical model with magnetic force, we compared numerical penetration with experimental penetration through the magnetic filter element at different flow rates for 100, 150, and 250 nm γ-Fe_2O_3 particles in the estimated external magnetic fields of both 20 and 40 kA/m as shown in Fig. 6.10. The numerical penetration was calculated using the proposed model base on the measured magnetic susceptibility data by VSM. We found that particle penetration increases with an increase

in aerosol flow velocity and decreases with an increase in external magnetic field strength as well as particle size. The good agreement between the calculated and the experimental penetrations validates our numerical model. In general, the discrepancy between the experimental and the calculated penetration is less than 10%.

(a) 20 kA/m

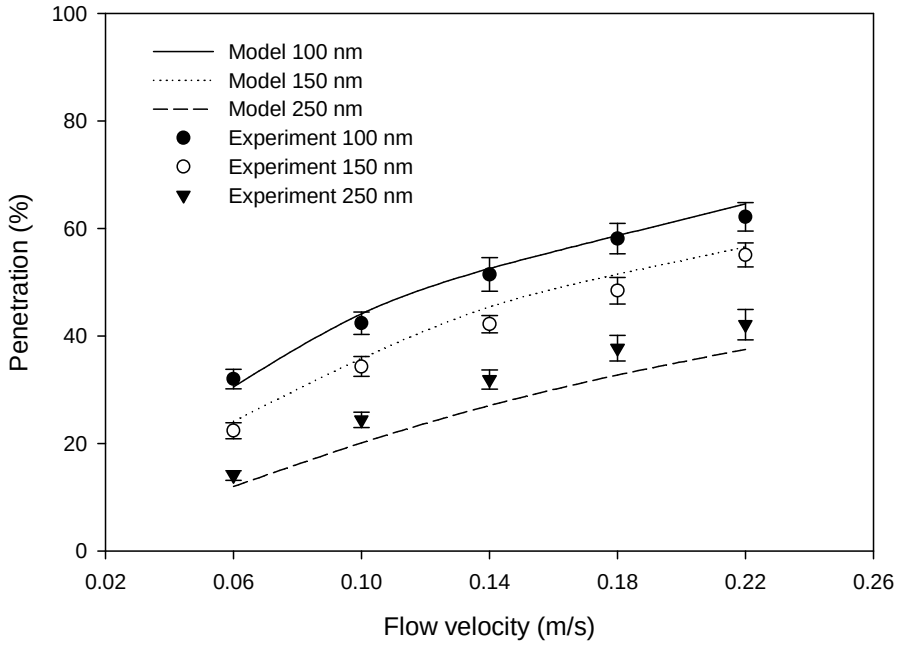

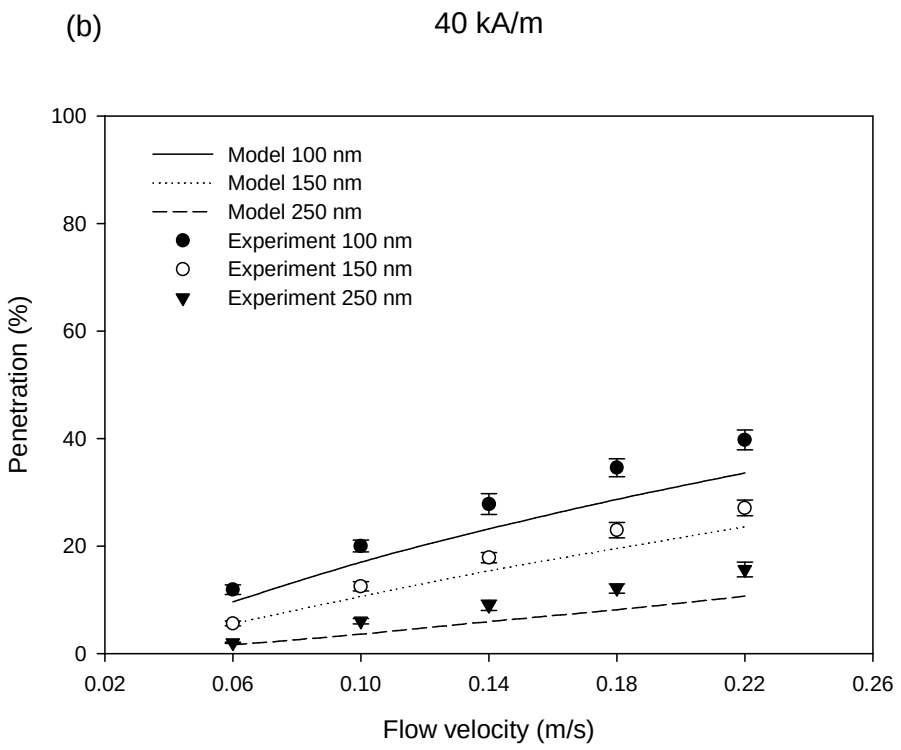

Figure 6.10 Comparison of calculated and experimental penetration through the magnetic filter element for 100, 150, and 250 nm γ-Fe_2O_3 particles at estimated 20 and 40 kA/m external magnetic field and different flow rates

With this model, the particle penetration curves through the magnetic filter element as a function of magnetic susceptibility were first calculated for γ-Fe_2O_3 particles in size ranging from 100 to 300 nm at different flow rates and in the external magnetic fields of 20 and 40 kA/m. From the above-calculated curves, the correlated particle magnetic susceptibility was then retrieved from the measured particle penetration data. The derived magnetic susceptibility of studied γ-Fe_2O_3 particles as a function of particle size is shown in Fig. 6.11. According to the calculated curve, the standard deviation of the magnetic susceptibility was determined from that of the penetration data, which includes the flow fluctuation of the UCPC. Generally, the derived magnetic susceptibility

of γ-Fe_2O_3 particles is in the same order of magnitude. However, a slight difference between the external magnetic field of 20 kA/m and the external magnetic field of 40 kA/m are observed, especially in the smaller particle sizes. Note that the particle magnetic susceptibility χ was assumed constant in our model even though particles may experience different magnetic field strengths in the particle trajectory calculation. For ferrimagnetic materials, the theoretical relationship between magnetization and magnetic field strength is not linear, indicating that magnetic susceptibility is a function of magnetic field strength. It may be why a small deviation is observed between the two different magnetic field strengths.

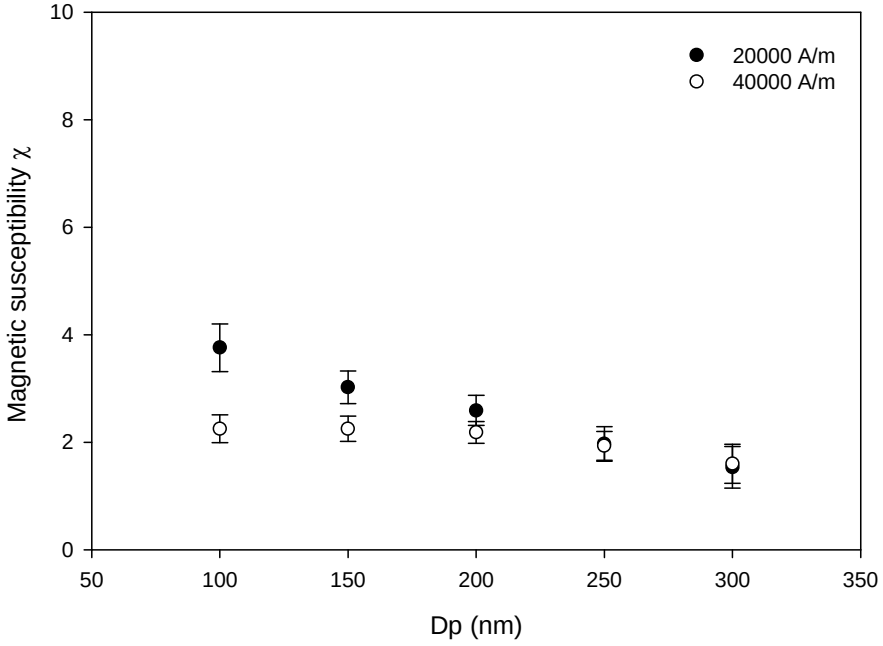

Figure 6.11 Derived magnetic susceptibility of γ-Fe_2O_3 particles in the size range from 100 to 300 nm at the estimated external magnetic fields of both 20 and 40 kA/m

A gradual decrease of the magnetic susceptibility of studied γ-Fe_2O_3 particles with increasing particle size is also observed in Fig. 6.11, which shows that particle magnetic susceptibility has a minor dependence on size. But the variation of magnetic susceptibility for γ-Fe_2O_3 particles in general remains small in the studied size range.

6.5 Summary

A magnetic filter system has been constructed and its performance has been evaluated to measure particles' magnetic property by using monodisperse γ-Fe_2O_3 particles ranging in size from 100 to 300 nm. In the system, SS 430 screens were placed in the magnetic filter element and exposed to an external magnetic field generated by an electric coil. Under the exposure of an external magnetic field, mesh screens were then magnetized and the high magnetic field gradient created by magnetized wires facilitated the collection of magnetic particles when they were passed through the filter element. The particle concentrations at the upstream and the downstream of the magnetic filter element were measured by an UCPC. Particle penetration obtained in the experiment was found to be a function of particle size, particle magnetic property and wire magnetization in general. In this study, a numerical model was also developed via the finite element package COMSOL Multiphysics 3.5. In the modeling, a single mesh screen is represented by an assembly of unit cells. The model then solved the flow, the magnetic fields, and the particle trajectory in a representative unit cell. The relationship between the particle penetration and the magnetic property for a given particle size, aerosol flow rate, and external magnetic field was obtained by the model. The numerical model was validated by comparing the calculated penetration with the experimental data, the former

being calculated with the measured magnetic susceptibility of 100, 150 and 250 nm γ-Fe_2O_3 particles via VSM. The magnetic susceptibilities of other sizes from 100 to 300 nm were also obtained by this model, according to the measured penetration data. In general, the magnetic susceptibility of γ-Fe_2O_3 particles is in the same order of magnitude. We observed that particle magnetic susceptibility has a minor dependence on the particle size and applied external magnetic field strength.

Chapter 7

Magnetic Susceptibility Characterization of Lunar Dust Simulants

7.1 Introduction

NASA's present plans for space exploration include returning human beings to the Moon, then to Mars and beyond. Many problems faced by the original Apollo astronauts must be addressed to enable missions of extended complexity and duration. One of the most significant ones encountered is the control of the lunar dust (< 20 μm) that makes up a large portion of the lunar surface (~ 20 weight %). During the Apollo missions, the ubiquitous, clinging, sharp, abrasive, glassy dust caused serious problems for exploration activities. The complications arising from the presence of lunar dust can be sorted into nine categories: vision obscuration, false instrument readings, dust coating and contamination, loss of traction, clogging of mechanisms, abrasion, thermal control problems, seal failures, and inhalation and irritation. Although simple dust mitigation measures were adequate for some problems (e.g., loss of traction), these measures were ineffective against many more serious problems (e.g., clogging, abrasion, and diminished heat rejection by radiators) (Gaier, 2005).

Lunar dust adhered to spacesuits both mechanically and electrostatically. Mechanical adhesion was affected by the barbed shapes of the dust grains, making removal difficult once the dust had worked into the fabric. Electrostatic adhesion was promoted by charging due to solar wind plasma, photoionization and triboelectric effects. During the Apollo missions, it was observed that the abrasivity of adhered dust caused significant wear on spacesuit fabrics, drastically reducing their useful lifetime (Subbs et al., 2007). Problems were also experienced during excursions of the Lunar Rover, with considerable quantities of dust being kicked up, covering exposed areas, and leading to increased friction at mechanical surfaces.

The majority of lunar dust (60-80%) is composed of broken pieces of agglutinitic glass, which contains abundant nanometer-sized metallic Fe grains (np-Fe^0) that impart a distinct magnetic susceptibility to the lunar soil. Recent experimentation with the 10~20 μm fraction of mature hi-Ti mare soil, 79221, has shown that a hand magnet will easily attract practically all the grains, even for those that are plagioclase with a thin patina of np-Fe^0 (Taylor et al., 2005). Motivated by such results, Kawamoto (2005) developed a cleaning device using magnetic force to remove lunar dust adhered to astronaut spacesuits. The total cleaning rate reported by the author was 40%. The possibility of improving the performance of magnetic mitigation methods requires a more complete understanding of the magnetic properties of the dust particles themselves.

Before proceeding to the measurement of relatively scarce Apollo lunar dust samples, the magnetic property of lunar dust simulants were characterized using the magnetic filter system described above. Simulants are often named after the places where they were developed (e.g., JSC from Johnson Space Center), and/or by the type of geologic feature that they are designed to reproduce (e.g., NU-LHT simulant was created by NASA and the USGS, and is a Lunar Highlands Type regolith simulant). Further designation by the maximum particle size may also be used (e.g., D = dust, F = fine, M = medium, and C = coarse). These designations are often accompanied by a number indicating the version of the simulant. The JSC-1A simulant manufactured by ORBITEC was intended to replicate many properties of low-titanium lunar mare regolith, matching the composition of the Apollo 14 regolith sample 14163 (which is a mixture between highlands and mare compositions). The NU-LHT series of highland regolith simulants models the normative mineralogy of Apollo 16 regolith (Edmunson et al., 2010).

In this study eight samples (three JSA-1A series, two NU-LHT series, and three minerals which are the building-block materials for the NU-LHT series) in the size range from 150 to 450 nm were characterized by the magnetic filter system in Chapter 6. The magnetic susceptibilities were obtained from the penetration difference with and without the external magnetic field, using the correlation calculated by the verified model. In this article, we report the measured magnetic susceptibility of lunar dust simulants in this test size range.

7.2 Experimental Setup and Procedure

The experimental setup was the same as Fig. 6.2. Lunar dust simulants were aerosolized using a custom Collision atomizer (Liu and Pui, 1974). A differential mobility analyzer (DMA, TSI Model 3081) downstream from the aerosol generation system classified singly charged, monodisperse particles in the size range from 150 to 450 nm. In principle, a DMA classifies particles of the desired size based on their electrical mobilities (Knutson and Whitby, 1975). For particles with diameters below 300 nm, the DMA was operated at an aerosol flow rate of 1.5 lpm and a sheath flow rate of 10.0 lpm. For particles larger than 300 nm, the DMA was operated at a sheath flow rate of 6.0 lpm while maintaining the same aerosol flow rate of 1.5 lpm. Since the classified particles exiting the DMA were electrically charged, a Po^{210} neutralizer and an electrostatic condenser were used downstream to obtain electrically neutral test particles of the desired size. The total flow rate through the magnetic filter was controlled by an UCPC operated at a flow rate of 0.3 lpm. The particle number concentrations both upstream and downstream of the magnetic filter system, i.e., N_{up} and N_{dn}, were measured

by the UCPC, respectively. The particle penetration P was then derived by the ratio of N_{dn} and N_{up}:

$$Penetration = \frac{N_{dn}}{N_{up}}. \tag{7-1}$$

7.3 Results and Discussion

Fig. 7.1 shows the SEM pictures of two lunar dust stimulants (JSC-1Af and NU-LHT-1D) and three minerals with the diameters of 200 and 400 nm. Generally, the shapes of two lunar dust stimulants and three minerals are nearly spherical, especially at the smaller size.

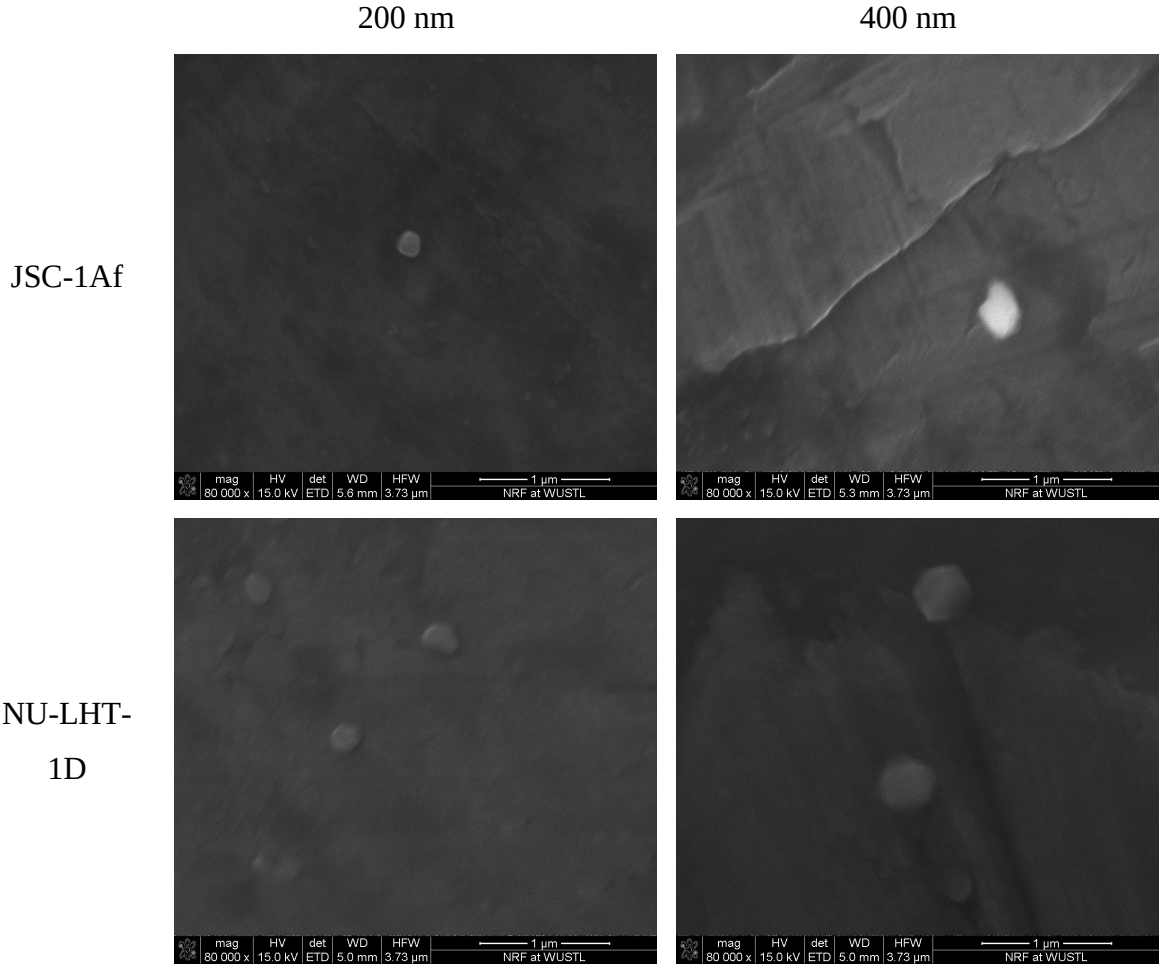

Norite

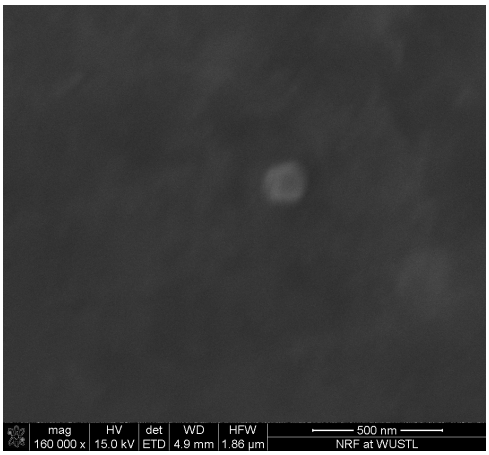

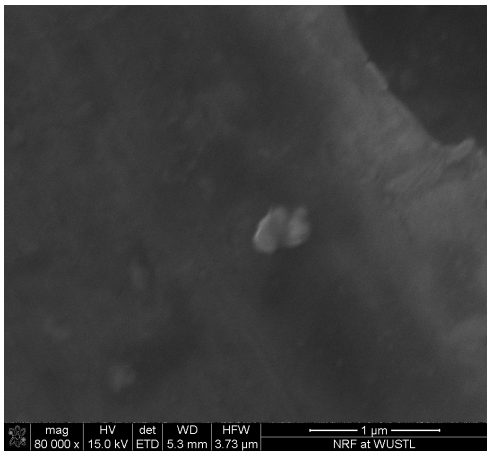

Anorthosite

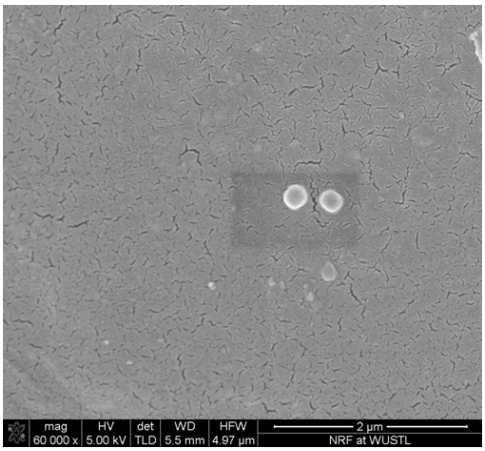

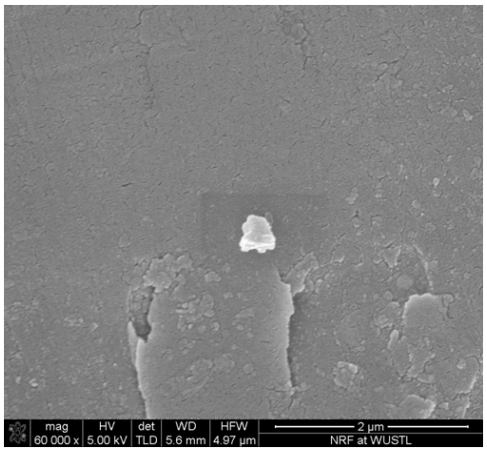

Harzburgite

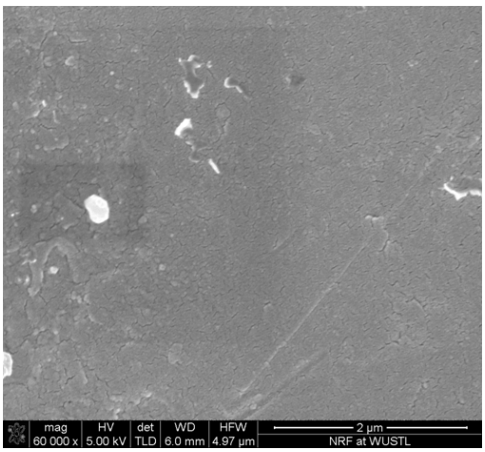

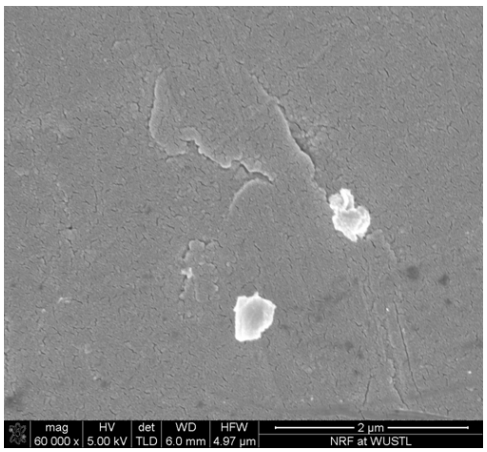

Figure 7.1 SEM pictures of two lunar dust stimulants and three minerals

As found in the results and discussion section of chapter 6, the magnetic susceptibility of particles can be directly obtained from the measured penetration data when a specific external magnetic field is applied. However, the magnetic susceptibilities

of the samples tested here are observed to be generally very low, resulting in a small absolute number of trapped particles under the presence of the applied magnetic field. For this reason we did not use the same direct approach, but instead used the penetration difference with and without the applied field to derive the magnetic susceptibility values of DMA-classified lunar dust particles.

Table 7.1 shows the magnetic susceptibility values of DMA-classified lunar dust simulants at the estimated 56 kA/m external magnetic field. In general terms, the measured magnetic susceptibilities are on the order of 10^{-3}~10^{-4}. Further, in the studied size range the bigger the particle, the smaller the magnetic susceptibility. The magnetic susceptibilities of the JSC-1A series are higher than those of the NU-LHT series and of the minerals, likely due to the composition differences. The JSC-1A #1 and #6 simulants were produced using a two-step process. The first step was to create a mature lunar regolith simulant that contains a high proportion of agglutinate-like particles and glass spherules, both of which contain metallic iron globules (including nanophase Fe^0). The second step was an industrial milling process to grind the feedstock material to the appropriate PSD (Gustafson et al., 2009). The LHT-1M series are completely composed of rock materials from the Stillwater Complex, which is a mafic layered intrusion consisting of hartzburgite, orthopyroxenite, norite, gabbro-norite, gabbro, and anorthosite. Ilmenite, obtained courtesy of Iluka Resources, is added. A high temperature, remotely coupled plasma melter was used to generate both high quality and agglutinitic glasses that simulate the glassy components of the regolith (Stoeser et al., 2007; 2008). According to the characterization and simulation profiles (JSC-1AF Characterization, LHT-1M Certificate of Information, available from the In Situ Resource Utilization

(ISRU) at NASA http://isru.msfc.nasa.gov; Schrader et. al., 2008), the JSC-1Af simulants have more Fe (FeO) component than the NU-LHT series, which do not include nanophase-Fe^0. This may represent the principal factor causing the magnetic susceptibilities of the JSC-1A series to be generally larger than those of the NU-LHT series.

Table 7.1 Magnetic susceptibility of lunar dust simulants

Dp (nm)	JSC-1A #6	Standard deviation	JSC-1A #1	Standard deviation	JSC-1Af	Standard deviation
150	$1.57*10^{-3}$	$1.0*10^{-4}$	$1.13*10^{-3}$	$7.0*10^{-5}$	$1.63*10^{-3}$	$7.0*10^{-5}$
200	$1.77*10^{-3}$	$1.0*10^{-4}$	$1.35*10^{-3}$	$9.0*10^{-5}$	$1.88*10^{-3}$	$1.2*10^{-4}$
250	$1.67*10^{-3}$	$1.0*10^{-4}$	$1.69*10^{-3}$	$1.4*10^{-4}$	$1.38*10^{-3}$	$7.0*10^{-5}$
300	$1.08*10^{-3}$	$8.0*10^{-5}$	$1.62*10^{-3}$	$1.7*10^{-4}$	$1.15*10^{-3}$	$8.0*10^{-5}$
350	$7.50*10^{-4}$	$5.0*10^{-5}$	$7.80*10^{-4}$	$5.0*10^{-5}$	$8.50*10^{-4}$	$5.0*10^{-5}$
400	$5.40*10^{-4}$	$7.0*10^{-5}$	$9.60*10^{-4}$	$9.0*10^{-5}$	$1.11*10^{-3}$	$1.0*10^{-4}$
450	$8.00*10^{-4}$	$9.0*10^{-5}$	$8.30*10^{-4}$	$9.0*10^{-5}$	$8.70*10^{-4}$	$5.0*10^{-5}$

Dp (nm)	NU-LHT 700-1x #8	Standard deviation	NU-LHT-1D	Standard deviation	Anorthosite	Standard deviation	Norite	Standard deviation	Harzburgite	Standard deviation
150	$8.80*10^{-4}$	$1.0*10^{-4}$	$6.30*10^{-4}$	$5.0*10^{-5}$	$<5*10^{-4}$		$5.60*10^{-4}$	$3.0*10^{-5}$	$<5*10^{-4}$	
200	$1.36*10^{-3}$	$1.3*10^{-4}$	$9.90*10^{-4}$	$7.0*10^{-5}$	$<2*10^{-4}$		$2.00*10^{-4}$	$2.0*10^{-5}$	$4.90*10^{-4}$	$6.0*10^{-5}$
250	$1.08*10^{-3}$	$9.0*10^{-5}$	$7.50*10^{-4}$	$6.0*10^{-5}$	$3.70*10^{-4}$	$1.0*10^{-5}$	$4.20*10^{-4}$	$3.0*10^{-5}$	$6.60*10^{-4}$	$5.0*10^{-5}$
300	$6.60*10^{-4}$	$6.0*10^{-5}$	$7.70*10^{-4}$	$8.0*10^{-5}$	$2.90*10^{-4}$	$1.0*10^{-5}$	$3.70*10^{-4}$	$3.0*10^{-5}$	$2.60*10^{-4}$	$1.1*10^{-4}$
350	$5.50*10^{-4}$	$3.0*10^{-5}$	$4.80*10^{-4}$	$3.0*10^{-5}$	$<1*10^{-4}$		$2.00*10^{-4}$	$3.0*10^{-5}$	$1.50*10^{-4}$	$3.0*10^{-5}$
400	$4.10*10^{-4}$	$3.0*10^{-5}$	$4.40*10^{-4}$	$4.0*10^{-5}$	$1.60*10^{-4}$	$1.0*10^{-5}$	$<1*10^{-4}$		$1.60*10^{-4}$	$1.0*10^{-5}$
450	$3.90*10^{-4}$	$3.0*10^{-5}$	$7.50*10^{-4}$	$6.0*10^{-5}$	$2.70*10^{-4}$	$2.0*10^{-5}$	$<1*10^{-4}$		$<1*10^{-4}$	

7.4 Summary

In this investigation we characterized eight lunar simulant samples (three JSA-1A series, two NU-LHT series, and three minerals) in the size range from 150 to 450 nm via a magnetic filter system. The magnetic susceptibilities of DMA-classified lunar dust simulant particles were obtained from the difference in particle penetration through a screen filter with and without an external magnetic field using the correlation calculated in the previously developed model. In general, the values of magnetic susceptibilities of tested samples were all on the order of 10^{-3}~10^{-4}. The magnetic susceptibility values decreased with increasing particle diameter in the studied size range. Further, the magnetic susceptibilities of the JSC-1A series are higher than those of the NU-LHT series and the minerals, a result which is attributed to the composition difference between two simulant series.

Chapter 8

Dissertation Accomplishments and Recommendations for Future Work

8.1 Summary of Accomplishments

In this dissertation, two physical properties of particles were studied, electrical and magnetic. . For particle electrical property, a unipolar corona charger was designed and evaluated for particle charge conditioning; a UV charger was also constructed for fundamental investigation of the particle photocharging process. For particle magnetic property, a magnetic filter system has been constructed, and its performance has been investigated. The studies accomplished within this dissertation -- particle charge conditioning by a unipolar corona charger, fundamental investigation of particle photocharging, calibration and modeling of a magnetic filter, and magnetic susceptibility characterization of lunar dust simulants -- are summarized as follows.

8.1.1 Particle Charge Conditioning by a Unipolar Corona Charger

The performance of a prototype corona-based, unipolar aerosol charge conditioner has been experimentally investigated. The construction of the prototype consists of an outer metal case and a corona discharge tube module with one end capped with a metal screen. Ions produced by the corona discharge module are driven through the metal screen by a weak, biased electric field between the screen and conditioner case (i.e., ion-driving voltage). The ion concentration in the charging zone can thus be controlled by varying ion-driving electrical field strength. The particle charging zone in the prototype is defined as the space between the metal screen and the aerosol exit channel of the prototype case. The nearly longitudinal electrical field in the charging zone is established by the geometric arrangement of the outer case and aerosol exit tube (both of which are grounded, and the tube module with the ion-driving voltage). The design of the charging zone in the charger also enables the quick exit of particles once they are electrically

charged, thus reducing the loss of charged particles. No sheath air was used in this prototype. The aerosol is directed into the prototype by two inlets located at opposite positions, and then flows into the charging zone at a 45^{o} angle to the center axis. The flow design minimizes the potential contamination of the corona needle tip by particles, thus prolonging the needle's lifetime.

The performance of the prototype was optimized by varying operational parameters (i.e., aerosol flow rate, corona current, and ion-driving voltage) to achieve its maximum extrinsic charging efficiency. The optimization experiment was done with monodisperse Ag particles 10 nm in diameter. Based on our finding, the corona current had negligible effect on the charging performance of the prototype. The corona current of 2 μA was thus used in the rest of our study. Our study also found that operating the prototype at a 3 lpm aerosol flow and an ion-driving voltage of 600 V offers the maximum extrinsic charging efficiency.

Both intrinsic and extrinsic charging efficiencies of particles in diameters ranging from 5 to 50 nm were measured at the optimal operating conditions. This prototype provides higher extrinsic efficiency than other corona-based unipolar chargers for both positive and negative charging. Charge distributions of monodisperse particles downstream of the prototype, operating at a 3 lpm aerosol flow rate, a 2 μA corona current and various ion-driving voltages, were measured by the tandem-DMA technique. The experimental data of particle charging efficiencies and charge distributions agree reasonably with the calculated results. The charge distribution measurement confirmed that after passing through the prototype the charge distribution of particles is variable through the control of the charging ion concentration by changing the ion-driving

voltage. The birth-and-death charging model with the Fuchs limiting sphere theory was used to obtain the $N_i t$ values at different operation conditions via best fitting to the measured intrinsic charging efficiency. The same $N_i t$ values obtained were also used in the birth-and-death charging model to calculate the charge distribution of particles. Reasonable agreement was achieved when the calculated charge distributions of particles were compared with the extrinsic charge distributions measured. The result implies a reduced loss of charged particles in the prototype than existing unipolar chargers in which the aerosol flow direction is perpendicular to the electric field direction.

8.1.2 Investigation of Aerosol Charging Using Pen-type UV Lamps

Particle photocharging for particles of various materials (i.e., Ag, Fe_2O_3, Co_3O_4, ZnO and TiO_2) has been investigated through a simple UV charger with pen-type UV lamps. The studied UV charger consists of a quartz tube about 7 in. long as the aerosol irradiation zone, four low-pressure Hg lamps located around the quartz tube, and an outer cylindrical aluminum case with aerosol inlet at one end and outlet at the other end. The charger also has an ion trap section at the exit of the quartz tube to remove free ions.

We experimentally evaluated the performance of the UV charger operated at 5 lpm flow rate and with four UV lamps using monodisperse Ag with diameters from 7 to 30 nm and metal oxide particles with sizes ranging from 50 to 200 nm. We characterized both extrinsic and extrinsic charging efficiencies of the UV charger, and measured the charge distributions of particles passing through the UV charger using the electrostatic precipitation technique for particles of sizes larger than those studied in previous work. We also compared the performance of the UV charger to existing corona-based chargers. The studied UV charger provides higher extrinsic charging efficiencies than corona-based

unipolar chargers for Ag particles. The extrinsic charging efficiency of the prototype is higher than 80% for particles of diameters larger than 15 nm. Depending on the material of test particles, the charging efficiency of the UV charger varies much, showing significant material dependence for the photocharging. Charge distributions of monodisperse Ag and Fe_2O_3 particles at the exit of the UV charger, operating at a 5 lpm aerosol flow rate and with four UV lamps turned on, were measured by the electrostatic precipitation technique. The charge distribution of 25 nm Ag particles is similar to that of 100 nm Fe_2O_3 particles, which further concludes the material dependence of the photocharging process.

To evaluate the effect of irradiation intensity on particle photocharging, we measured the charging efficiencies and charge distributions for Ag particles with sizes from 7 to 30 nm at an aerosol flow rate of 5 lpm, with one, two, or four lamps turned on. This study used the UV charging model with the photoemission following the Fowler-Nordheim law to obtain the K_cI values at various operational conditions by best fitting to the measured intrinsic charging efficiency. The same K_cI values obtained above were then used in the charging model to calculate the charge distribution of particles. The study achieved reasonable agreement between calculated and measured charge distributions of particles.

8.1.3 Calibration and Modeling of a Magnetic Filter

A magnetic filter system has been constructed and its performance has been evaluated to measure particles' magnetic properties by using monodisperse γ-Fe_2O_3 particles ranging in size from 100 to 300 nm. In the system, SS 430 screens were placed in the magnetic filter element and exposed to an external magnetic field generated by an

electric coil. Under the exposure of an external magnetic field, mesh screens were then magnetized and the high magnetic field gradient created by magnetized wires facilitated the collection of magnetic particles when they were passed through the filter element. The particle concentrations upstream and downstream of the magnetic filter element were measured by an UCPC. Particle penetration obtained in the experiment was found to be a function of particle size, particle magnetic property and wire magnetization in general. In this study, a numerical model was also developed via the finite element package COMSOL Multiphysics 3.5. In the modeling, a single mesh screen is represented by an assembly of unit cells. The model then solved the flow and magnetic fields, and the particle trajectory in a representative unit cell. The relationship between the particle penetration and the magnetic property for a given particle size, aerosol flow rate, and external magnetic field were obtained by the model. The numerical model was validated by comparing the calculated penetration with the experimental data, the former being calculated with the measured magnetic susceptibility of 100, 150, and 250 nm γ-Fe_2O_3 particles via VSM. The magnetic susceptibilities of other sizes from 100 to 300 nm were also obtained by this model, according to the measured penetration data. In general, the magnetic susceptibility of γ-Fe_2O_3 particles is in the same order of magnitude. We observed that particle magnetic susceptibility has a minor dependence on the particle size and applied external magnetic field strength.

8.1.4 Magnetic Susceptibility Characterization of Lunar Dust Simulants

In this investigation we characterized eight lunar simulant samples (three JSA-1A series, two NU-LHT series, and three minerals) in the size range from 150 to 450 nm via a magnetic filter system. The magnetic susceptibilities of DMA-classified lunar dust

simulant particles were obtained from the difference in particle penetration through a screen filter with and without an external magnetic field using the correlation calculated in the previously developed model. In general, the values of magnetic susceptibilities of tested samples were all on the order of 10^{-3}~10^{-4}. The magnetic susceptibility values decreased with increasing particle diameter in the studied size range. Further, the magnetic susceptibilities of the JSC-1A series are higher than those of the NU-LHT series and the minerals, a result which is attributed to the composition difference between two simulant series.

8.2 Recommendations for Future Research

The unipolar charge conditioner developed in this study has the design of parallel directions of electrical and aerosol flow fields, variable control of ion concentration in the charging zone, and direct particle exit once the particles are electrically charged, thus reducing the loss of charged particles. However, it still has space to improve by optimizing the charger structure, such as the dimension of the charging zone and the angle of the aerosol stream into the charging zone. Since multiple charges of particles is always an issue in the data analysis when using a corona charger as a component of a particle sizer, the charge conditioner may be a good option in this area. It can provide high charging efficiency when measuring small particles, and reduce multiple charges for large particles by altering the ion-driving voltage. We use the birth-and-death charging model with the Fuchs limiting sphere theory to obtain the $N_i t$ values and calculate the charging efficiency and charge distribution. The discrepancy between the experimental data and modeling results can be attributed to the loss of charged particles and the non-

uniform ion concentration in the charging zone. Hence, detailed simulation on the charging process is needed to consider these two factors.

Although metal and metal oxide particles have been investigated, for the fundamental study of aerosol photocharging, other particles, e.g., salt and organics, also should be tested to further explore material dependence. The effect of light intensity has been experimentally evaluated by varying the number of lamps and theoretically represented by the parameter I in the model. A light intensity meter is needed to measure the intensity value so that the K_c value can be further retrieved from the model and compared among different particles. In fact, researchers have proposed the theoretical models to calculate the K_c values among different elements. The differences between the modeling results and experiment data require further investigations on particle photocharging process in both theoretical and experimental ways. Moreover, other factors of aerosol photocharging, e.g., particle concentration and ion recombination, can be studied in the future.

For the magnetic filter, the lower detection limit of particle magnetic susceptibility was on the order of 10^{-4}, limited by the field strength that is presently available with this apparatus. For particles with magnetic susceptibility lower than 10^{-4}, the resultant magnetic force acting on particles while they pass through the screen filter is so small that it could not enhance the particle trapping in the filter element in addition to diffusion. The induced magnetic force is a function of the external magnetic field strength and magnetic field gradient. Thus the detection limit of the system can be further improved by optimizing the system operating parameters, such as applying a stronger

external magnetic field strength or using screens with stronger magnetic properties and/or with finer mesh.

References

[1] Adachi, M., Liu, B.Y.H., and Piu, D.Y.H. *Development of an Automatic System for Measuring Particle Charge and Size Distributions in a Clean Room.* Part. Part. Syst. Charact., 8: 200-208, 1991.

[2] Adachi, M., Kousaka Y., and Okuyama, K. *Unipolar and bipolar diffusion charging of ultrafine aerosol particles.* J. Aerosol Sci., 16(2): 109-122, 1985.

[3] Adachi, M., Okuyama, K., Kousaka, Y., Kozuru, H., and Pui, D.Y.H. *Bipolar diffusion charging of aerosol particles under high particle/ion concentration ratios.* Aerosol Sci. Technol., 11: 144-156, 1989.

[4] Adachi, M., Tsukui, S., and Okuyama, K. *Nanoparticle formation mechanism in CVD reactor with ionization of source vapor*. J. Nanoparticle Res., 5: 31-37, 2003.

[5] Aers, G.C., and Inglesfield, J.E. *Photoyield enhancement from small metal particles.* J. Phys. F: Met. Phys., 13(8): 1743-1756, 1983.

[6] Airapetyan, S.S., Balayan, G.G., and Khachatryan, A.G. *Synthesis and Some Characteristics of Magnetic Matrices for Fixation of Biologically Active Substances*. Russian J. Appl. Chem., 74(3): 519-521, 2001.

[7] Akoto, I.Y. *Mathematical Modeling of High-Gradient Magnetic Separation Device.* IEEE Trans. Magn., 13(5): 1486-1489, 1977.

[8] Anand, P., Etzel, J.E., and Friedlaender, F.J. *Heavy metals removal by high gradient magnetic separation*. IEEE Trans. Magn., 21(5): 2062-2064, 1985.

[9] Biskos, G., Reavell, K., and Collings, N. *Unipolar diffusion charging of aerosol particles in the transition regime*. J. Aerosol Sci., 36: 247-265, 2005.

[10] Boisdron, Y., and Brock, J.R. *On the stochastic nature of the acquisition of electrical charge and radioactivity by aerosol particles.* Atmospheric Environment, 4: 35-50, 1970.

[11] Brown, R.C. *Air Filtration*. Pergamon Press, London, 1993.

[12] Bucak, S., Jones, D.A., Laibinis, P.E., and Hatton, T.A. *Protein separations using colloidal magnetic nanoparticles*. Biotechnol. Prog., 19(2): 477-484, 2003.

[13] Burtscher, H., Scherrer, L., Siegmann, H.C., and Schmidt-Ott, A., and Federer, B. J. *Probing aerosol by photoelectric charging.* J. Appl. Phys., 53(5): 3787-3791, 1982.

[14] Buscher, P., Schmidt-Ott, A., and Wiedensohler, A. *Performance of a unipolar 'square wave' diffusion charger with variable nt-product.* J. Aerosol Sci., 25: 651-663, 1994.

[15] Chen, D.-R., and Pui, D.Y.H. *A high efficiency, high throughput unipolar aerosol charger for nanoparticles.* J. Nanoparticle Res., 1: 115-126. 1999.

[16] Chen, D.-R., Pui, D.Y.H., Hummes, D., Fissan, H., Quant, F.R., and Sem, G.J. *Design and evaluation of a nanometer aerosol differential mobility analyzer (Nano-DMA).* J. Aerosol Sci., 29: 497-509, 1998.

[17] Chen, H., Ebner, A.D., Bockenfeld, D., Ritter, J.A., Kaminski, M.D., Liu, X., Rempfer, D., and Rosengart, A.J. *A comprehensive in vitro investigation of a portable magnetic separator device for human blood detoxification*. Phys. Med. Biol., 52: 6053-6072, 2007a.

[18] Chen, H., Bockenfeld, D., Rempfer, D., Kaminski, M.D., and Rosengart, A.J. *Three-Dimensional modeling of a portable medical device for magnetic separation of particles from biological fluids*. Phys. Med. Biol., 52: 5205-5218, 2007b

[19] Chen, Q.Y., and Bates, C.W. *Geometrical factors in enhanced photoyield from small metal particles.* Phys. Rev. Lett., 57(21): 2737-2740, 1986.

[20] Cheng, Y.S., and Yeh, H.C. *Theory of a screen-type diffusion battery*. J. Aerosol Sci., 11: 313-320, 1980.

[21] Cheng Y.S., Yeh H.C., and Kanapilly G.M. *Collection efficiencies of a point-to-plane electrostatic precipitator.* American Industrial Hygiene Association, 42: 605-610, 1981.

[22] Clacke, J. *SQUIDs*. Scientific American, August: 46-53, 1994.

[23] Clarkson, C., Kelland, D., and King, T. *Model for calculation of capture radii of a high gradient magnetic separator at moderate Reynolds numbers.* IEEE Trans. Magn., 12(6): 901-903, 1976.

[24] Cohen, B.S., Xiong, J.Q., and Li, W. *The influence of charge on the deposition behavior of aerosol particles with emphasis on single charged nanometer sized particles,* in aerosol inhalation, lung transport & deposition & the relation to the environment. Recent Research & Frontiers, ed. By Marijnissen, J.C.M., and Gradon, L., Kluwer Scientific Press, Norwell, MA, 153-164, 1996.

[25] Cohen, B.S., Xiong, J.Q., Fang, C.-P., and Li, W. *Deposition of charged particles on lung airways.* Health Phys., 74: 554-560, 1998.

[26] Cowen, C., and Friedlaender, F.J. *Single Wire Model of High Gradient Magnetic Separation Processes III*. IEEE Trans. Magn., 13(5): 1483-1485, 1977.

[27] Cowen, C., Friedlaender, F.J. and Jaluria, R. *Single Wire Model of High Gradient Magnetic Separation Processes I.* IEEE Trans. Magn., 12(5): 466-470, 1976.

[28] Czichos, H., Saito, T., Smith, L. *Handbook of Materials Measurement Methods.* Springer, Berlin, 2006

[29] DOE Industrial Technologies Program (ITP) Report, Materials for Separation Technologies: Energy and Emission Reduction Opportunities, BSC Inc., and Oak Ridge National Laboratory (ORNL), 2005 (http://www1.eere.energy.gov/industry/imf/pdfs/separationsreport.pdf).

[30] Ebner, A.D., and Ritter, J.A. *New correlation for the capture cross section in high-gradient magnetic separation*. AIChE Journal, 47(2): 303-313, 2001.

[31] Edmunson, J., Betts, W., Rickman, D., McLemore, C., Fikes, J., Stoeser, D., Wilson, S., and Schrader, C. *NASA lunar regolith stimulant program.* 41st Lunar and Planetary Science Conference, Woodlands, Texas, 2010.

[32] Einstein, A. *Investigations on the theory of the Brownian movement* (R. Furth, ed.). Dover, New York, 1956.

[33] Faraci, G., Pennisi, A.R., and Margaritondo, G. *Mechanism of phtotelectron yield enhancement from Ag clusters.* Phys. Rev. B, 40(6): 4209-4211, 1989.

[34] Faraci, G., Pennisi, A.R., Privitera, V., Burtscher, H., and Schnidt-Ott, A. *Photoemission from small particles of Ag and Au.* Phys. Rev. B, 37(18): 542-546, 1988.

[35] Fissan, H., Kennedy, M.K., Krinke, T.J., and Kruis, F.E. *Nanoparticles from the Gas Phase as Building Blocks for Electrical Devices.* J. Nanoparticle Res., 5: 299-310, 2003.

[36] Foner, S. *Versatile and sensitive vibrating-sample magnetometer.* The Review of Scientific Instruments, 30(7): 548-557, 1995.

[37] Forsyth, B., Liu, B.Y.H., and Romay, F.J. *Particle Charge Distribution Measurement for Commonly Generated Laboratory Aerosols.* Aerosol Sci. Technol., 8(6): 489-501, 1998.

[38] Fowler, R. H. *The Analysis of Photoelectric Sensitivity Curves for Clean Metals at Various Temperatures.* Phys. Rev. 38: 45-56, 1931.

[39] Friedlander, S.K. *Smoke, Dust, and Haze.* Oxford University Press, New York, 2000.

[40] Friedlander, S.K., and Pui, D.Y.H. *Emerging issues in nanoparticle aerosol science and technology (NAST).* NSF workshop report, 2003.

[41] Fuchs, N.A. *On the stationary charge distribution on aerosol particles in bipolar ionic atmosphere.* Geofis. Pura Appl., 56: 185-193, 1963.

[42] Gaier, J.R. *The effects of lunar dust on EVA systems during the Apollo missions, NASA/TM— 2005-213610.* Glenn Research Center, Cleveland, Ohio, 2005.

[43] Gerber, R. *Magnetic Separation*. In Applied Magnetism, Gerber, R., Wright, C.D., and Asti, G., eds., Kluwer, Dordrecht, the Netherlands, 1994.

[44] Gerber, R., and Birss, R.R. *High Gradient Magnetic Separation.* Wiley, New York, 1983.

[45] Gerber, R., and Lawson, P. *The HGMS Filter Performance Exponential Law*. IEEE Trans. Magn., 25(5): 3806-3808, 1989.

[46] Gustafson, R.J., and White, B.C. *Development of a lunar dust simulant, International Conference On Environmental Systems.* Savannah, Georgia, 2009.

[47] Haefeli, U.O., Casillas, S., Dietz, D.W., Pauer, G.J., Rybicki, L.A., Conzone, S.D., and Day, D.E. *Hepatic tumor radioembolization in a rat model using radioactive rhenium(^{186}Re/^{188}Re) glass microspheres*. Int. J. Radiation Oncology and Biological Phy., 44(1): 189-199, 1999.

[48] Han, B., Shimada, M., Choi, M., and Okuyama K. *Unipolar Charging of Nanosized Aerosol Particles Using Soft X-ray Photoionization.* Aerosol Sci. Technol., 37(4): 330-341, 2003.

[49] Hinds, W.C. *Aerosol Technology*. John Wiley & Sons, New York, 1999.

[50] Hogan, C.J., Li, L., Biswas, P., and Chen, D.-R. *Estimating Aerosol Particle Charging Parameters Using a Bayesian Inversion Technique.* J. Aerosol Sci. 40: 295-306, 2009.

[51] Hontañón, E., and Kruis, F. *Single charging of nanoparticles by UV photoionization at high flow rates*. Aerosol Sci. Technol., 42(4): 310-323, 2008.

[52] Jacobs, H.O., and Whitesides, G.M. *Submicrometer patterning of charge in thin-film electrets*, Science, 291: 1763–1766, 2001.

[53] Jiang J., Chen, D.-R., and Biswas, P. *Synthesis of nanoparticles in a flame aerosol reactor with independent and strict control of their size, crystal phase and morphology*. Nanotechnology, 18: 285603, 2007a.

[54] Jiang, J., Lee, M.H., and Biswas, P. *Model for nanoparticle charging by diffusion, direct photoionization, and thermionization mechanisms*. J. Electrostatics, 65(4): 209-220, 2007b.

[55] Jung, Th., Burtscher, H., and Schmidt-Ott, A. *Multiple charging of ultrafine aerosol particles by aerosol photoemission (APE)*. J. Aerosol Sci., 19(4): 485-490, 1988.

[56] Karapinar, N. *Magnetic separation of ferrihydrite from wastewater by magnetic seeding and high-gradient magnetic separation*. Int. J. Miner. Process., 71: 45-54, 2003

[57] Kauffeldt, Th., Lohmann, M., and Schmidt-Ott, A. *On-line measurement of magentic properties of aerosol particles*. Procedding of the Workshop Ultrafine Paticles in Delft 1993 (edited by MarijnissenJ. and Partsinis S.E.), Delft University Press, 1993.

[58] Kauffeldt, Th., Lakner, H., Luczak, A., and Schmidt-Ott, A. *The influence of a magnetic field in magnetic particle production*. J. Aerosol Sci., 26: S231-S232, 1995.

[59] Kauffeldt, Th., Kleinwechter, H., and Schmidt-Ott, A. *Absolute on-line measurement of the magnetic moment of aerosol particles*. Chem. Eng. Commun., 151: 169-185, 1996.

[60] Kauffeldt, Th., Luczak, A., and Schmidt-Ott, A. *On line investigation of the relation between magentic properties of nickel particles on primary particle size*. J. Aerosol Sci., 28: S315-S316, 1997.

[61] Kaufman, S. L., Medved, A., Pcher, A., Hill, N., Caldow, R., and Quant, F.R. *An Electrical Aerosol Detector Based on the Corona-Jet Charger*. Abstracts of the 21st annual AAAR Conference Charlotte, 2002.

[62] Kawamoto, H. *Electrostatic and electromagnetic cleaning of lunar dust adhered to spacesuits.* Annual Meeting of the Lunar Exploration Analysis Group, Houston, Texas, 2009.

[63] Kennard, E. H. *Kinetic theory of gasses*. McGraw-Hill, New York, 1938.

[64] Keskinen, J., Pietarinen, K., and Lehtimäki, M. *Electrical Low Pressure Impactor*. J. Aerosol Sci., 23: 353-360, 1992.

[65] Kim, H., Kim, J., Yang, H., Suh, J., Kim, T., Han, B., Kim, S., Kim, D.S., Pikhitsa, P.V., and Choi, M. *Parallel patterning of nanoparticles via electrodynamic focusing of charged aerosols. Nature Nanotechnology*, 1: 117-121, 2006.

[66] Knutson, E.O., and Whitby, K.T. *Aerosol Classification by Electric Mobility, Apparatus, Theory, & Applications*. J. Aerosol Sci., 6: 443-421, 1975.

[67] Kobe, S., Drazic, G., McGuiness, P.J., and Strazisar, J. *The influence of the magnetic field on the crystallisation form of calcium carbonate and the testing of a magnetic water-treatment device*. J Magn. Magn. Mater., 236: 71-76, 2001.

[68] Kogelschatz, U. *Silent-discharge driven excimer UV sources and their applications*. Appl. Surface Sci., 54: 410-423, 1992.

[69] Kruis, F.E., and Fissan, H. *Nanoparticle charging in a twin Hewitt charger*. J. Nanoparticle Res., 3: 39-50, 2001.

[70] Kulkarni, P., Namiki, N., Otani Y., and Biswas P. *Charging of particles in unipolar coronas irradiated by in-situ soft X-rays: enhancement of capture efficiency of ultrafine particles*. J. Aerosol Sci., 33: 1279-1296, 2002.

[71] Laschober, C., Kaufman, S.L., Reischl, G., Allmaier, G., and Szymanski, W.W. *Comparison between an Unipolar Corona Charger and a Polonium-based Bipolar Neutralizer for the Analysis of Nanosized Particles & Biopolymers*. J. Nanoscience & Nanotechnology, 6:1474-1481, 2006.

[72] Legault, A., and Rivero, R. *Mainstreaming Efficient Industrial Separation Systems.* OPEN Energy Technology Bulletin, 55, 2008 (http://www.iea.org/impagr/cip/pdf/Issue55IETSArticle.pdf).

[73] Liu, B.Y.H., and Piu, D.Y.H. *A Submicrion Aerosol Standard and the Primary, Absolute Calibration of the Condensation Nuclei Counter*. J. Colloid and Interface Sci., 47(1): 155-171, 1974a.

[74] Liu, B.Y.H., and Pui, D.Y.H. *Equilibrium bipolar charge distribution of aerosols.* J. Colloid and Interface Sci., 49(2): 305-312, 1974b.

[75] Liu, B.Y.H., and Pui, D.Y.H. *On unipolar diffusion charging of aerosols in the continuum regime*. J. Colloid and Interface Sci., 58(1): 142-149, 1977.

[76] Lu., S., Pugh, R.J., Forssberg, E. *Interfacial Separation of Particles*. Oxford: Elsevier, Amsterdan, The Neherlands, 2005

[77] Luborsky, F.E., and Drummond, B.J. *High Gradient Magnetic Separation: Theory versus Experiment*. IEEE Trans. Magn., 11(6): 1696-1700, 1975.

[78] Maisels, A., Jordan, F., and Fissan, H. *Dynamics of the aerosol particle photocharging process*. J. Appl. Phy., 91(5): 3377-3383, 2002.

[79] Maisels, A., Jordan, F., and Fissan, H. *On the effect of charge recombination on the aerosol charge distribution in photocharging systems*. J. Aerosol Sci., 34: 117-132, 2003.

[80] Marquard, A., Meyer, J., and Kasper, G. *Characterization of unipolar electrical aerosol chargers — Part I: A review of charger performance criteria*. J. Aerosol Sci., 37: 1052-1068, 2006a.

[81] Marquard, A., Meyer, J., and Kasper, G. *Characterization of unipolar electrical aerosol chargers — Part II: Application of comparison criteria to various types of nanoaerosol charging devices*. J. Aerosol Sci., 37: 1069-1080, 2006b.

[82] Matter, D., Mohr, M., Fendel, W., Schmidt-Ott, A., and Burtscher H. *Multiple wavelength aerosol photoemission by excimer lamps*. J. Aerosol Sci., 26(7): 1101-1115, 1995.

[83] Mazumder, M.K., Robison, J., Wyatt, C., Srirama, P.K., Sharma, R., Zhang, J., and Biris, A.S. *Electrohydrodynamic dispersion of dry fine powders*. IEEE-IAS Annual Meeting New Orleans, September, 2007.

[84] Medved, A., Dorman, F., Kaufman, S.L., and Pocher, A. *A new corona-based charger for aerosol particles*. J. Aerosol Sci. 31: S616-S617, 2000.

[85] Melandri, C., Tarroni, G., Prodi, V., De Zaiacomo, T., Formignani, M., and Lombardi, C.C. *Deposition of charged particles in the human airways*. J. Aerosol Sci., 14: 657-569, 1983.

[86] Miltenyi, S., Müller, W., Weichel, W., and Radbruch, A. *High-gradient magnetic cell-separation with Macs*. Cytometry, 11(2): 231-2388, 1990.

[87] Mohr, M., and Burtscher, H. *Photoelectric aerosol charging at high particle concentrations.* J. Aerosol Sci., 28(4): 613-621, 1997.

[88] Moeser, G., Roach, K.A., Green, W.H., Laibinis, P.E., and Hatton, T.A. *Water-Based Magnetic Fluids as Extractants for Synthetic Organic Compounds*. Ind. Eng. Chem. Res., 414(19): 4739-4749, 2002.

[89] Mohr, M., Matter, D., and Burtscher, H. *Efficient multiple charging of diesel particles by photoemission.* Aerosol Sci. Technol., 24(1): 14-20, 1996.

[90] Müller, U., Schmidt-Ott, A., and Burtscher, H. *Photoelectric Quantum Yield of Free Silver Particles near Threshold*. Z. Physics B—Condensed Matter. 73: 103-106, 1988a.

[91] Müller, U., Burtscher, H., and Schmidt-Ott, A. Photoemission from small metal spheres: A model calculation using an enhanced three-step model. Phys. Rev. B, 38(11): 7814-7816, 1988b.

[92] Natanson, G.L. *On the theory of the charging of a microscopic aerosol particles as a result of capture of gas ions*. Soviet Phy. Technical Phy., 5: 538-551, 1960.

[93] Nedelcu, S., and Watson, J.H.P. *Magnetic separator with transversally magnetised disk permanent magnets*. Miner. Eng., 15: 355-359, 2002.

[94] Newns, A., and Pascoe, R.D. *Influence of path length and slurry velocity on the removal of iron from kaolin using a high gradient magnetic separator*. Miner. Eng., 15: 465-467, 2002.

[95] Noronha, F.B., Schmal, M., Nicot, C., Moraweck, B., and Frety, R. *Characterization of Graphite-Supported Palladium-Cobalt Catalysts by*

Temperature-Programmed Reduction and Magnetic Measurements. J. Cataly., 168(1): 42-50, 1997.

[96] O'Handley R.C. *Modern Magnetic Materials: Principles and Applications*. John Wiley, New Yourk, 2000.

[97] Park, J.W., Yoo, I.S., Chang, W.S., Lee, E.C., Ju, H., Chung, B. H., and Kim, B.S. *Magnetic moment measurement of magnetic nanoparticles using atomic force microscopy*. Measurement Sci. Tech., 19: 017005, 2008.

[98] Parker, K.R. *Applied electrostatic precipitation*. Blackie Academic and Professional, London, 1997.

[99] Penn, D.R., and Rendell, R.W. *Surface photoeffect in small spheres.* Phys. Rev. B, 26(6): 3047-3067, 1982.

[100] Prinz G.A. *Magnetoelectronics*. Science, 282: 1660-1663, 1998.

[101] Pui, D.Y.H., Fruin S., and McMurry P.H. *Unipolar diffusion charging of ultrafine aerosols*. Aerosol Sci. Technol., 8: 173-187, 1988.

[102] Qi, C., Chen, D.-R., and Pui, D.Y.H. *Experimental study of a new corona-based unipolar aerosol charger*. J. Aerosol Sci., 38(7): 775-792, 2007.

[103] Qi, C., Chen, D.-R., and Greenberg, P. *Performance study of a unipolar aerosol mini-charger for a personal nanoparticle sizer*. J. Aerosol Sci., 39(5): 450-459, 2008.

[104] Qi, C., Asbach, C., Shin, W.G., Fissan, H., and Pui, D.Y.H. *The effect of particle pre-existing charge on unipolar charging and its implication on electrical aerosol measurements*. Aerosol Sci. Technol., 43: 232-240, 2009.

[105] Ramachandran, G., and Kandlikar, M. *Bayesian Analysis for Inversion of Aerosol Size Distribution Data*. J. Aerosol Sci., 27: 1099-1112, 1996.

[106] Reischl, G.P., Makela, J.M., Harch, R., and Necid, J. *Bipolar charging of Ultrafine Particles in the size range below 10 nm.* J. Aerosol Sci., 27: 931-949, 1996.

[107] Rembaum, A., Yen, R.C.K., Kempner, D.H., and Ugelstad, J., *Cell labeling and magnetic separation by means of immunoreagents based on polyacrolein microspheres*. J. Immunol. Methods, 52(3): 341-351, 1982.

[108] Romay, F.J., and Pui, D.Y.H. *On the combination coefficient of positive ions with ultrafine neutral particles in the transition and free-molecule regime.* Aerosol Sci. Technol., 17: 134-147, 1992.

[109] Romay, F.J., Liu, B.Y.H., and Pui, D.Y.H. *A sonic jet corona ionizer for electrostatic discharge and aerosol neutralization.* Aerosol Sci. Technol., 20: 31-41, 1994.

[110] Rousseau, R.W. *Handbook of Separation Process Technology*. Wiley, New York, 1987.

[111] Roy, S., Das, D., Chakravorty, D., and Agrawal, D.C. *Magnetic properties of glass-metal nanocomposites prepared by the sol-gel route and hot pressing*. J. Appl. Phys. 74: 4746-4749, 1993.

[112] Scheibel, H.G., and Porstendörfer, J. *Generation of monodisperse Ag- and NaCl-aerosol with particle diameters between 2 and 300 nm*. J. Aerosol Sci., 14: 113-126, 1983.

[113] Schleicher, B., Burtscher, H., and Siegmann, H. C. *Photoelectric Quantum Yield of Nanometer Metal Particles*. Appl. Phys. Lett. 63: 1191-1193, 1993.

[114] Schmidt-Ott, A., Schurtenberger, P., and Siegmann, H.C. *Enormous Yield of Photoelectrons from Small Particles*. Phys. Rev. Lett. 45: 1284-1287, 1980.

[115] Schmidt-Ott, A., and Siegmann, H.C. *Photoelectron emission from small particles suspended in air.* Appl. Phys. Lett., 32(11): 710-713, 1978.

[116] Shimada, M., Cho, S. –J., Okuyama, K., Tamura, T., Adachi, M., and Fujii, T. *Removal of Airborne Particles by a Tubular Particle Removal Device Using UV/photoelectron Method.* J. Aerosol Sci., 28(4): 649-661, 1997.

[117] Schrader, C.S., Rickman, R., Mclemore, C., Fikes, J., Wilson, S., Stoeser, D., Butcher, A., and Botha, P. *Extant and extinct lunar regolith simulants: modal analyses of NU-LHT-1M and -2M, OB-1, JSC-1, JSC-1A and -1AF, FJS-1, and MLS-1*. Planetary Mining and Science Symposium, Montreal, Canada, 2008.

[118] Shaikh, A.M.H., and Dixit, S.G. *Removal of phosphate from waters by precipitation and high gradient magnetic separation*. Water Res., 26(6):845-852, 1992.

[119] Shimada, M., Han, B., Okuyama, K., and Otani, Y. *Bipolar Charging of Aerosol Nanoparticles by a Soft X-ray Photoionizer.* J. Chem. Eng. Jpn. 35: 786-793, 2002.

[120] Shin W.G., Pui D.Y.H., Fissan H., Neumann S., and Trampe A. *Calibration & numerical simulation of Nanoparticle Surface Area Monitor (TSI Model 3550 NSAM)*. J. Nanoparticle Res., 9: 61-69, 2007.

[121] Stoeser D., and Wilson, S. *NU-LHT-1M pilot highlands soil stimulant*. Lunar and Dust Regolith Simulant Workshop, Huntsville, Alabama, 2007.

[122] Stoeser, D., Wilson, S., Weinstein, M., Rickman, D., Lowers, H., Meeker, G., Schrader, C., McLemore, C., and Fikes, J. *The LHT (Lunar Highlands Type)*

regolith simulant series. The Geological Society of America (GSA) 2008 Joint Annual Meeting. Houston, Texas, 2008.

[123] Stommel, Y.G., and Riebel, U. *A corona-discharge-based aerosol neutralizer designed for use with the SMPS-system.* J. Electrostatics, 63: 917-921, 2005.

[124] Stubbs, T.J., Vondrak, R.R., and Farrell, W.M. *Impact of dust on lunar exploration*. in *Proceedings of Dust in Planetary Systems*, (Workshop, 26-30 September 2005, Kauai, Hawaii), edited by: Krüeger, H. and A. L. Graps, 239-243, Eur. Space Agency Publ., SP-643, 2007,

[125] Taylor, L.A., Schmitt, H.H., Carrier, W.D., and Nakagawa, M. *The lunar dust problem: from liability to asset*. 1st Space Explor. Conf., AIAA, Orlando, Florida, 2005 (http://hefd.jsc.nasa.gov/toxladtag.htm).

[126] Vivas, M.M., Hontañón, E., and Schmidt-Ott, A. *Reducting multiple charging of submicron aerosols in a corona diffusion charger*. Aerosol Sci. Technol. 42: 97-109, 2008.

[127] Wang, S.C., and Flagan, R.C. *Scanning Electrical Mobility Spectrometer*. Aerosol Sci. Technol., 13: 230-240, 1990.

[128] Wang, J., Shin, W.G., Mertler, M., Sachweh B., Fissan, H., and Pui, D.Y.H. *Measurement of nanoparticle agglomerates by combined measurement of electrical mobility and unipolar charging properties*. Aerosol Sci. & Technol., 44: 97-108, 2010.

[129] Watson, J.H.P. *Magnetic Filtration*. J. Appl. Phys., 44(9): 4209-4213, 1973.

[130] Watson, J.H.P. *Approximate Solutions of the Magnetic Separator Equations*. IEEE Trans. Magn., 14(4): 240-245, 1978a.

[131] Watson, J.H.P. *Improvements of a Low-Field, High-Intensity Matrix Separator*. IEEE Trans. Magn., 14(5): 392-394, 1978b.

[132] Whitby, K.T. *Generator for producing high concentrations of small ions.* The Review of Scientific Instruments, 32(12): 1351-1355, 1961.

[133] Wood, D.M. *Classical Size Dependence of the Work Function of Small Metallic Particles.* Physical Review Letters, 46: 749, 1981.

[134] Ying, T.-Y., Yiacoumi, S., and Tsouris, C. *High-gradient magnetically seeded filtration*. Chem. Eng. Sci., 55: 1101-1113, 2000.

[135] Young, H.D., and Freedman, R.A. *Sears and Zemansky's university physics with modern physics*, 11th Ed., Addison Wesley, Reading, MA, 2003.

[136] Yu, C.P. *Theories of electrostatic lung deposition of inhaled aerosols.* Ann. Occup. Hyg., 29: 219-227, 1985.

[137] Zarutskaya, T., and Shapiro, M. *Capture of nanoparticles by magnetic filters*. J. Aerosol Sci., 31(8): 907-921, 2000.

[138] Zhuang, Y., Kim, Y.J., Lee, T.G., Biswas, P. *Experimental and theoretical studies of ultra-fine particle behavior in electrostatic precipitators*. J. Electrostatics, 48: 245-260, 2000.

Appendix A

A Miniature Disk Electrostatic Aerosol Classifier (mini-disk EAC) For Personal Nanoparticle Sizers

Lin Li[1], Da-Ren Chen[1], Chaolong Qi[2], and Pramod S. Kulkarni[2]

[1]Department of Energy, Environmental & Chemical Engineering

Washington University in St. Louis

One Brookings Drive, Box 1180

St. Louis, Missouri 63130, U.S.A.

[2] Centers for Disease Control and Prevention

National Institute for Occupational Safety and Health

4676 Columbia Pkwy, MS: R3

Cincinnati, OH, 45226

Journal of Aerosol Science

Abstract

We have developed a miniature disk electrostatic aerosol classifier (mini-disk EAC) for use in electrical mobility-based personal nanoparticle instrumentation for measurement of personal exposures to nanoaerosols. The prototype consists of two parallel disk electrodes separated by an electrically insulating spacer, to create the particle classification zone. The aerosol enters and exits the classification zone along the bottom disk electrode. An additional, particle-free sheath flow is used to improve the measurement resolution. The transmission measurement of the mini-disk EAC for DMA-classified particles shows that particle losses due to diffusion and electrical image forces were low. The particle penetration at 10 nm diameter (the designed lower size limit for the classifier) was 67% when the prototype was operated at the aerosol and sheath flow rates of 0.5 and 1.0 l min^{-1}, respectively. The performance of the mini-disk EAC was experimentally characterized using the particle cutoff curves that describe their penetration through the classifier as a function of applied voltage across the two disk electrodes. Based on the measurement of particle penetration at different aerosol and sheath flows, it was found that the aerosol and sheath flow rates of 0.5 and 1.5 l min^{-1} were optimal for classifier operation. Finally, a semi-empirical model was also developed to describe the transfer function of the mini-disk EAC for non-diffusive particles.

Keywords: miniature mobility classifier, nanoparticle sizer, personal aerosol exposure

1. Introduction

Particles in the submicron and nanometer range are often encountered in the exhaust of combustion sources, chemical processes and aerosol reactors (Hildemann et al., 1991). Examples of combustion sources and processes include waste incinerators, welding processes, cooking ovens, smelters, nuclear reactor accidents, utility boilers, and the exhaust from automobile, trucks, and jet aircraft (Biswas and Wu, 1998). Meanwhile, nanoparticles of different physical and chemical properties - the building bocks for Nanotechnology - have been synthesized in chemical reactors for modern industrial applications. Examples of such nano-materials are carbon black, pigments, and other nano-materials for technological applications such as optical waveguides and advanced ceramic powders (Biswas and Wu, 2005). While unique functionalities of nanoparticles make them attractive for technological applications, the very same properties may possibly create adverse health effects. As a result, there is a growing concern over the potential health risks from exposure to these materials in industrial environments. Recent toxicological studies of fibrous and tubular nanoparticles (Lam et al. 2004; Poland et al. 2008; Shvedova et al. 2003; Shvedova et al. 2004; Warheit et al. 2004; Warheit 2006) have shown that at extremely high doses these materials are associated with fibrotic lung responses and result in inflammation and an increased risk of carcinogenesis. Data on personal exposure to engineered nanomaterials is very limited, partially due to lack of suitable instrumentation. Therefore, miniature, low-cost instrumentation to monitor personal exposure to nanoparticles in the workplace will play an important role in design and implementation mitigation strategies.

Existing personal particle samplers are primarily focused on particles larger than 0.1 μm. In these devices, particles are inertially separated and then collected at different stages within the personal impactors or cyclones. The manual measurement for the particle mass collected on each impactor/cyclone stage after the exposure is necessary (Lee et al., 2006, Misra et al., 2002, Koch et al., 1999; Chen et al., 1999). These samplers have been widely applied for particle measurements in different environments (Liu et al., 2002, Mader et al., 2001). While the inertial-separation-based devices work well in separating particles in the supermicrometer and upper submicrometer range, they are not effective for collecting particles in lower submicrometer and nanometer size range.

Electrical mobility-based particle sizing techniques, on the other hand, are ideal for measuring nanometer sized particles down to 1 nm. A typical electrical mobility-based particle sizer consists of three essential components: a particle charger to electrically charge the sampled particles to a known charge distribution, a particle electrical mobility-based classifier, and an aerosol detector to measure the concentration of the classified particles. Widely used mobility-based instruments that measure particle size distributions in the lower submicron and nanometer range, such as the scanning mobility particle sizer (SMPS; TSI model 3936), are more suitable for laboratory and scientific studies. Their size, weight, and cost are prohibitive for their use as personal exposure monitors.

To develop the miniature version of electrical mobility particle sizer, it is necessary to significantly reduce the size of the aerosol charger, the particle classifier, and the detector. To address these concerns, Qi et al. (2008) have recently developed a miniature, low-cost disk-type electrostatic aerosol precipitator. Despite its compact size,

the prototype device provides satisfactory penetration for charged particles. Qi et al. further developed a semi-empirical model to describe the penetration curves of charged particles through the precipitator. While the mini-disk precipitator performs well for the task of altering the size distribution of sampled particles, it can not separate charged particle via selected electrical mobility, consequently, making it difficult to retrieve more precise particle size distribution.

For use in personal nanoaerosol sizer, we have designed and evaluated a new miniature disk electrostatic aerosol classifier (mini-disk EAC). The prototype used parallel disk geometry and is described in detail in the following section. A similar electrostatic aerosol analyzer (EAA) that uses radial flow configuration has been developed before (Pourprix and Daval, 1990). The principal difference between the previous designs and our current prototype is in the design of the aerosol and the sheath flow directions. The device developed by Pourprix and Daval (1990), introduced a design where both the aerosol and sheath flows come from the outer edge of parallel disks while ours reverses the direction of both flows. Moreover, the size of our prototype is significantly smaller compared to the earlier designs. Differential mobility analyzers (DMAs) with the radial configuration, i.e., the Spectromètre de Mobilité Electrique Circulaire (SMEC) and the Radial Differential Mobility Analyzer (RDMA), have also been developed (Pourprix, 1994; Zhang et al, 1995). The inclusion of monodisperse aerosol flow channels in these radial flow DMAs potentially increases the manufacturing cost for personal particle sizers. Low cost is the primary reason for adopting an EAA-type scheme in this work compared to DMA-type differential classification scheme.

In the following sections, we report on the design of the mini-disk EAC and on the experimental evaluation of its performance. We evaluated the performance of our prototype by measuring the penetration efficiency of particles with a specific electrical mobility as a function of applied voltage at a fixed aerosol flow rate. A critical electrical mobility Z_{pc}, defined as the electrical mobility of particles having 50% penetration as they pass through the prototype for a given voltage, can then be determined from the penetration measurement. A simple model was further derived in this study to predict the performance of the prototype. Furthermore, the experimental transfer function of the mini-disk EAC was retrieved based on the deconvolution scheme assuming non-diffusive transfer function for DMA and compared with the theoretical transfer function from the proposed model.

2. Design of the Miniature disk Electrical Aerosol Classifier

The schematic diagram of mini-disk EAC with critical dimensions is shown in Fig. 1. The prototype consists of a top metal disk electrode and a bottom metal disk electrode, which is embedded in the delrin cavity case. The particle classification region in the miniature classifier is created by the space between the top disk electrode plate and the bottom disk electrode; the gap between the two electrodes is controlled by an electrically insulating spacer of 1.6 mm height. Electrically charged particles are introduced into the classification region through the circular entrance slit, formed by a flange centrally attached to the aerosol entrance tube and the cave-in at the center of the bottom disk electrode. The spacing and aerosol flow injection angle of the entrance slit is controlled by the contours of the tube flange and of the cave-in. The particle-free sheath

flow is delivered to the classification region by a flow entrance, formed by the annular space between central aerosol tube and an outer tube. The sheath flow is supplied through a side tube as shown in Fig. 1. Three annular slots, located close to the outer edge the bottom disk electrode, allow aerosol to exit from the classification region. Classified particles, after passing through the annular slots, merge together and then leave through the central tube at the bottom.

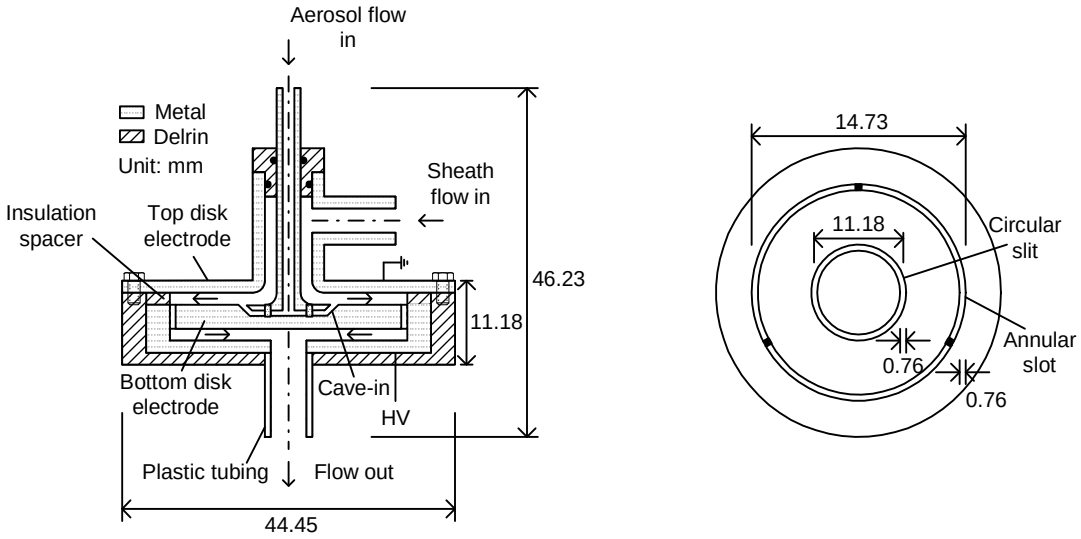

Figure 1 Schematic diagram of prototype miniature disk electrical aerosol classifier

High electrical potential is applied to the bottom disk electrode. The top metal disk electrode plate is electrically grounded. Since the aerosol enters the classification region along the bottom electrode, it will be necessary to maintain the polarity of the bottom electrode same as that of the aerosol particles in order to classify the particles. When a uniform electrical field is established between the electrodes, the trajectories of charged particles in the classification region will deflect towards the top disk plate.

Particles with sufficiently high electrical mobility will deposit on the top metal disk, and those with less mobility will exit the classifier.

Compared with the miniature disk-type electrostatic aerosol precipitator designed by Qi et al., a sheath flow is introduced into this the mini-disk EAC, which could provide the opportunity to separate charged particle based on their electrical mobility and give more precise information for retrieving particle size distribution.

3. Experimental Setup for the Evaluation of Miniature disk Electrical Aerosol Classifier

Shown in Fig. 2 is the schematic diagram of the experimental setup used for the performance evaluation of mini-disk EAC. Two different techniques were used to generate test aerosols. Polydisperse Ag particles with electrical mobility diameters ranging from 10 to 50 nm were generated by the evaporation-condensation technique (Scheibel and Porstendörfer, 1983). Ag powder was placed in a ceramic boat located in a high temperature tube furnace (Lindberg/Blue Model CC58114A-1). Nitrogen at the flow rate of 1.5 l min^{-1} was used as the vapor carrier gas, passing through a tube placed in the furnace. The flow rate of the carrier gas was regulated and monitored by a needle valve and a laminar flow meter prior to its introduction to the furnace tube. The powder material in the ceramic boat was evaporated at high temperature, and its vapor was carried out by the nitrogen gas flow. At the exit of the furnace tube, polydisperse nanoparticles were formed by mixing the vapor carrier gas with particle-free air at room temperature. A constant-output, custom-made atomizer was used to produce KCl particles with electrical mobility sizes from 50 to 120 nm (Liu and Pui, 1974). The flow

rate output from the atomizer was 4.0 l min^{-1} when the compressed air pressure was at 30 psig. Droplets produced by the atomizer were passed through a Po^{210} radioactive neutralizer to remove electrical charges on the particles, and also through a diffusion dryer to remove the solvent in droplets.

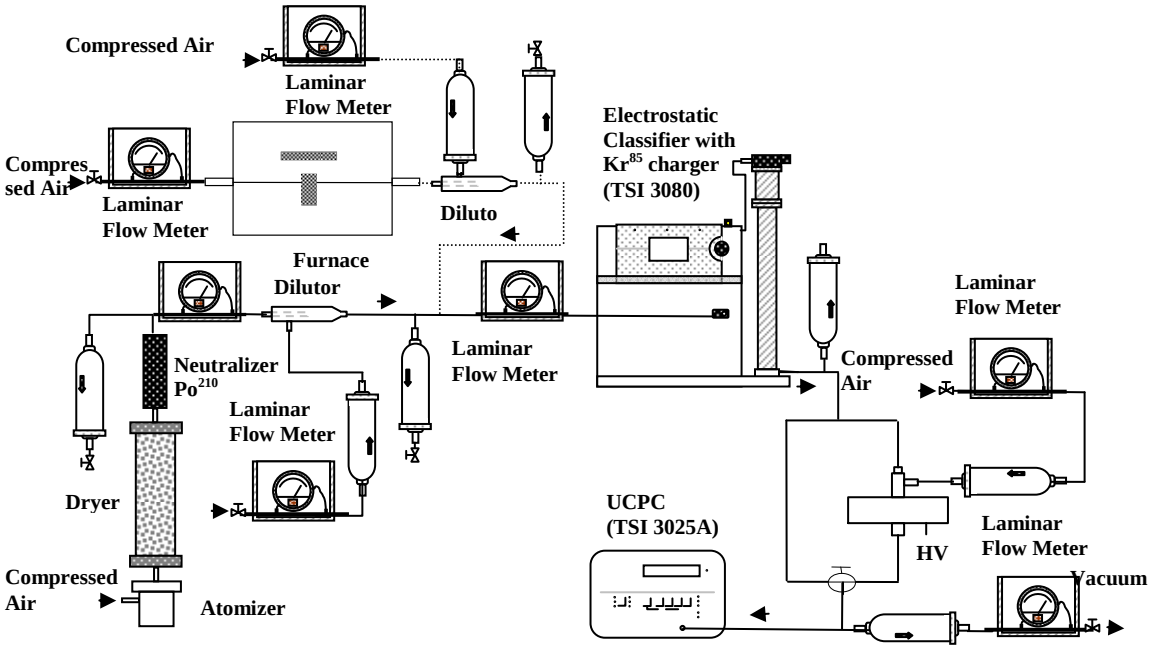

Figure 2 Experimental setup for the measurement of particle penetration and cutoff curves

A differential mobility analyzer (DMA, TSI Model 3081) was used downstream from the polydisperse aerosol generation systems to obtain near-monodisperse particles of desired sizes. Prior to introducing into the DMA, the polydisperse aerosol was passed through a Kr^{85} radioactive bipolar charger to impart a steady state charge distribution (Knutson and Whitby 1975). The DMA was operated at an aerosol flow rate of 1.0 l min^{-1} and at the sheath flow rate of 10.0 l min^{-1}. Since the mini-disk EAC can be operated at different aerosol and sheath flow rates, clean compressed air was used as the sheath flow

regulated and monitored by a needle valve and a laminar flow meter. The total flow rate of the mini-disk EAC was controlled by an Ultrafine Condensation Particle Counter (UCPC, TSI model 3025A), operated at a high flow rate, and a vacuum pump with a needle valve.

The transmission efficiency of singly charged particles through the prototype was first measured at different particle sizes. In this part of the experiment, particle number concentrations both upstream and downstream of the mini-disk EAC, N_{up} and $N_{dn}(0)$ respectively, were measured by a UCPC. The particle transmission efficiency was then obtained by the ratio of $N_{dn}(0)$ and N_{up}:

$$Transmission = \frac{N_{dn}(0)}{N_{up}}. \quad (1)$$

To measure the particle cutoff curves of the mini-disk EAC, DMA-classified aerosol were directly introduced into the classifier. For each electrical mobility of the DMA-classified aerosol, we first measured the particle concentration downstream from the mini-disk EAC with no voltage applied, i.e. $N_{dn}(0)$. Downstream particle concentrations at different voltage settings, $N_{dn}(V)$, were then measured. As applied voltage was gradually increased from zero, more number of particles precipitated on the top electrode. All charged particles eventually precipitated when sufficiently high voltage was applied. The particle cutoff curve for a given electrical mobility of the DMA-classified aerosol was obtained by the measured particle penetration (P) as a function of applied voltage:

$$P = \frac{N_{dn}(V)}{N_{dn}(0)}. \quad (2)$$

4. Results and Discussion

4.1 Particle Transmission Efficiency

Fig. 3 shows the measured transmission efficiency of singly charged particles through the mini-disk EAC operated at an aerosol flow rate (Q_a) of 0.5 l min^{-1} and the sheath flow rate (Q_{sh}) of 1.0 l min^{-1}. Monodisperse particles in the diameters ranging from 10 to 120 nm were used for the measurement. It is evident that the particle loss is not significant despite the narrow spacing of the classification region. The loss of particles larger than 60 nm is negligible. As expected the loss of singly charged particles in the prototype increases as the particle size decreases. The singly charged particle penetration of the prototype reduces to 67% at 10 nm. More, the data-fitted equation in Fig. 3 can be used in the data reduction scheme to recover the size distributions for particles larger than 10 nm in diameter.

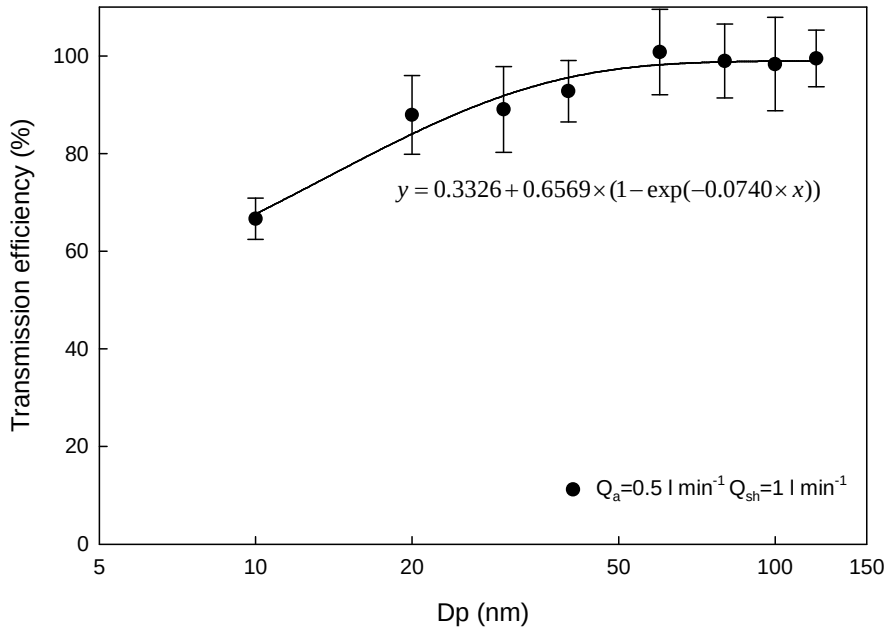

Figure 3 Transmission efficiency of singly charged particles in the mini-disk EAC

4.2 Penetration curves of Miniature disk Electrical Aerosol Classifier

The performance of mini-disk EAC is characterized by the so-called particle cutoff or penetration curve, which describes the particle penetration as a function of applied voltage. During the performance characterization, the top disk electrode of the disk classifier was electrically grounded, and high voltage was applied at the bottom electrode.

Shown in Fig. 4 are the cutoff curves of particles 80 nm in diameter that have different aerosol flow rates but a constant total flow rate (Q_t) of 1.5 l min^{-1} (i.e., Q_a+Q_{sh}). The measured particle penetration at voltage V was normalized with transmission efficiency at V=0 and the applied voltage was normalized using V_{50}, the voltage at 50% particle penetration. The standard deviation for each data point includes the UCPC fluctuation. As expected, the slope of particle cutoff curves, defined as the slope of lines tangential to the 50% normalized particle penetration, increases with the decreasing ratio of the aerosol to the sheath flow rates ($\beta = \frac{Q_a}{Q_{sh}}$). The results also show that sharpness of cut-off couldn't be significantly improved when the Q_a was reduced below 0.5 l min^{-1}. It is worth noting that a lower β also means greater dilution of the aerosol flow exiting the classifier. Dilute particle concentration may present difficulties in aerosol concentration measurement, particularly if one is using Faraday cage electrical detectors. Therefore it is desirable to operate the classifier at the highest possible aerosol flow rate and the lowest acceptable aerosol-to-sheath flow rate ratio. With the above consideration, the prototype was operated at the Q_a=0.5 and Q_t= 1.5 l min^{-1}, respectively, for the subsequent experiments.

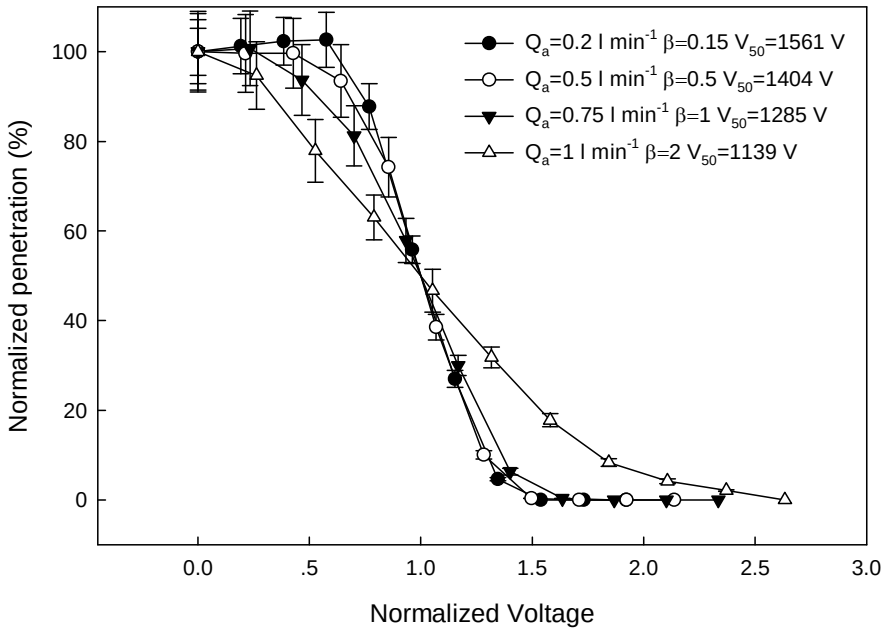

Figure 4 Particle cutoff curves of the disk classifier for 80 nm particles at different aerosol flow rate while keeping the total flow rate of 1.5 l min^{-1}: Normalized penetration vs. normalized voltage

Shown in Fig. 5(a) are V_{50} for 80 nm particles when the classifier was operated at different values of Q_t but at constant Q_a of 0.5 l min^{-1}. The results demonstrate that higher voltage is required to achieve the same particle penetration efficiency as Q_t increases, keeping the Q_a constant. Shown in Fig. 5(b) are the particle cutoff curves with the normalized voltage abscissa for 80 nm particles when the classifier was operated at different values of Q_t but at constant Q_a of 0.5 l min^{-1}. In the figure, the measured penetration is normalized with respect to transmission efficiency at V=0. All the data at different applied voltages collapse into one curve. This indicates that the effect of β on the characteristics of penetration curves of the mini-disk EAC is negligible when β<0.5.

Since lower voltages are preferable for personal instrumentation applications, it is desirable to maintain lower sheath flow rates in the classifier. Therefore, it is desirable to operate the mini-disk EAC at a $Q_t \leq 1.5$ l min^{-1} and $\beta = 0.5$.

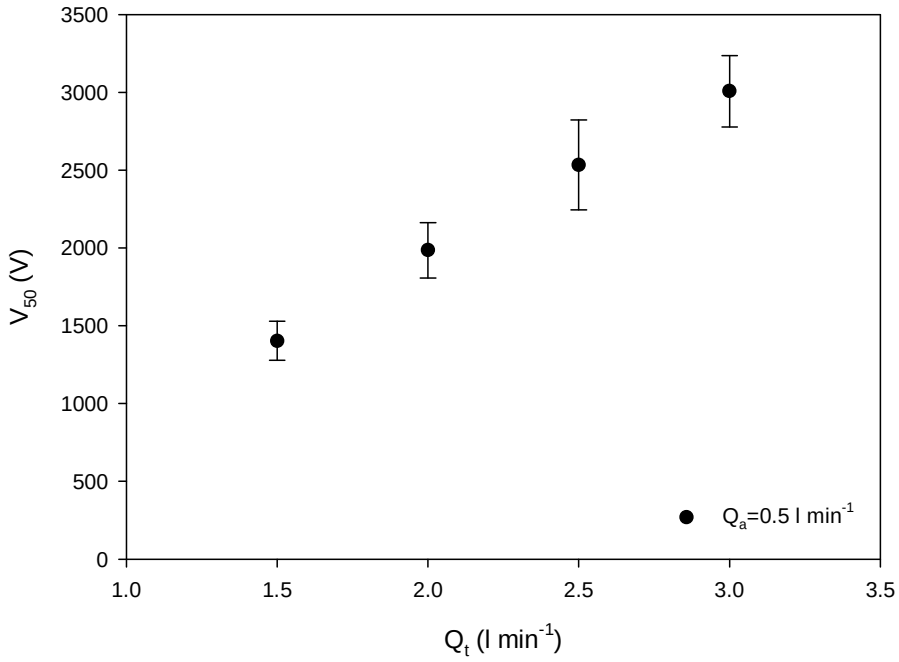

Figure 5(a) Voltages at a 50% penetration (V_{50}) for 80 nm particles when the classifier was operated at different total flow rate while keeping the aerosol flow rate of 0.5 l min^{-1}

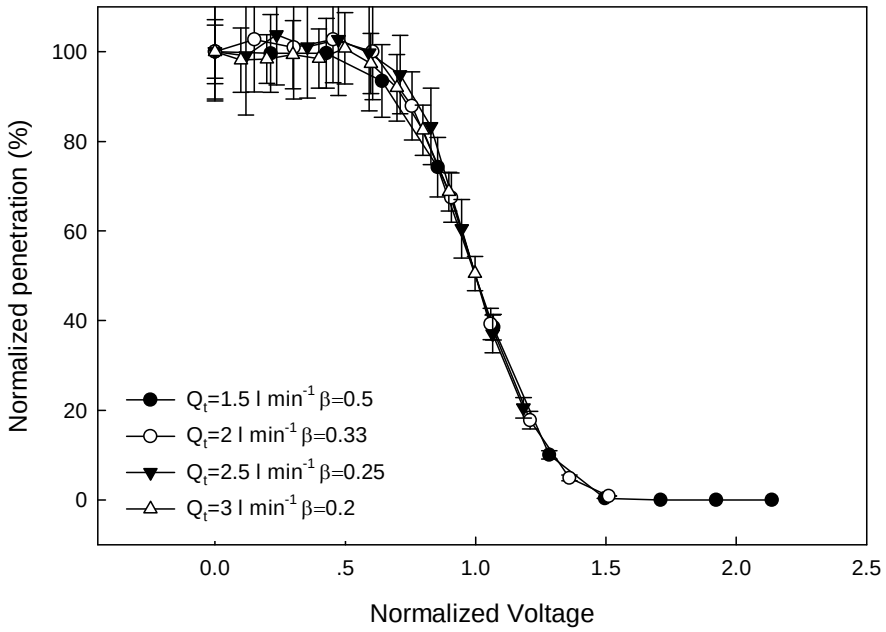

Figure 5(b) Particle cutoff curves of 80 nm particles when the classifier was operated at the aerosol flow rate of 0.5 l min^{-1} while varying the total flow rate: Normalized penetration vs. normalized voltage

Shown in Fig. 6(a) are particle cutoff or penetration curves for different DMA-classified particle diameters when the prototype is operated at Q_a= 0.5 and Q_t=1.5 l min^{-1}, respectively. Y-axis represents the measured penetration efficiency normalized with transmission efficiency at V=0. As expected, the V_{50} increased with the increasing particle diameter. The critical electrical mobility Z_{pc}, defined as the electrical mobility of particles having 50% penetration as they pass through the prototype for any given voltage, can thus be determined from the particle cutoff curves. Fig. 6(b) shows the same data shown in Fig. 6(a) except that the normalized voltage was used as the abscissa. The curves

collapse into one curve in Fig. 6(b). This shows that the penetration characteristics, or the transfer function of the classifier, are relatively constant over the size range of interest.

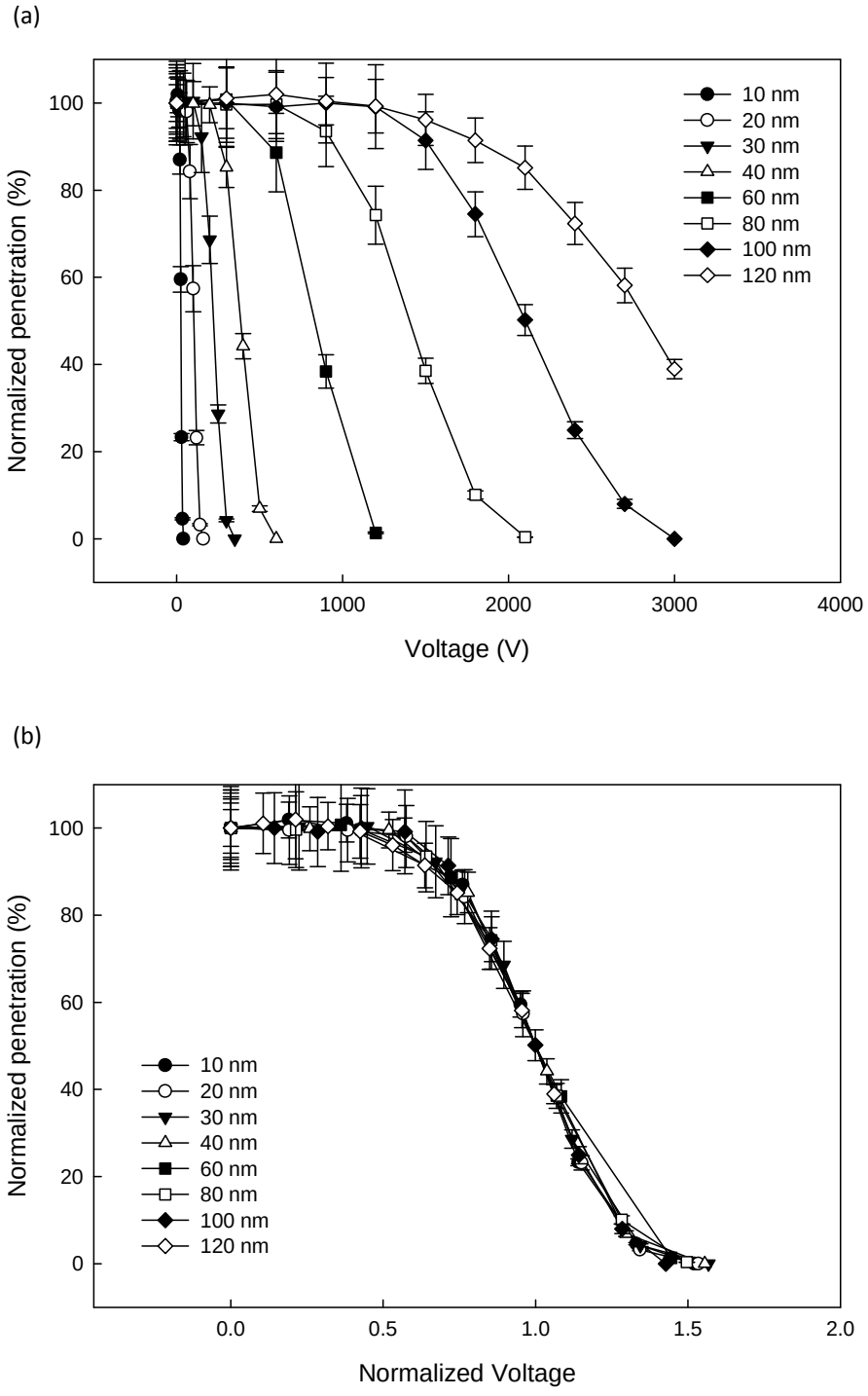

Figure 6 Particle cutoff curves of different particle sizes when the classifier was operated at the aerosol and total flow rates of 0.5 and 1.5 l min^{-1}, respectively: (a) Normalized penetration vs. applied voltage; (b) Normalized penetration vs. normalized voltage

5. Semi-empirical Model to Describe the Transfer Function of the Mini-disk EAC

The transfer function is defined as the probability that an aerosol particle which enters the mobility analyzer via the aerosol inlet will leave via the aerosol outlet. The difference between the transfer function and the cutoff curve of the mini-disk EAC is that the cutoff curve is actually the convolution of transfer functions of both the DMA and the mini-disk EAC. There are three reasons for developing a model to describe the particle transfer function of the prototype. One is to understand the fundamental precipitation mechanism governing the prototype. Another is that the developed model can be used to predict the particle transfer functions of different sizes when the operational condition of the prototype is varied. The third reason is that such a model will be necessary for data inversion scheme to recover particle size distributions.

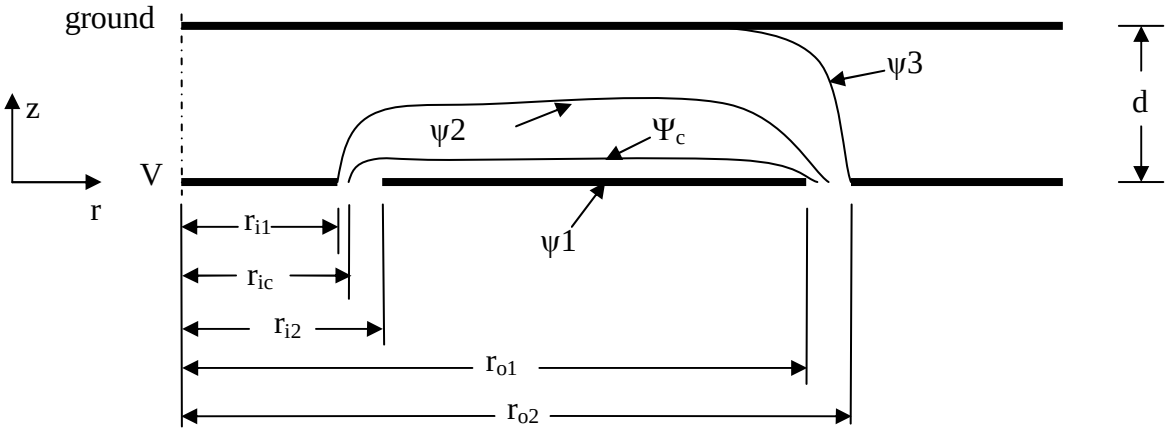

Figure 7 Illustration of the particle classification region in the prototype used in the modeling. Included in the illustration are flow streamlines for defining polydisperse aerosol, sheath and total flow rates.

Shown in Fig. 7 is the simplified particle classification region of the classifier. Due to the axisymmetric geometry of the prototype, only half of the classification region is shown. Cylindrical coordinate system, with the r and z denoting the radial and axial coordinates, respectively, is used in the following derivation. Neglecting the particle inertial and diffusion effects on the particle transport behavior in the classification region, we find that the trajectory of a charged particle is governed by the following equations:

$$\frac{dr}{dt} = u_r + Z_p E_r , \tag{3}$$

$$\frac{dz}{dt} = u_z + Z_p E_z , \tag{4}$$

where, Z_p is the electrical mobility of the particle, calculated as

$$Z_p = \frac{neC_c}{3\pi\eta d_p} \tag{5}$$

in which n is the number of elemental electrical charges on particles, C_c the Cunningham correction factor, η the gas viscosity; u_r and u_z the radial and axial components of the flow velocity; and E_r and E_z the respective components of the electrical field. In this derivation, we also assume that the electrical field distortion at the aerosol entrance and outlet is negligible because of the narrow slit spacing. The electrical field is thus constant in the axial direction and zero in the radial direction. Similarly, we assume the flow distortion at the aerosol inlet and outlet to be negligible. The flow velocity in the

classification region of mini-disk EAC is therefore assumed to be in the radial direction only.

With the above assumptions, the particle stream function formulation for non-diffusive particles is used (Knutson and Whitby; 1975):

$$\Gamma(r,z) = \psi(r,z) + Z_p \Phi(r,z) \tag{6}$$

which is expressed in terms of the fluid stream function ψ and the corresponding electric flux function Φ. Assuming that the flow is incompressible, laminar and axisymmetric, one can define the stream function and electric flux function by Eqs. (7, 8) as follows:

$$\psi(r,z) = \int^{r,z} [ru_r dz - ru_z dr], \tag{7}$$

$$\Phi(r,z) = \int^{r,z} [rE_r dz - rE_z dr] = \int^{r,z} [-rE_z dr]. \tag{8}$$

Since it is assumed that the particles are non-diffusing, the particle stream function remains constant along the particle trajectory. Therefore the following equation applies for the trajectory of particles with a given electrical mobility:

$$\Delta\psi = -Z_p \Delta\Phi . \tag{9}$$

Three key streamlines, ψ_1, ψ_2, and ψ_3, can be defined in the classification region and are shown in Fig 7. The streamlines ψ_1 and ψ_2 bound the aerosol flow entering through the entrance slit. The streamlines ψ_2 and ψ_3 bound the sheath flow. Since both aerosol flow Q_a and sheath flow Q_{sh} exit the device from the same slot, the streamlines ψ_1 and ψ_3 form the boundaries of the total flow. The flow rates of Q_a and Q_{sh} can be then described as:

$$Q_a = 2\pi(\psi_2 - \psi_1), \tag{10}$$

$$Q_{sh} = 2\pi(\psi_3 - \psi_2). \tag{11}$$

When charged particles having electrical mobility Z_P enter the classification region and the voltage V applied to the bottom electrode, some particles are attracted to the upper ground plate by the electrical field. A critical streamline ψ_c can thus be defined. Particles entering the classification region between the streamlines ψ_2 and ψ_c are precipitated, where $\psi_1 \le \psi_c \le \psi_2$, while the others exit the region. Therefore, particles entering at streamline ψ_c move to streamline ψ_3 when they exit, and it can be described by the following equation:

$$\psi_c = \psi_3 + Z_p \Delta\Phi, \tag{12}$$

$$\Delta\Phi = \int_{r_{ic}}^{r_{o2}} -rE_z dr = -\frac{r_{o2}^2 - r_{ic}^2}{2}\frac{V}{d}, \tag{13}$$

where r_{ic} is the radial coordinate of the critical streamline ψ_c at the entrance slit; r_{02} is the radius of the streamline ψ_3 at the exit slot .

Assuming the particle concentration at the aerosol entrance is uniform, the particle penetration is give by:

$$P = 1 - \frac{\psi_2 - \psi_c}{\psi_2 - \psi_1}. \tag{14}$$

Submitting Eqs (10) - (13) into Eq. (14), we get:

$$P = 1 + \frac{Q_{sh}}{Q_a} - KV, \tag{15a}$$

where,

$$K = \frac{\pi Z_p}{Q_a d}(r_{o2}^2 - r_{ic}^2). \tag{15b}$$

The boundary condition $\psi_1 \le \psi_c \le \psi_2$ then implies $\frac{Q_{sh} d}{\pi V (r_{o2}^2 - r_{ic}^2)} \le Z_p \le \frac{(Q_{sh} + Q_a) d}{\pi V (r_{o2}^2 - r_{ic}^2)}$. If $\psi_c \le \psi_1$ (i.e., $Z_p \le \frac{Q_{sh} d}{\pi V (r_{o2}^2 - r_{ic}^2)}$), all particles pass through the device (i.e., P = 1). If $\psi_2 \le \psi_c$ (i.e., $\frac{(Q_{sh} + Q_a) d}{\pi V (r_{o2}^2 - r_{ic}^2)} \le Z_p$), all particles are precipitated in the device (i.e., P = 0).

In general, Eq. (15) is rather less useful since P is a function of r_{ic}- a quantity that is not known *a priori*. As an approximation, r_{ic} can be replaced by an average of r_{i1} and r_{i2} [i.e., $r_i = (r_{i1} + r_{i2})/2$]. This error is estimated to be very small for our prototype; the relative difference between the values of $r_{o2}^2 - r_{i1}^2$ and $r_{o2}^2 - r_{i2}^2$ is about 5%. It is estimated that the maximum error introduced by this approximation in Eq. (15) is less than 3%. To take into account the non-ideal conditions such as the electrical field and flow distortion at the aerosol entrance and exit, an empirical coefficient α is introduced in Eq. (15b):

$$K = \frac{\pi Z_p}{Q_a d \alpha} (r_{o2}^2 - r_i^2) . \qquad (16)$$

The particle transfer function as a function of applied voltage for a certain particle size can then be modeled using Eqs (15a) and 16.

Fig. 8 shows the comparison of the experimental and calculated voltages at the 50% particle penetration as a function of electrical mobility for the prototype operated at the aerosol and total flow rates of 0.5 and 1.5 l min^{-1}, respectively. The value of α was assumed to be 1 in these calculations. The excellent agreement between the experimental and the theoretical V_{50} at all tested electrical mobility demonstrates the accuracy and usefulness of this simple model.

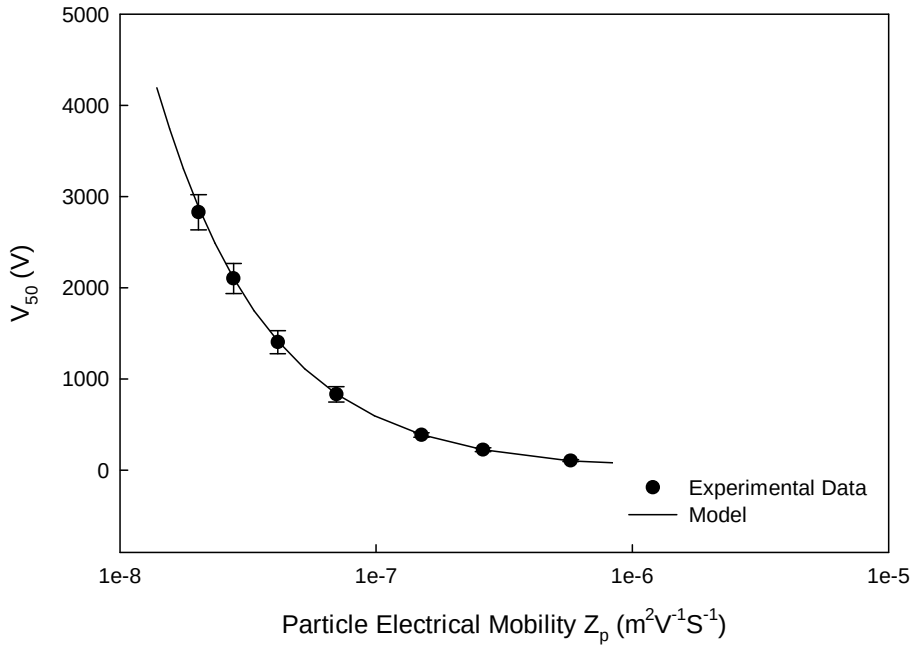

Figure 8 Comparison of the experimental and predicted voltages at a 50% penetration (V_{50}) as a function of test particle electrical mobility.

Since the experimental data is a result of convolution of transfer functions of both the DMA and the mini-disk EAC, the theoretical non-diffusive response of the mini-disk EAC, obtained by convoluting the DMA and the classifier transfer functions is also calculated and shown in Fig. 9(a) as a function of normalized voltage for the mini-disk EAC operated at the Q_a=0.5 and Q_t=1.5 l min^{-1}. In this study, the DMA was operated at a flow rate ratio of 1:10, and the prototype was operated at the flow rate ratio β=0.5. Overall, the slope of the theoretical non-diffusive curve is slightly steeper than that obtained experimentally. However, the agreement between theoretical and experimental values is excellent for penetrations in the range 30-70%.

Fig. 9(b) shows the comparison of experimental and theoretical transfer function as function of normalized voltage for the mini-disk EAC operated at the Q_a=0.5 and Q_t=1.5 l min^{-1}. The experimental transfer function is retrieved based on the deconvolution scheme assuming non-diffusive transfer function for DMA (Li et al., 2006). Overall, the slope of the theoretical non-diffusive curve is also slightly steeper than that obtained by using the experimental data. We also considered the possible experimental errors, possibly both a 10% and a 2% variation for the flow rates of the UCPC (Q_t) and the laminar flow meters (Q_{sh}) through the classifier. The worst-case scenario for the disk classifier transfer function of the non-diffusive particles is also shown in Fig. 9(b). The plot shows that the experimental transfer function with a penetration efficiency ranging from 20 to 70% is close to the theoretical worst case. Other possible reasons for the deviation from the theoretical response could be Brownian diffusion and flow distortion, which could lead to smearing of particle trajectories. The experimental transfer function of the mini-disk EAC can be used in the data-reduction scheme to retrieve a more accurate particle size distribution from the raw data measured by the mini-disk EAC.

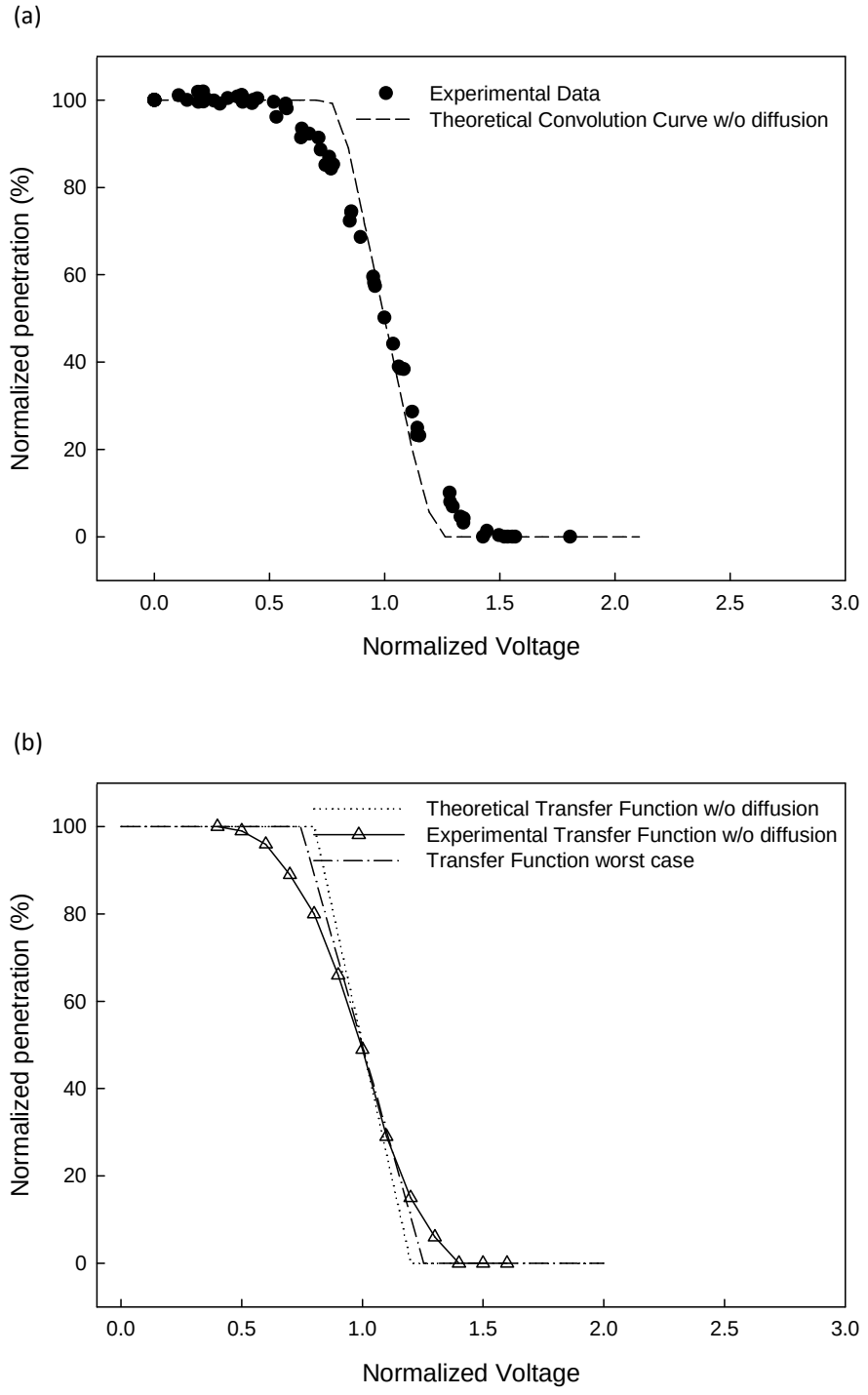

Figure 9 Comparison of experimental and predicted curves as a function of normalized voltage when the classifier was operated at the aerosol and total flow rates of 0.5 and 1.5 l min^{-1}, respectively: (a) cutoff curves; (b) transfer function curves.

6. Conclusion

We report design and development of an electrical mobility-based prototype of a miniature disk electrostatic aerosol classifier intended for use in miniature nanoparticle sizer. This new miniature prototype provides a low-cost solution for miniature nanoparticle sizers, much needed in spatially distributed particle size measurement or personal exposure monitoring. Performance of the prototype was experimentally characterized in the laboratory using DMA-classified aerosols. Despite its compact size, the prototype has satisfactory penetration for singly charged particles, as is evidenced by the penetration measurement of singly charged particles with sizes ranging from 10 to 120 nm. The singly charged particle penetration at the aerosol and sheath flow rates of 0.5 and 1.0 l min^{-1}, respectively, was close to 100% for particles with sizes larger than 60 nm. The penetration decreases as the particle size decreases. The penetration of charged particles through the prototype was at 67% at a particle size of 10 nm (i.e., the lower limit of a particle size targeted for the prototype). The performance of the prototype was experimentally characterized by so-called the particle cutoff curves, i.e., the normalized penetration vs. the normalized voltage. The particle cutoff curves were obtained at different combinations of aerosol and sheath flow rates in the experimental evaluation of prototype performance. From the experimental data, we recommend the prototype to be operated at the aerosol and sheath flow rates of 0.5 and 1.0 l min^{-1}, respectively. The recommended flow rate operation for the prototype is determined by the facts that (1) the slope of the prototype's particle cutoff curves would not be further improved with the aerosol-to-sheath flow rate ratio less than 0.5; (2) the aerosol concentration would be further diluted when a lower aerosol-to-sheath flow ratio is used—a drawback is one is

using electrical detectors downstream. In addition to the experimental evaluation, the methodology used by Knutson and Whitby (1975) for DMA analysis was applied to develop a semi-empirical model for the description of the particle transfer function of the prototype. The comparison between the experimental data and the prediction shows that the model successfully predicts the voltages at a 50% penetration of particles with different electrical mobilties. However, a comparison between the experimental and the calculated cutoff curves shows that the slope of the theoretical particle cutoff curve is slight larger than experimental curve. The slight difference in the experimental and theoretical slopes may be attributed to particle diffusion and flow distortion in the classification region which leads to smearing of trajectories. Nonetheless, the developed model can be used to optimize the mini-disk EAC performance. The experimental particle transfer function of the mini-disk EAC was also obtained by the deconvolution scheme. The experimental transfer function of the disk classifier can be used in the data-reduction scheme to retrieve more accurate particle size distribution from the raw data collected by miniature nanoparticle sizers utilizing the mini-disk EAC as the size altering component.

Acknowledgement

LL and DRC are grateful for the financial support provided by National Institute for Occupational Safety and Health through the subcontract (#22-001322-62343) to Washington University in St. Louis.

Disclaimer

The findings and conclusion in this report are those of the author(s) and do not necessarily represent the views of the National Institute for Occupational Safety and Health

References

[1] Biswas, P., & Wu, C.Y. (1998). Control of toxic metal emissions from combustors using sorbents: a review. *Journal of Air & Waste Management Association, 48,* 113-127.

[2] Biswas, P., & Wu, C.Y. (2005). Nanoparticles and the Environment. *Journal of Air & Waste Management Association, 55,* 708-746.

[3] Chen, C.C., Huang, S.H., Lin, W.Y., Shih, T.S., & Jeng, F.T. (1999). The Virtual Cyclone as a Personal Respirable Sampler. *Aerosol Science and Technology, 31,* 422-432.

[4] Hildemann, L. M., Markowski G. R., Jones, M. C., & Cass, G. R. (1991). Submicrometer Aerosol Mass Distributions of Emissions from Boilers, Fireplaces, Automobiles, Diesel Trucks, and Meat-Cooking Operations. *Aerosol Science and Technology 14,* 138-152.

[5] Knutson, E.O., & Whitby, K.T. (1975). Aerosol Classification by Electric Mobility: Apparatus, Theory, and Applications. *Journal of Aerosol Science, 6,* 443-421.

[6] Koch, W., Dunkhorst, W., & Lodding, H. (1999). Design and Performance of a New Personal Aerosol Monitor. *Aerosol Science and Technology, 31,* 231-246.

[7] Lam C.W., James J.T., McCluskey R., & Hunter R.L. (2004). Pulmonary toxicity of single-wall nanotubes in mice 7 and 90 days after intratracheal instillation. *Toxicological Sciences, 77,* 126-134.

[8] Lee, S.J., Demokritou, P., Koutrakis, P., & Delgado-Saborit, J.M. (2006). Development and evaluation of personal respirable particulate sampler (PRPS). *Atmospheric Environment, 40,* 212-224.

[9] Liu, B.Y.H., & Pui, D.Y.H. (1974). A Submicrion Aerosol Standard and the Primary, Absolute Calibration of the Condensation Nuclei Counter. *Journal of Colloid and Interface Science, 47,* 155-171.

[10] Liu, L.-J., Slaughter, J.C., & Larson, T.V. (2002). Comparison of Light Scattering Devices and Impactors for Particulate Measurements in Indoor, Outdoor, and Personal Environments. *Environmental Science & Technology, 36,* 2977-2986.

[11] Mader, B.T., Flagan, R.C., & Seinfeld, J.H. (2001). Sampling Atmospheric Carbonaceous Aerosols Using a Particle Trap Impactor/Denuder Sampler**.** *Environmental Science & Technology, 35,* 4857-4867.

[12] Misra, C., Singh, M., Shen, S., Sioutas, C., & Hall, P.M. (2002). Development and evaluation of a personal cascade impactor sampler (PCIS). *Journal of Aerosol Science, 33,* 1027-1047.

[13] Oberdörster, G., Oberdörster, E., & Oberdörster, J. (2005). Nanotoxicology: an emerging discipline evolving from studies of ultrafine particles. *Environ. Health Perspect., 113,* 823-839.

[14] Poland C.A., Duffin R., Kinloch I., Maynard A., Wallace W.A.H., Seaton A., Stone V., Brown S., MacNee W., & Donaldson K., (2008). Carbon nanotubes introduced into the abdominal cavity of mice show asbestos-like pathogenicity in a pilot study. *Nature Nanotechnology, 3,* 423-428.

[15] Pourprix, M. (1994). Sélecteur de particules chargées, a haute sensibilité", Brevet francais No 94 06273, 24 Mal..

[16] Pourprix, M., & Daval, J. (1990). Electrostatic precipitation of aerosol on wafers, a new mobility spectrometer, in "Aerosols: Science, Industry, Health and Environment", (proceedings on the Third International Aerosol Conference, 24-27 Sept. 1990, Kyoto, Japan), Volume II, edited by S. Masuda and K. Takahashi, pp797-800, Pergamon Press.

[17] Qi, C., Chen, D.-R., & Greenberg, P. (2008). Fundamental Study of a Miniaturized Disk-type Electrostatic Aerosol Precipitator for a Personal Nanoparticle Sizer. *Aerosol Science and Technology, 42,* 505-512.

[18] Scheibel, H.G., & Porstendörfer, J. (1983). Generation of monodisperse Ag- and NaCl-aerosol with particle diameters between 2 and 300 nm. *Journal of Aerosol Science, 14,* 113-126.

[19] Shvedova A.A., Castranova V., Kisin E., Schwegler-Berry D., Murray A.R., Gandelsman V.Z., Maynard A., & Baron P. (2003). Exposure to carbon nanotube material: assessment of nanotube cytotoxicity using human keratinocyte cells. *J. Toxicol Environ Health, A 66,* 1909-1926.

[20] Shvedova A.A., Kisin E., Murray A.R., Schwegler-Berry D., Gandelsman V.Z., & Baron P. (2004). Exposure of human bronchial cells to carbon nanotubes caused oxidative stress and cytotoxicity. In: Proceedings of the Meeting of the SFRR Europe 2003, Ioannina, Grèce, 91-103.

[21] Wang, S.C., & Flagan, R.C. (1990). Scanning Electrical Mobility Spectrometer. *Aerosol Sci. Technol., 13,* 230-240.

[22] Warheit, D. B. (2004). Nanoparticles: heath impacts. *Materials Todays, 7,* 32-35.

[23] Warheit D.B., Webb T..R, Sayes C.M., Colvin V., & Reed K. (2006). Pulmonary Instillation Studies with Nanoscale TiO2 Rods and Dots in Rats: Toxicity is not Dependent Upon Particle Size and Surface Area. *Toxicological Sciences, 91 (1),* 227-236.

[24] Li, W., Li, L., & Chen, D.-R. (2006). Technical Note: A New Deconvolution Scheme for the Retrieval of True DMA Transfer Function from Tandem DMA Data. *Aerosol Science and Technology, 40,* 1052-1057.

[25] Zhang, S.-H., Akutsu, Y., Russell, L.M., Flagan, R.C., & Seinfeld, J.H. (1995). Radial Differential Mobility Analyzer. *Aerosol Science and Technology, 23,* 357-372.

Appendix B

Evaluation of an Electrical Aerosol Detector (EAD) for the Aerosol Integral Parameter Measurement

Lin Li[1], Da-Ren Chen[1] and Perng-Jy. Tsai[2]

[1]Department of Energy, Environmental & Chemical Engineering

Washington University in St. Louis

One Brookings Drive, Box 1180

St. Louis, Missouri 63130, U.S.A.

Email : chen@seas.wustl.edu

[2]Department of Environmental and Occupational Health, Medical College,

National Cheng Kung University

138 Sheng-Li Road, 70428, Tainan, Taiwan

Email: pjtsai@mail.ncku.edu.tw

Journal of Electrostatics

Abstract

The performance of an Electrical Aerosol Detector (EAD; TSI Model 3070A) was experimentally evaluated for measuring the integral parameters of particles (i.e., total length concentration of particles, and the total surface area concentrations of particles deposited in a human lung). The EAD consists of a unipolar diffusion charger with an ion-trap, and aerosol electrometer. We first evaluated the performance of the EAD charger. Both polydisperse and monodisperse particles of Ag, NaCl, and oleic acid (with the dielectric constants of infinite, 6.1 and 2.5) were then generated to evaluate the particle material effect on the EAD readout.

Key words: Electrical Aerosol Detector (EAD); Particle total length; Particle surface area; Material dependence; Unipolar charger evaluation

1. Introduction

Nanoparticles are encountered in many industrial systems utilizing aerosol reactors. Such reactors are used in industry to make a wide variety of particulate commodities, such as carbon black, pigments, and materials for high technology applications such as optical waveguides and powders for advanced ceramics [1]. Nanoparticles of different physical and chemical properties are synthesized through different methods for these new applications. A similar scenario is encountered in many other systems, where a large quantity of the so-called “undesirable” aerosols is produced. Biswas and Wu [2] cite as examples municipal waste incinerators, hazardous waste incinerators, welding systems, exhausts, coke ovens, smelters, nuclear reactor accidents, utility boilers, and the exhausts from automobile, diesel engine, and jet aircraft. As more studies reveal that nanoparticles may be associated with deleterious health effects [3-6], it will be necessary to monitor them in closed or ambient environments where workers or the public are potentially to be exposed. This leads to the increasing demand/need for a simple device capable of monitoring the integral parameters (i.e., total number, length, surface area concentration) of nanoparticle size distributions. Electrical aerosol detector (EAD) techniques are thus proposed for the above-mentioned tasks. A typical EAD consists of two key components: one for electrically charging aerosols and one that measures the current/charges on charged aerosols. The readout of an EAD strongly depends on the charging technique used.

The measurement of aerosol number concentration using EADs can be accomplished by imparting electronic charges to particles and measuring the resulting charges with an aerosol electrometer. Liu and Lee [7] used unipolar diffusion charging

and electrometer detection to measure the electrical charges on particles for aerosol concentration measurements. John [8] used contact electrification coupled with an aerosol electrometer for the monitoring of particulate matter. In general, the techniques can be used for precise concentration measurements only if the charging characteristics on particles are constant and measured aerosols have the same or very close size distributions. Further, ion interception by particles has been used by investigators to determine the number concentration and mean diameter of aerosol systems [9]. In this method, bipolar ions are produced by a ^{60}Co source in a cylindrical chamber. As particles passing through the chamber, the ions are intercepted, and the ion current is attenuated. The measurement of particle number concentration is then deduced through the comparison of the attenuated ion current to that from a parallel chamber in which all particles are filtered. The principle of monitoring ion attenuation due to the presence of aerosol has been applied to smoke detectors commonly installed in all the office buildings and residential houses [10].

The EAD technique had also been proposed to study the diameters of particles [11]. In an aerosol flame ionization detector, aerosol particles passing through a H_2 flame alter the dielectric properties of the flame region. With appropriate dilution, aerosol particles pass through the flame one by one, and the integrated response is simply related to the particle diameter for a given substance. However, the response of the aerosol flame ionization detector depends significantly upon the particle composition.

More recently, the EAD technique has been proposed to monitor the total length concentration of nanoparticles. Renewed interest in a simple integral parameter measurement of particles prompted the complete redesign and introduction of the Model

3070A Electrical Aerosol Detector (EAD). The EAD measures a unique aerosol parameter called total aerosol length concentration (mm/cm^3), which can be thought of as the product of the number concentration and average particle diameter, or simply as the first moment of particle size distribution (i.e., the integral of the size-weighted particle size distribution). Fig. 1 shows the schematic diagram of an EAD. Sampled particles are first passed through a small cyclone to remove particles with diameters larger than 1.0 μm. The sampled aerosol flow of 2.5 lpm is then split unequally: one portion of the flow (1.5 lpm) is directly introduced into the aerosol charging chamber and the other portion (1.0 lpm) is used as the carrier for unipolar ions, generated in the corona discharging region. The 1.0 lpm portion of the flow is first passed through HEPA and active carbon filters to remove particles and vapor contaminants in the stream, then serves as an ion carry flow. The two split flow streams are combined and mixed in the aerosol charging chamber. Particles exiting from the mixing chamber are passed through an ion-trap, with the voltage set at 20V to remove excess ions. The electrical charges carried by particles are measured in an aerosol electrometer of the Faraday cage type downstream of the ion-trap. The output of diffusion charger with ions provided by corona discharge in the EAD has a linear relationship between particle diameter and the number of elementary charge acquired by particles in the diameters ranging from 10 nm to 1 μm [12]. The overall EAD response, which includes internal particle losses, follows a nearly linear power law, with the net electrometer current proportional to the particle diameter raised to the 1.133 power [12].

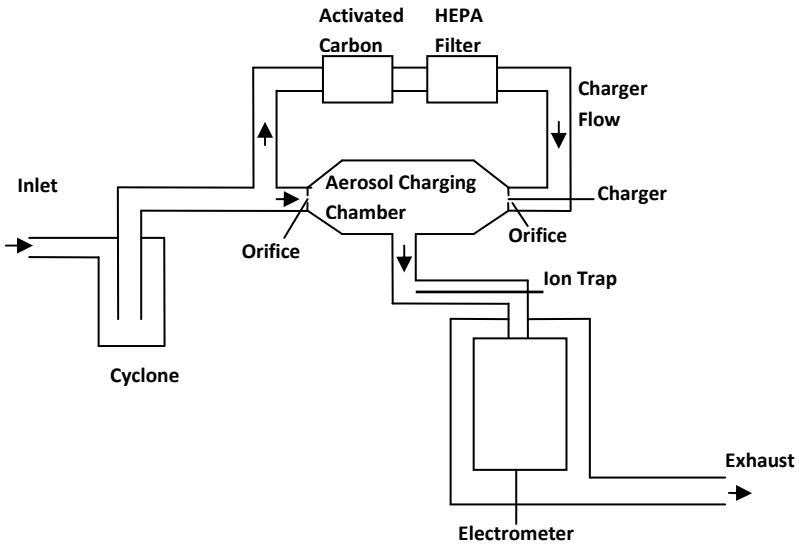

Figure 1 Schematic Diagram of the Electrical Aerosol Detector (EAD) under this study

For the surface area measurement of particles, an integrated system consisting of a condensation particle counter (CPC), mass concentration monitor (MCM), and electrical aerosol detector (EAD) were used to characterize the integral parameters (i.e., the total number, surface area, and mass concentration) of sampled particle size distributions [13]. Recent study using the integrated system and atmospheric field data has shown that the EAD readout can be a useful indicator of the surface area concentration of particles deposited in human lungs [14]. It has further been found that the response of the EAD with the ion-trap voltage at 100V correlates with the calculated surface area concentration of particles deposited in the tracheobronchial (TB) lung region, and that with an ion-trap voltage set of 200V correlates with that deposited in the alveolar (AL) region [15]. Based on this observation, the TSI Nanoparticle Surface Area Monitor (NSAM, Model 3550) has thus been made commercially available to measure the surface area concentration of nanoparticles deposited in the TB and AL regions of a

human lung by adjusting the ion-trap voltage of TSI 3070A EAD. A portable version of the NSAM (TSI Model 9000) is also available on the market.

Due to the unipolar diffusion charger used in the EAD, the concern of particle material dependence on the EAD readout has been raised [16, 17]. The electrical image force resulting from unipolar ions moving in the close proximity of particles plays an important role in the diffusion charging process. The dielectric constant effect on the resulting image force can be quantified by a factor of $(\frac{\kappa-1}{\kappa+1})$, where κ is the dielectric constant of the particle material. To investigate the effect of the particle material on the EAD readout, calibration factors (i.e., a constant to convert the EAD readout to the sampled particle surface area concentration) have been measured using monodisperse (Ag agglomerates and NaCl, 7 - 100 nm) and polydisperse particles (Ag agglomerates, number count mean diameter below 50 nm) [18]. No significant dependence of the calibration factors on particle material was concluded in the study. Both Ag and NaCl test particles used in the study mostly in the range less than 100 nm have relatively high dielectric constants: infinite and 6.1, resulting in the image force factor of 1 and 0.71, respectively. Furthermore, although the configuration and performance of the EAD charger have been studied previously [19], the flow rates used in this investigation are different. It is thus important to characterize the EAD aerosol charger under its current operational flow rate setting to understand the effect of particle material on the EAD readout in more detail.

In this work, we first measured the charging efficiency and charge distribution of particles after the EAD charger using monodisperse Polystyrene latex (PSL) and Ag particles (with the dielectric constants of 2.5 and infinite, respectively) in the diameter

range of 4 - 105 nm. We then evaluated the performance of the EAD with the ion-trap voltages set at 20, 100, and 200 V, using polydisperse and monodisperse particles of oleic acid, NaCl, and Ag (with the dielectric constants of 2.5, 6.1 and infinite, respectively) with the mean sizes ranging from 20 to 200 nm.

2. Experimental Evaluation of EAD Charger

2.1. Experimental Setup

To investigate the performance of the EAD charger, a custom-made adaptor was made to sample all particles downstream from the EAD ion-trap. In this experiment, no voltage was applied on the EAD ion-trap. The study to characterize the charger's performance consists of two parts: measuring charging efficiency and charge distribution of particles.

Two different techniques were used to generate test aerosols. The setups for two aerosol generation techniques are shown in Fig. 2. Polydisperse Ag particles with electrical mobility sizes ranging from 5 to 50 nm were generated by the evaporation-and-condensation technique [20]. In this setup, Ag powder was placed in a ceramic boat located in a high temperature tube furnace (CM Furnace 1730-20HT). Nitrogen at a rate of 2.0 lpm was the vapor carrier gas, passing through a tube placed in the furnace. The flow rate of the carrier gas was regulated and monitored by a needle valve and laminar flow meter prior to its introduction through the furnace tube. The powder material in the ceramic boat was evaporated at high temperature, and its vapor was carried out by the nitrogen gas flow. At the exit of the furnace tube, polydisperse nanoparticles were formed by mixing the vapor carrier gas with particle-free air at room temperature. To vary the

mean sizes of generated particles, the tube furnace temperature was varied from 1000 °C to 1200 °C for Ag particles. A constant-output, home-made atomizer was used to produce PSL particles with electrical mobility sizes from 85 to 105 nm. The flow rate output from the atomizer was 4.0 lpm when the pressure of compressed gas was at 30 psig. Droplets produced by the atomizer were passed through a Po^{210} radioactive neutralizer and silicon-gel diffusion dryer before they were used as test aerosols to remove the electrical charges and the solvent in droplets.

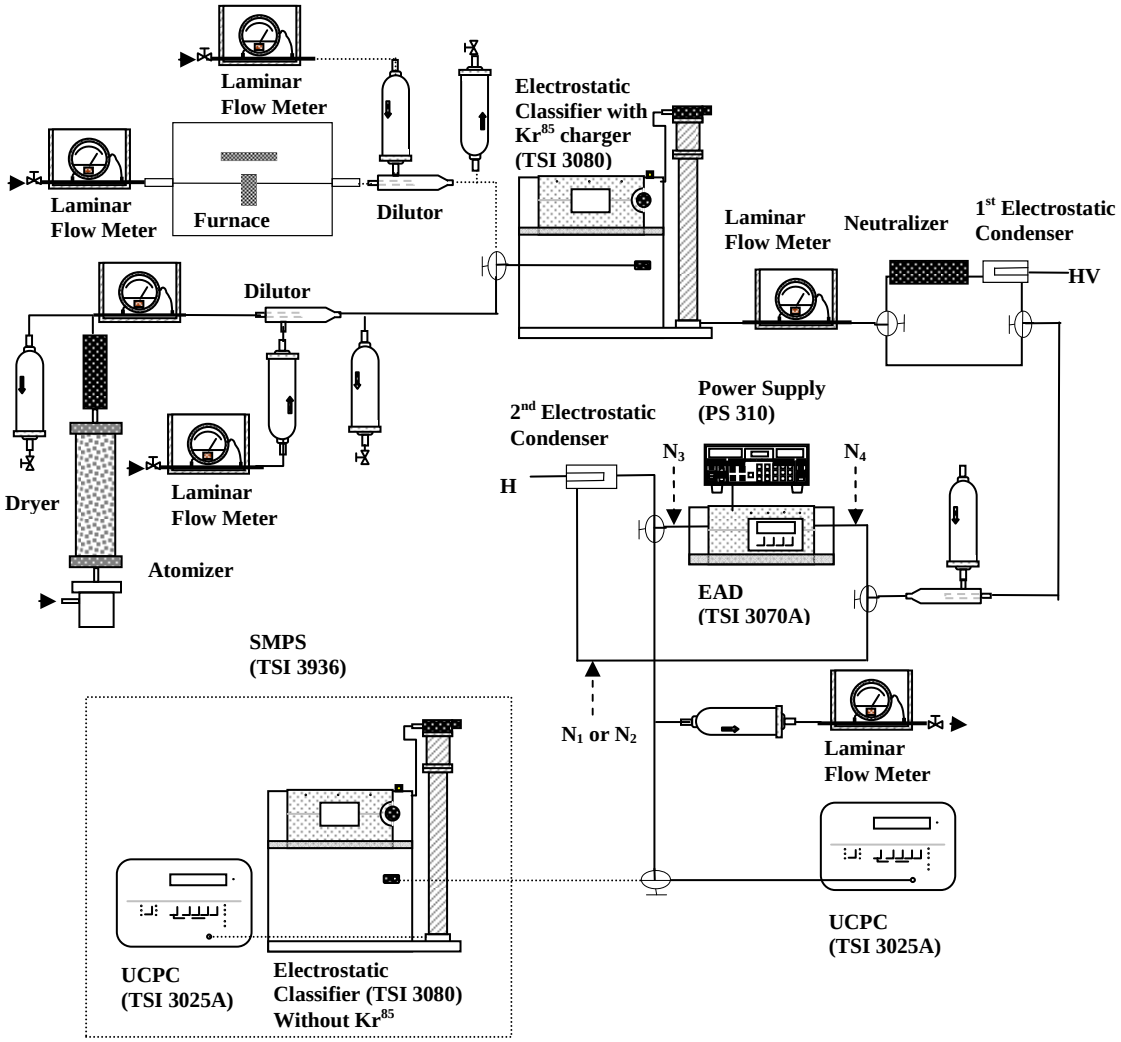

Figure 2 Diagram of the experimental setup for the performance evaluation of the unipolar diffusion charger used in the EAD

To produce monodisperse test particles, a differential mobility analyzer (DMA, TSI Model 3081) was used downstream of both polydisperse aerosol generation systems to classify the particles with desired diameters. Prior to their introduction to the DMA, generated particles were electrically charged in a Kr^{85} particle charger [21]. The DMA was operated at aerosol and sheath flow rates of 1.0 and 8.0 lpm, respectively. A Po^{210} radioactive neutralizer at the DMA monodisperse aerosol exit reduced the electrical charges on classified particles. Neutral test particles were needed for this part of the experiment. To remove all the charged particles in aerosol flow stream, an electrostatic condenser (EC) was installed at the exit of the aerosol neutralizer, located downstream of the DMA monodisperse aerosol exit.

For the extrinsic charging efficiency measurement, the charged fraction of particles exiting the EAD charger was measured. The task was accomplished by installing a 2^{nd} EC at the downstream of the EAD charger to remove the charged fraction of particles in the flowstream, and then measuring the number concentration of neutral particles after the 2^{nd} EC by an Ultrafine Condensation Particle Counter (UCPC, TSI model 3025A). For the charge distribution measurement, the particles leaving the EAD charger were directly sampled by a Scanning Mobility Particle Sizer (SMPS, TSI Model 3936) without the Kr^{85} neutralizer in place. The SMPS scanned the electrical mobility distribution of particles exiting the EAD charger, from which the particle charge distribution was obtained.

2.2 Calculation of EAD Charging Efficiencies

In this part of the experiment, the intrinsic charging efficiency was measured by the method used by Romay and Pui [22], calculated as

$$\eta_{in} = 1 - \frac{N_1}{N_2}, \quad (1)$$

where η_{in} is the intrinsic charging efficiency, and N_1 is the particle number concentration measured with both the charger and EC on, whereas N_2 is measured with both the charger and EC off. The extrinsic charging efficiency was evaluated by the method described by Chen and Pui [23], defined as

$$\eta_{ex} = \frac{(N_3 - N_1 / P_{ec})Q_t}{N_4 Q_{in}}. \quad (2)$$

Here η_{ex} is the extrinsic charging efficiency; N_3 the number concentration of particles exiting the EAD charger when the EAD charger is on; N_4 the number concentration of particles entering the charger; P_{ec} the penetration of neutral particles through the 2nd EC. The total volumetric flow rate exiting the EAD charger Q_t and the volumetric flow rate of aerosol entering the mixing chamber in the EAD charger Q_{in} relates to Q_t as

$$Q_t = Q_{in} + Q_i, \quad (3)$$

where Q_i is the volumetric flow rate of the ion carrier gas.

2.3 Results on the Performance of EAD Diffusion Charger

To study the performance of the EAD charger, we measured the intrinsic and extrinsic charging efficiencies as well as charge distributions of particles exiting from the EAD diffusion charger using monodisperse Ag particles in the size range of 5 - 50 nm and PSL particles in the size range of 85 - 105 nm. Fig. 3 shows the intrinsic and extrinsic charging efficiencies for the EAD diffusion charger operated at the designed flow rates

(i.e., 1.5 lpm aerosol and 2.5 lpm total flow rates). As expected, the intrinsic charging efficiency curve is higher than the extrinsic efficiency, because of the loss of particles in the EAD unipolar charger as they become electrically charged. The intrinsic charging efficiency is higher than 95% for particle sizes larger than 40 nm. For sizes less than 40 nm, the charging efficiency decreases as the particle size decreases. The extrinsic charging efficiency remains constant at 90% for particle sizes larger than 50 nm. The extrinsic charging efficiency decreases with particle diameter below 50 nm.

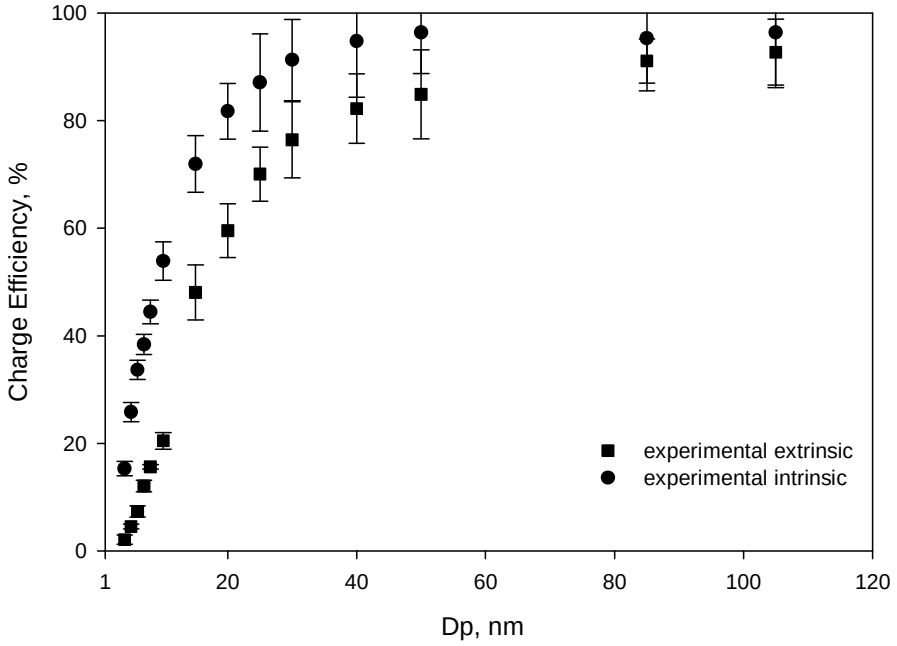

Figure 3 Measured intrinsic and extrinsic charging efficiencies for the unipolar EAD charger used in the EAD. Monodisperse PSL and Ag particles were used in the experiment

Fig. 4 shows the measured charge distributions of Ag particles in the size range of 15 - 50 nm, and of PSL particles in the range of 85 - 105 nm. It was found that for

particles less than 20 nm in diameter, the electrical charge on particles exiting the EAD charger is mostly single. The mean electrical charge on the charge distribution increases as the particle size increases. If there is obvious material dependence, the charge distribution of PSL particle with large size might be very close or equal to that of Ag particle with small size. In our case, particle charge distribution smoothly transit toward the multiple charges direction from Ag to PSL when increasing particle size. Therefore, the smooth transition between Ag and PSL particles on both charging efficiency curves and charge distribution implicitly indicates minor particle material dependence on the EAD readout for the case of monodisperse particle testing.

(a)

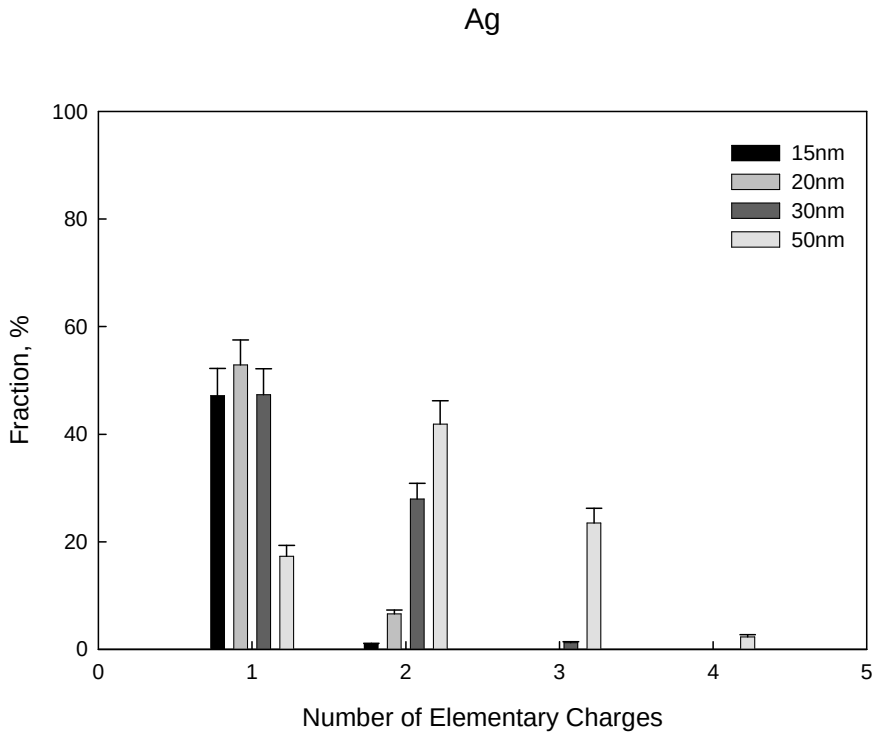

(b) PSL

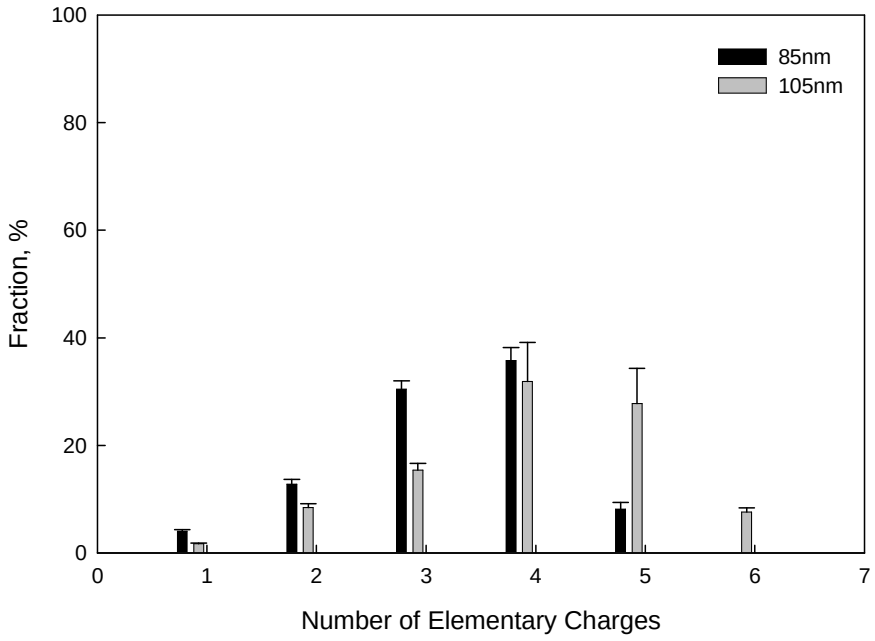

Figure 4 Measured charge distribution of particles exiting the EAD unipolar diffusion charger: (a) Ag particles and (b) PSL particles

3. Evaluation of EAD for the Aerosol Integral Parameter Measurements

3.1 Experimental Setups for Material Dependence Testing

Fig. 5 shows a schematic of the experimental setup to evaluate the particle material effect on the EAD readout. The particle-generation systems are the same as described in the section 2.1. For particles with electrical mobility sizes ranging from 20 to 40nm, the high temperature tube furnace was used to produce polydisperse Ag and NaCl particles. To vary the mean sizes of generated particles, the tube furnace temperature was varied from 1000 °C to 1200 °C for Ag particles, and 650 °C to 750 °C for NaCl particles. For particles with electrical mobility sizes ranging from 80 to 200nm, a constant-output, home-made atomizer was used to produce polydisperse NaCl and oleic

acid particles. The mean sizes of test particles were varied by changing the solutions of NaCl or oleic acid volume concentration from 0.01% to 1%.

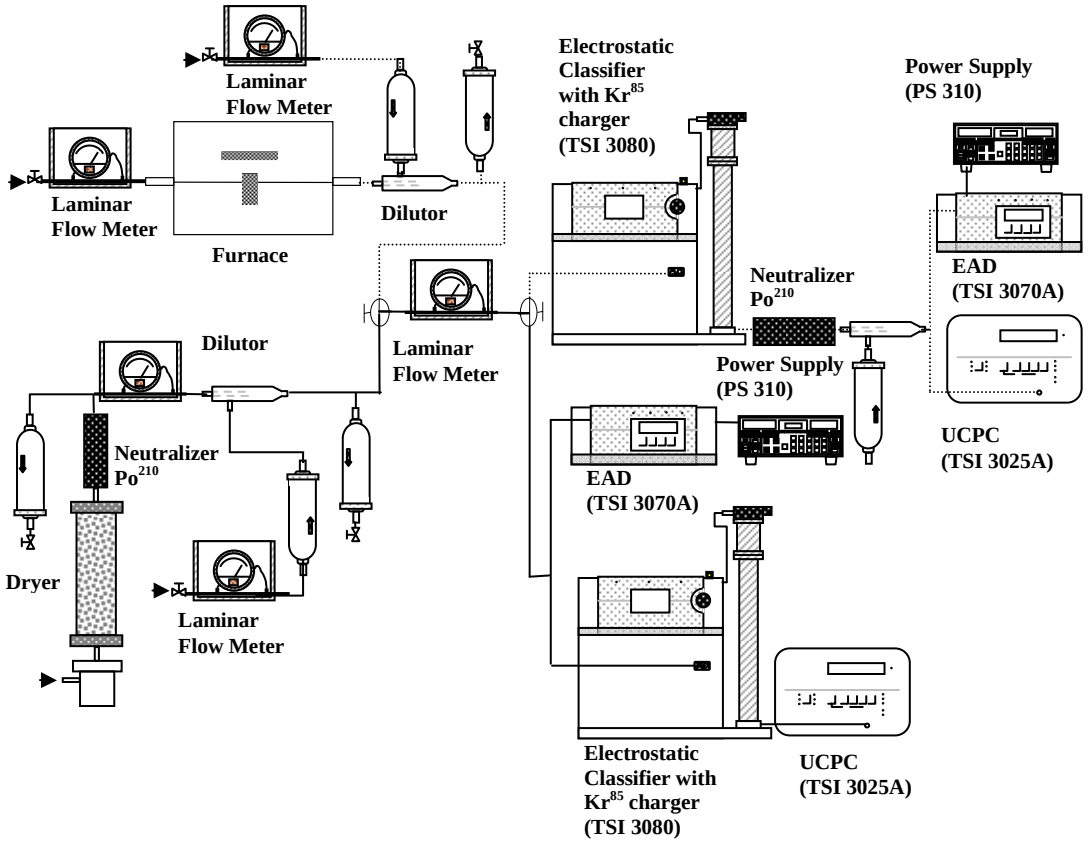

Figure 5 Schematic diagram of the experimental setup for the performance evaluation of EAD

Different experimental arrangements were used to evaluate the EAD's performance with monodisperse and polydisperse particles. For the monodisperse particle testing, particles were simultaneously introduced to both a UCPC and the EAD (TSI model 3070A). The particle number concentration and electrometer current were simultaneously measured from the UCPC and EAD for all experiments using Ag, NaCl, and oleic acid particles. For the polydisperse particle testing, challenge particles were

simultaneously introduced to the EAD and a SMPS (TSI Model 3936) to measure particle size distributions after passing through a dilutor. In both testing cases, the concentration of test aerosol was varied in the aerosol dilutor.

3.2 Data Analysis

3.2.1 Calculation of average electrical charges on individual particles

For monodisperse particle testing, the concentration of test particles was measured by a UCPC, while the electrical current of the charged test particles was measured by the EAD. The average charge q_{avg} on the test particles was thus calculated as

$$q_{avg} = \frac{I}{N(d_p)eQ_{in}}, \quad (4)$$

where I is the charged particle current measured by EAD; $N(d_p)$ is the particle concentration measured by the UCPC; and e is the charge on an electron e, $1.6*10^{-19}$C.

3.2.2 Calculation of the total particle length concentration

For the polydisperse testing, the size distributions of test particles were measured by SMPS and fit to a log-normal distribution, while the electrical current of the charged test particles were measured by the EAD. The total particle length concentration (L) is calculated by

$$L = \sum_{i=1}^{n} N_i(d_p)d_{p,i} \quad (5)$$

where $N(d_p)$ is the number of particles in each size bin of the distribution, measured by SMPS; and n the number of size bins used in each particle size distribution.

3.2.3 Calculation of the surface area concentration of particles deposited in the TB and AL lung regions

Fig. 6 shows the deposition curves for tracheobronchial (TB) and alveolar (AL) deposition in a typical human lung. The deposition curves were obtained using the UK National Radiological Protection Board's (NRPB's) LUDEP Software [24], based on the recommendations of ICRP Publication 66 [25]. The breathing and lung conditions of a reference worker were used in the calculation are selected as the follows [15]:

- Breathing type: nose only
- Functional lung residual capacity: 3301 cc
- Breathing rate (Breath/min): 20
- Ventilation rate: 1.5 m^3/hr
- Activity level: light exercise.

Using the particle size distribution measured by SMPS and the particle lung deposition curves, the surface area concentration of particles deposited in different regions of a human lung (DS) is calculated by

$$DS = \sum_{i=1}^{n} N_i(d_p)\pi d_{p,i}^2 \eta_i(d_p) \quad (6)$$

where $\eta(d_p)$ is the particle lung deposition efficiency in the TB or AL region of a human lung. The SMPS particle size distributions were fit by the log-normal distribution prior to the calculation using Eq. (6).

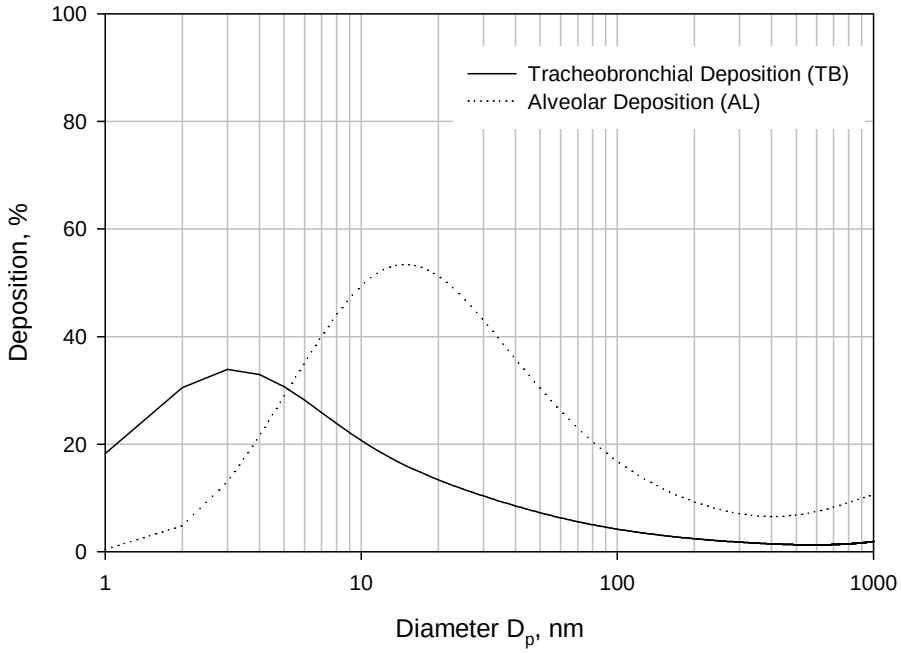

Figure 6 Calculated particle deposition curves as a function of particle size for the tracheobronchial (TB) and alveolar (AL) regions of a human lung (based on the model given in ICRP, 1994)

3.3 Results and Discussion

3.3.1 Average charges on particles

Fig. 7 shows the average electrical charges on Ag, NaCl, and oleic acid particles as a function of particle size with the ion-trap voltages set at 20, 100 and 200 V, respectively. The EAD readout was typically below 1 pA for the cases of monodisperse Ag and NaCl particles with the sizes ranging from 20 to 50 nm and the number concentrations ranging from $4*10^3$ to $9*10^4$ #/cm^3, as well as monodisperse NaCl and oleic acid particles with the diameters of 80 - 200 nm and the concentrations from $4*10^3$ to $6*10^4$ #/cm^3. Near linear relationships between the particle average charge and particle

size are observed for all the test ion-trap voltage settings. Particles with a high dielectric constant have slightly more average electric charges for the same particle size. Although the combination coefficient between neutral particles and ions significantly depends on the dielectric constant of particles [26], it is thus believed that the effect on the EAD readout is considered minor but detectable in the cases of particles acquiring multiple charges.

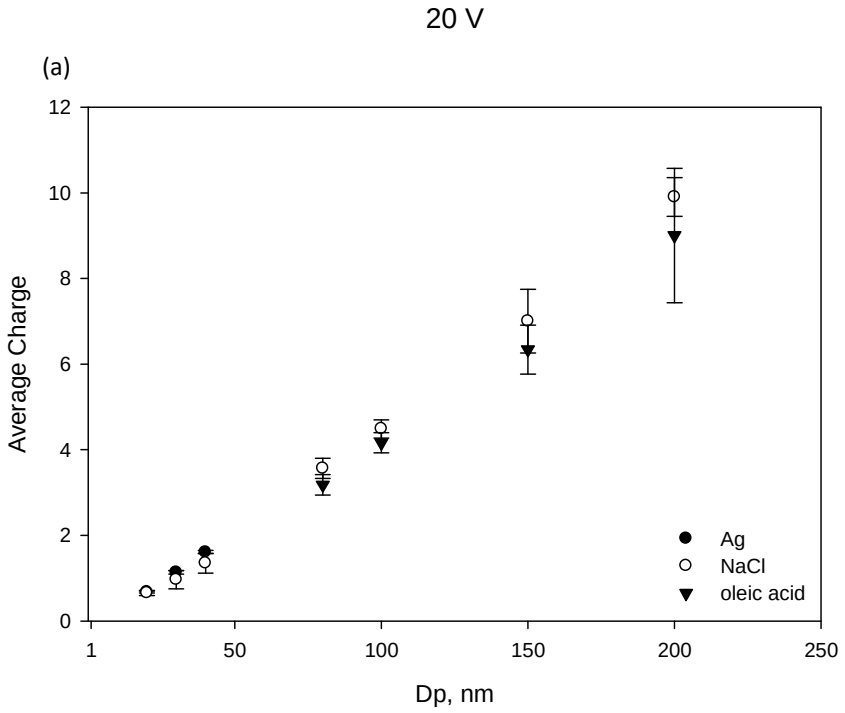

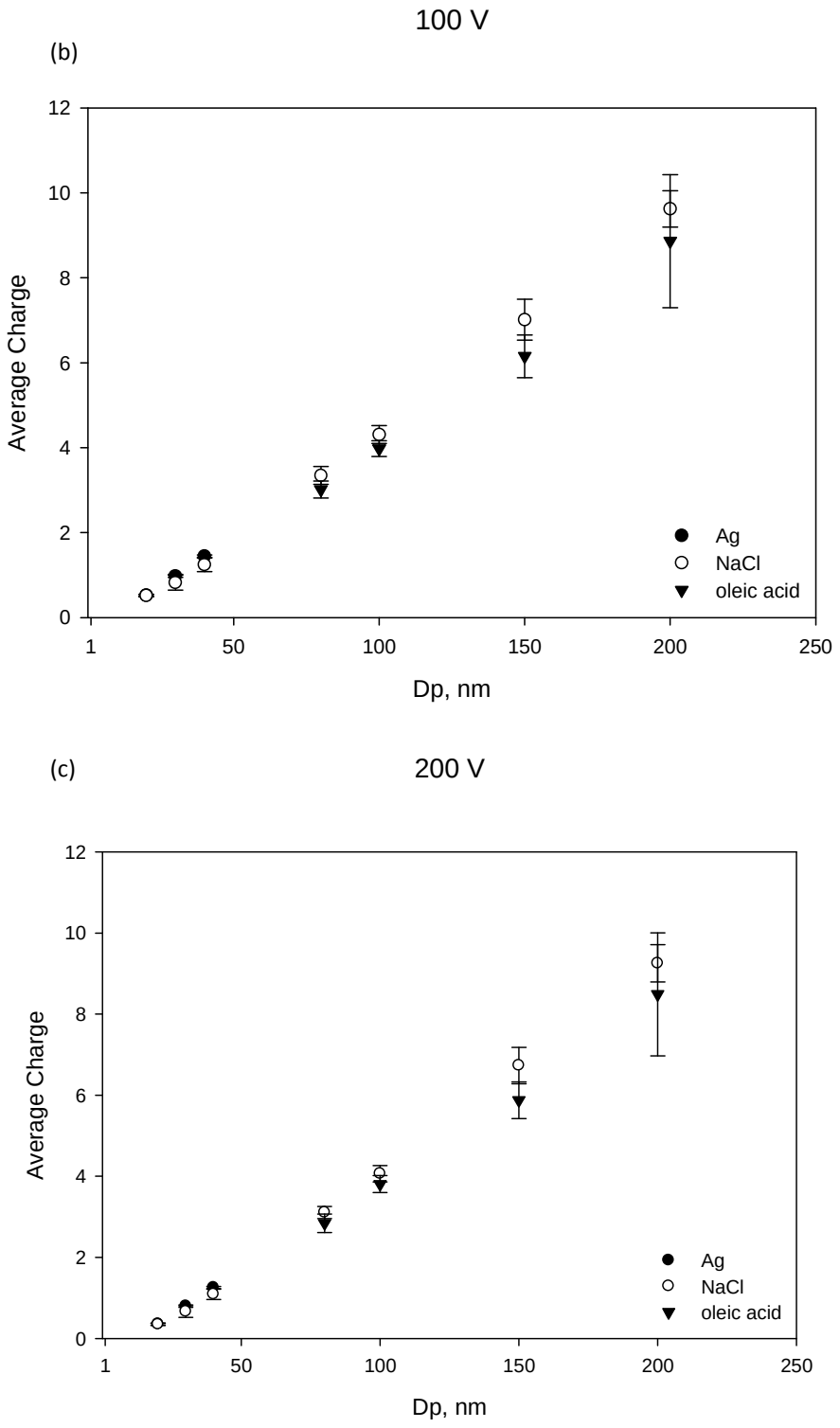

Figure 7 Measured average charges on monodisperse Ag, NaCl, and oleic acidparticles when the EAD ion-trap voltages were set at (a) 20V; (b) 100V; and (3) 200V

Based on the near linear relationship between particle average charge and particle size, it is not surprising that the EAD readout is proportional to the total length concentration of sampled particles. In fact, the readout of an EAD test can be correlated to any integral variables if the variables are linearly proportional to the particle size. As an example, Fig. 8 shows the curves of the surface area of a particle deposited in the TB and AL region of a human lung as a function of particle size. The curves were created based on ICRP lung model [25]. There is a near linear relationship between the particle surface area and particle size in the range from 10 to 400 nm. Based on this observation, the EAD readout can be correlated to the surface area concentration of particles deposited in TB and AL regions of a human lung for particle diameter in the range of 10 - 400 nm. Therefore, with the proper calibration, the EAD readout can be used as an indicator of surface area concentration of particles deposited in TB and AL regions. Note that the curve of deposited particle surface area may not be linearly proportional to the particle size due to, for example, the hygroscopic property of particles. The size of hydrophilic particles entering a human lung will increase, typically in high relative humidity, resulting in increased particle deposition. The traditional ICRP deposition curve may be altered and become non-linear in the entire size range. In such cases it will be hard to correlate the EAD readout to the surface area concentration of particles deposited in a human lung.

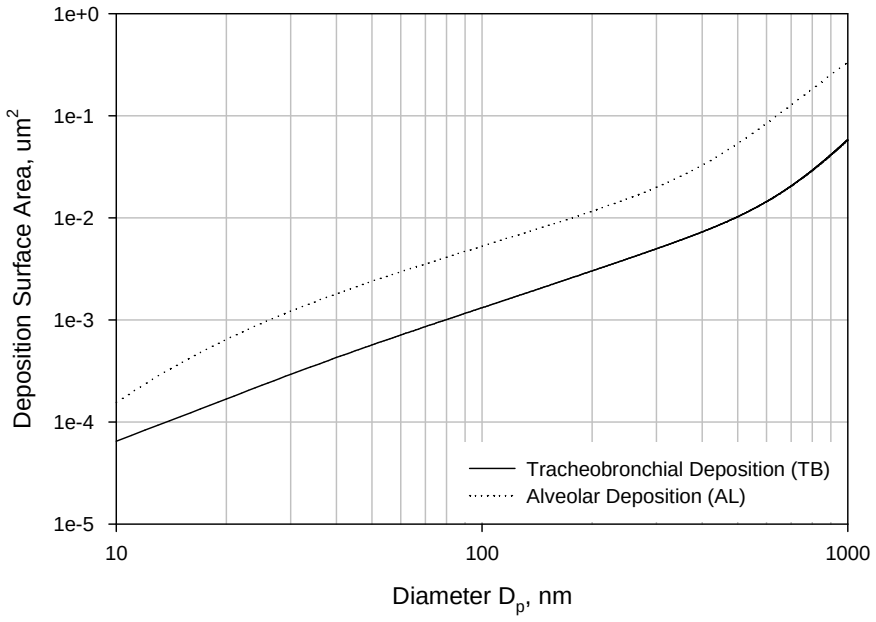

Figure 8 Calculated surface area of particles deposited in the tracheobronchial (TB) and alveolar (AL) regions of a human lung. The data was derived from the curves given in Figure 6

3.2.2 Effect of particle material

Polydisperse Ag, NaCl, and oleic acid particles were used to test the EAD performance at high concentration (i.e., up to 50 pA of an EAD readout; compared with up-to-1-pA EAD readout in monodisperse particle testing). Fig. 9 shows the correlation curves between the calculated total particle length and EAD readouts for polydisperse Ag, NaCl, and oleic acid particles with the ion-trap voltage set at 20 V. For Ag and NaCl particles generated by the furnace, the particle mean sizes, number concentrations, and geometrical standard deviations range from 20 to 50 nm, from $3*10^5$ to $9*10^6$ #/cm^3, and from 1.5 to 1.6, respectively. For the cases of NaCl and oleic acid particles generated by atomizer, the particle mean sizes, number concentrations, and geometrical standard

deviations are ranging from 80 to 200 nm, from $2*10^5$ to $5*10^6$ #/cm^3, and from 1.65 to 1.8, respectively. The linear relationship between the EAD reading and the calculated total particle length are evident in all the curves. Linear regression analysis was applied to identify the slopes of all the curves. It was found that in general the slopes of the correlation curves decrease with the increase in particle dielectric constant. The minor particle material dependence observed in monodisperse particle testing is amplified herein by the compound effect of particle material and polydispersity in this testing. For the correlation curves at 20V ion-trap voltage (shown in Fig.9a), the variation of line slopes is about 15% when changing the dielectric constant of the particles' material from 2.5 to infinite. It is important to notice that the slope difference between the cases of NaCl and Ag particles is in fact negligible. The slope variation of the correlation lines at 20V ion-trap voltage between the cases of NaCl and Ag particles is about 3%. The observation of the negligible material dependence on the correlation curves for NaCl and Ag particles agrees with what reported by Shin et al. [18]. The most prominent difference in the correlation line slope occurs between the cases of NaCl and oleic acid particles.

Figs. 9b and 9c show the correlation curves between the calculated surface area concentration of particles deposited in the TB and AL lung regions and EAD readouts for polydisperse Ag, NaCl, and oleic acid particles with the EAD ion-trap voltage set at 100 and 200 V. The general trends of correlation curves for deposited particle surface area testing are the same as those for the cases of total particle length testing. The slope of the correlation line decreases with an increase in particle dielectric constant. The variation of the line slopes for TB and AL correlation curves are about 13% and 5%, respectively, which is less than that observed in the case of total particle length testing. Based on the

experiment evaluating the EAD charger, particles with high dielectric constant acquire more charges in the EAD charger; however, the consequent loss of charged particles in the ion-trap dwarfs the particle material effect. This offsetting loss is reflected in the observation that the particle material effect on the EAD readout is less detectable at higher ion-trap voltage in the cases of monodisperse and polydisperse particle testing.

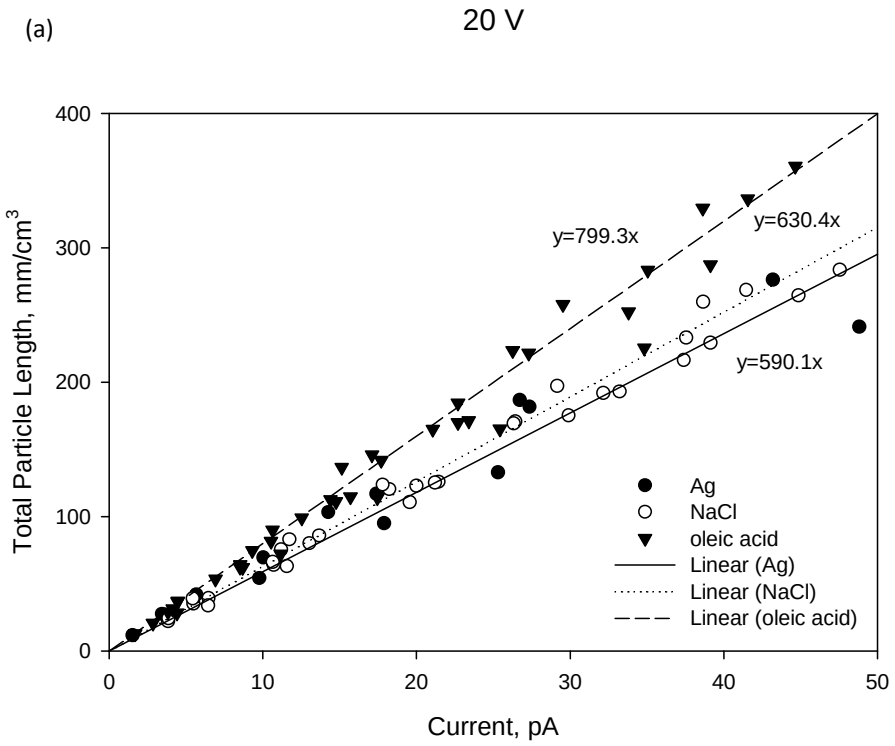

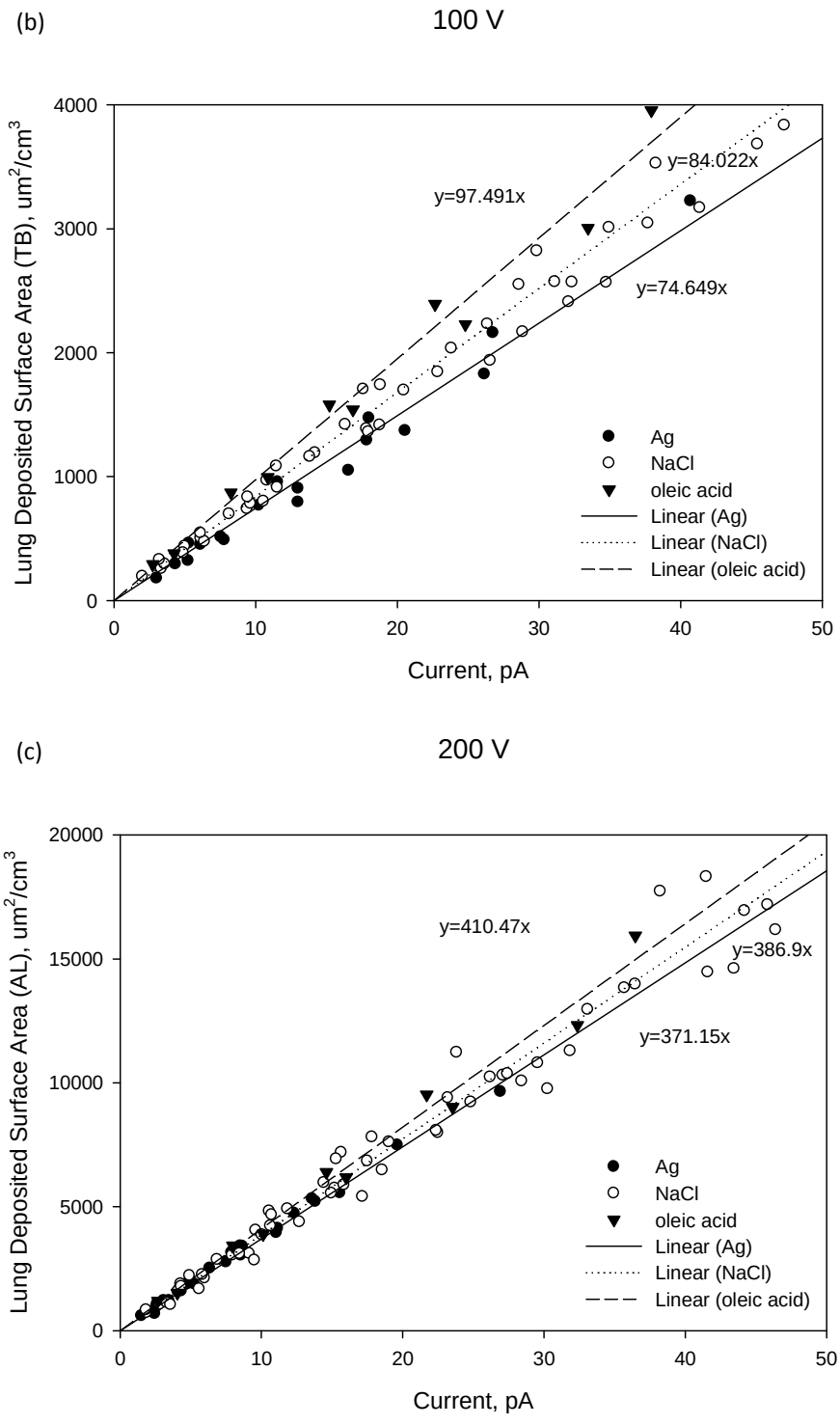

Figure 9 EAD Correlation curves (a) between the calculated total particle length and EAD readouts with 20V ion-trap voltage; (b) between the calculated particle deposited surface area in TB region and EAD current readouts with 100V ion-

trap voltages; and (c) between the calculated particle deposited surface area in AL region and EAD readout with 200V ion-trap voltage. The data were obtained by using polydisperse oleic acid, NaCl and Ag particles with the dielectric constants of 2.5, 6.1 and infinite, respectively.

4 Conclusion

In summary we have characterized the intrinsic and extrinsic charging efficiencies, and charge distribution of particles for the unipolar diffusion charger used in the studied EAD. The charger characterization was done by using monodisperse PSL and Ag particles with the dielectric constants of 2.5 and infinite, respectively. Both the intrinsic and extrinsic charging efficiencies decrease as the particle size decreases. The intrinsic charging efficiency was higher than 95% for particles in the diameters larger than 40 nm. The extrinsic charging efficiency remains constant at 90% for particle sizes larger than 50 nm. At the exit of the EAD charger, the charge distribution measurement indicates that, the number of electrical charges on particles with the diameters less than 20 nm is mostly single.

We have evaluated the performance of the EAD with the ion-trap voltage settings at 20, 100, and 200 V. Polydisperse and monodisperse particles of Ag, NaCl, and oleic acid (with the dielectric constants of infinite, 6.1 and 2.5, respectively) were generated and used as test aerosols. For the mean electrical charges on Ag, NaCl, and oleic acid particles, a nearly linear relationship between the average electrical charges on particles and particle size was observed. As expected, particles with high dielectric constant acquire more electrical charges than those with low dielectric constant for the same

particle size. In spite of the fact that the combination coefficient between neutral particles and ions is a strong function of particle material from the aerosol charging theory, the particle material effect on the diffusion charging process is considered minor but measureable when particles acquire multiple charges. The main reason might be that the $N_i t$ (N_i: ion concentration; t: residence time) value is too large to make the combination coefficient less important in the process. Physically, there are so many ions that particle material is less dependent in the combination of ions and particles.

Correlation curves for the calculated total particle length and deposited particle surface area concentrations v.s. the EAD readout at different ion-trap voltages were obtained for different polydisperse test particles. In general, the correlation curves are linear in all the test conditions. The EAD readout can thus be used to correlate any integral parameter that varies linearly with particle size (i.e., total particle length and surface area of particles deposited in TB and AL regions of a human lung). For the correlation curves between the EAD readout at 20V ion-trap voltage and the calculated total particle length, the correlation line slopes vary about around 15%, when varying the dielectric constant of particle material from 2.5 to infinite. The most significant difference in correlation line slopes occurs between the cases of NaCl and oleic acid particles (with the dielectric constants of 6.1 and 2.5, respectively). The correlation line slope difference between the cases of NaCl and Ag particles is in fact negligible. For the correlation between the EAD readout and the calculated particle surface area concentration deposited in TB and AL regions, the variation of line slopes are about 13% and 5%, respectively, when varying the dielectric constant of the particles' material from

2.5 to infinite. The dielectric constant effect on EAD readouts is less detectable with the increase of ion-trap voltage.

References

[1] P. Stamatakis, C.A. Natalie, Research needs in aerosol processing, Aerosol Sci. Technol. 14 (1991) 316-321.

[2] P. Biswas, C.Y. Wu, Control of toxic metal emissions from combustors using sorbents: a review, J. Air Waste Manage. Assoc. 48 (1998) 113-127.

[3] D. B. Warheit, Nanoparticles: health impacts, Materials Today. 7 (2004):32-35.

[4] G. Oberdörster, E. Oberdörster, J. Oberdörster, Nanotoxicology: an emerging discipline evolving from studies of ultrafine particles, Environ. Health Perspect. 113 (2005) 823-839.

[5] G. Oberdörster, V. Stone, K. Donaldson, Toxicology of nanoparticles: a historical perspective, Nanotoxicology. 1 (2007) 2-25.

[6] G.K. Wolfgang, S.-B. Manuela, M. Winfried, Health implications of nanoparticles, J. Nanoparticle Res. 5 (2006) 543-562.

[7] B.Y.H. Liu, K.W. Lee, An aerosol generator of high stability, American Industrial Hygiene Association Journal. 36 (1975) 861-865.

[8] W. John, Contact electrification applied to particulate matter-monitoring, in: B.Y.H. Liu (Eds.), Fine Particles, Academic Press INC., New York, 1976, pp. 649-667.

[9] V.A. Mohnen, P. Holtz, The SUNY-ASRC aerosol detector, J.A.P.C.A. 18 (1968) 667-668.

[10] F.N. Simon, G.G. Rock, Ionization-type smoke detectors, Rev. Sci. Instrum. 47 (1976) 74-80.

[11] L.L. Altpeter, J.S. Herman, J.P. Pilney, A.J. Senechal, D.L. Overland, Performance of flame ionization detector as atmospheric aerosol monitor, Envir. Sci. Technol. 10 (1976) 997-1002

[12] S.L. Kaufman, A. Medved, A. Pöcher, N. Hill, R. Caldow, F.R. Quant, An electrical aerosol detector based on the corona-jet charger, Poster PI2-07, Abstracts of 2002 AAAR, Charlotte, NC, (2002) 223.

[13] K.-S. Woo, D.-R. Chen, D.Y.H. Pui, W.E. Wilson, Use of continuous measurements of integral aerosol parameters to estimate particle surface area, Aerosol Sci. Technol. 34 (2001) 57-65.

[14] W.E. Wilson, H.-S. Han, J. Stanek, J. Turner, D.-R. Chen, D.Y.H. Pui, Use of electrical aerosol detector as an indicator for the total particle surface area deposited in the lung, Symposium on air quality measurement methods and technology sponsored by Air and Waste Management Association. Research Triangle Park, NC, (2004) Paper #37.

[15] H. Fissan, A. Trampe, S. Neunman, D.Y.H. Pui, W.G. Shin, Rationale and principle of an instrument measuring lung deposition area, J. Nanoparticle Res. 9 (2007) 53-59.

[16] J.R. Brock, M.-S. Wu, Unipolar diffusion charging of aerosols and the image force, J. Colloid Interface Sci. 33 (1970) 473-474.

[17] W.H. Marlow, J.R. Brock, Unipolar charging of small aerosol paticles, J. Colloid Interface Sci. 50 (1975) 32-38.

[18] W.G. Shin, D.Y.H. Pui, H. Fissan, S. Neumann, A. Trampe, Calibration and numerical simulation of nanoparticle surface area monitor (TSI Model 3550 NSAM), J. Nanoparticle Res. 9 (2007) 61–69.
[19] Medved, F. Dorman, S.L. Kaufman, A. Pöcher, A new corona-based charger for aerosol particles, J. Aerosol Sci. 31 (2000) S616-S617.
[20] H.G. Scheibel, J. Porstendorfer, Generation of monodisperse Ag and NaCl aerosol with particle diameters between 2 and 300 nm, J. Aerosol Sci. 14 (1983) 113-126.
[21] E.O. Knutson, K.T. Whitby, Aerosol classification by electric mobility: apparatus, theory, and applications, J. Aerosol Sci. 6 (1975) 443-451.
[22] F.J. Romay, D.Y.H. Pui, On the combination coefficient of positive ions with ultrafine neutral particles in the transition and free-molecule regime, Aerosol Sci. Technol. 17 (1992) 134-147.
[23] D.-R. Chen, Pui, D.Y.H. A high efficiency, high throughput unipolar aerosol charger for nanoparticles, J. Nanoparticle Res. 1 (1999) 115-126.
[24] A.C. James, M.R. Bailey, M.-D. Dorrian, LUDEP Software, Version 2.07: Program for implementing ICRP-66 Respiratory tract model, RPB, Chilton, Didcot, OXON. OX11 ORQ UK, 2000.
[25] ICRP (International Commission on Radiological Protection). Human respiratory tract model for radiological protection. ICRP Publication 66. Pergamon Press, Oxford, England, 1994.
[26] N.A. Fuchs, On the stationary charge distribution on aerosol particles in a bipolar ionic atmosphere, Geophys. Pura Appl. 56 (1963) 185-193.

Appendix C

Use of an Electrical Aerosol Detector (EAD) for Nanoparticle Size Distribution Measurement

Lin Li[1], Da-Ren Chen[1] and Perng-Jy. Tsai[2]

[1]*Department of Energy, Environmental & Chemical Engineering, Washington University in St. Louis, One Brookings Drive, Box 1180, St. Louis, Missouri 63130, U.S.A.*

[2]*Department of Environmental and Occupational Health, Medical College, National Cheng Kung University, 138 Sheng-Li Road, 70428, Tainan, Taiwan*

Journal of Nanoparticle Research

Abstract

Recently, Nanoparticle Surface Area Monitor (NSAM, TSI model 3550) and EAD (EAD, TSI Model 3070A) have been commercially available to measure the integral parameters (i.e., total particle surface area and total particle length) of nanoparticles. By comparison, the configuration of the EAD or NSAM is similar to that of electrical mobility analyzer of the early generation for particle size distribution measurement. It is therefore possible to use the EAD or NSAM as a particle sizer. To realize the objective of using the EAD as a sizer, we characterized the average electrical charges of monodisperse particles passing through the EAD particle charger and ion trap set at voltages ranging from 20 to 2500 V. The average charge data collected at different ion-trap voltages were then summarized by the empirical correlation using the parameter of $Zp*V$, where Zp is the particle electrical mobility and V is the ion-trap voltage. A data-reduction scheme was further proposed to retrieve the size distribution of sampled particles from the EAD readout at different ion-trap voltages. In the scheme, the functional format of each mode in a number size distribution of particles was assumed as log-normal, but the number of modes in an entire size distribution is not limited. A criterion was used to best fit the simulated EAD readouts with experimental ones by varying the count median diameter (CMD), geometric standard deviation (σg), and total particle number (Nt) of each mode in a particle size distribution. Experiments were performed to verify the proposed scheme.

Key words: Nanoparticle sizer, Electrical aerosol detector (EAD), Nanoparticle surface area monitor (NSAM), EAD unipolar charger

Introduction

Two types of instruments are currently available for measuring of physical properties of aerosol. One type measures the integral moments of the size distributions of particles to be investigated. Examples of such devices include the QCM (Quartz Crystal Microbalance) or TEOM (Tapered Element Oscillating Microbalance) for measuring particle mass concentration (Martin et al. 1991; Patashnick and Rupprecht 1991); NSAM (Nanoparticle Surface Area Monitor) for measuring the surface area concentration of particles deposited in human lungs (Fissan et al. 2007), and the CPC (Condensation Particle Counter) for detecting particle number concentration (Stoltzenburg and McMurry 1991). The other type of aerosol instrument measures particle size distribution. The particle size distribution instruments offer more detailed insight into the particles to be sampled. Particle size distributions are often necessary to study particle behaviors in different environments, to identify potential particle sources, and to interpret the data collected by integral-moment-type aerosol instruments. Examples of particle-size distribution-type aerosol instruments are the Scanning Mobility Particle Sizer (SMPS), Electrostatic Low Pressure Impactor (ELPI), and Optical Particle Counter (OPC).

To measure the size distribution of particles, instruments based on the particle electrical mobility technique are more suitable for particles in the submicron and nanometer diameter ranges. The technique requires sampled particles to be electrically charged prior to their introduction to an electrical classifier. In the classifier the particle size distribution can be altered by the presence of an electrical field in the device. The concentration of particles after passing through the classifier is then counted by an aerosol concentration detector (i.e., CPC or aerosol electrometer). The size distribution of

sampled particles can be reconstructed from the counter readouts collected at different electrical field strengths in the classifier (Knutson and Whitby 1975). The Electrical Aerosol Analyzer (EAA) and SMPS are examples of aerosol instruments using this technique. Both instruments are however designed for scientific research, and they are larger and more expensive, respectively, than devices used for industrial hygiene and exposure studies.

For industrial hygiene and epidemiologic studies, two assessment approaches can be used to determine the particle exposure level of workers: personal and site sampling. The site sampling is performed by using manual sampling devices and offline analyzing collected samples, and/or by real-time particle analysis devices. The latter are always preferred in modern studies, because the quick response of devices makes feasible the collection of time-dependent data. Many real-time aerosol mass monitors used in the workplace are based on a particle light scattering technique; photometers and laser particle counters are examples. The techniques used in photometers are generally insensitive for particles with diameters smaller than 100 nm (Hinds 1999). Optical instruments that size individual particles and convert the measured number size distribution to the mass distribution (i.e., laser particle counters, LPCs) are similarly limited to particles larger than 100 nm in diameter. Other real-time monitors using the vibration techniques, i.e., Quartz crystal microbalance (QCM) and Tapered element osscilation microscope (TEOM), are typically limited for measuring particle mass concentration in the level higher than 1 $\mu g/cm^3$, making them difficult in measuring the mass concentration of nanoparticles (except at high particle concentration). The SMPS is widely used as a research tool for characterizing submicron-sized aerosols, although its

applicability for use in the workplace is limited by the size and cost of the instrument, and its inclusion of a radioactive source as the particle charger. The Electrical Low Pressure Impactor (ELPI) is an alternative instrument that combines a cascade impactor with real-time aerosol charge measurements to measure size distributions (Keskinen et al. 1992). The low size resolution and expensive cost of the ELPI again make its use difficult in industrial hygiene studies. Thus, there is a need to develop a low-cost and portable device capable of measuring of size distributions of particles in the submicron and nanometer range.

As indicated by recent works (Oberdörster et al. 1996, 2005; Donaldson et al. 1998) the surface area concentration seems to be a good metric for the toxicity of particles in the submicron and nanometer size range, which leads to the development of instruments capable of measuring the surface area concentration of particles. A system integrating a condensation particle counter (CPC), mass concentration monitor (MCM), and electrical aerosol detector (EAD) has been used to infer the aerosol size distribution having a lognormal distribution functional format (Woo et al. 2001). The methodology works well for measuring the surface area of particles in the ambient environment. Given the lung deposition curves for a typical worker, the surface area concentration of particles deposited in human lungs is then obtained from calculation. In the course of field testing the integrated system for particle surface area concentration, it has been found that the response function curve of the EAD of the latest version (to be described in the next paragraph) correlates well with the area concentration of particles deposited in the tracheobronchial (TB) and alveolar (AL) regions of a human lung (Wlison et al. 2004). A later study by Fissan et al. (2007) found that the correlation curve of the EAD signal v.s.

the area concentration of particles deposited in the human lung can be established by setting the ion-trap voltage at 100 V for particles deposited in the TB lung region and by setting the ion-trap voltage at 200 V for particles in the AL region. Based on Fissan et al. (2007), the TSI Nanoparticle Surface Area Monitor (NSAM, Model 3550) has been commercially introduced to measure the surface area concentration of nanoparticles deposited in the TB and AL regions of a human lung of a typical worker by adjusting the ion-trap voltage of the EAD.

Fig. 1 shows a schematic diagram of the EAD. Sampled particles are first passed through a small cyclone to remove particles with a diameter larger than 1.0 μm. The sampled aerosol flow (i.e., 2.5 lpm) is then split into two: one portion of the flow (i.e., 1.5 lpm) is directly introduced into the aerosol charging chamber, and the other portion of sampled flow (i.e., 1.0 lpm) is used as the carrier for unipolar ions, generated in the corona discharging chamber, after the particles and vapor contaminants are removed by HEPA and active carbon filters. The two split flows are impinged and mixed in the aerosol charging chamber. Particles exited from the charging chamber are passed through an ion trap, with the voltage set at 20 V, before the electrical charges carried by particles are measured in an aerosol electrometer of Faraday cage type downstream of the ion trap. Different from the EAD, the NSAM has the built-in feature of adjusting the applied ion-trap voltage to correlate the NSAM readouts with the total surface area concentration of nanoparticles deposited in TB and AL regions of a human lung of a typical worker. It is worth noting that the functions of components used in the EAD or NSAM are essentially the same as those used in the early generation of electrostatic devices for particle size measurement.

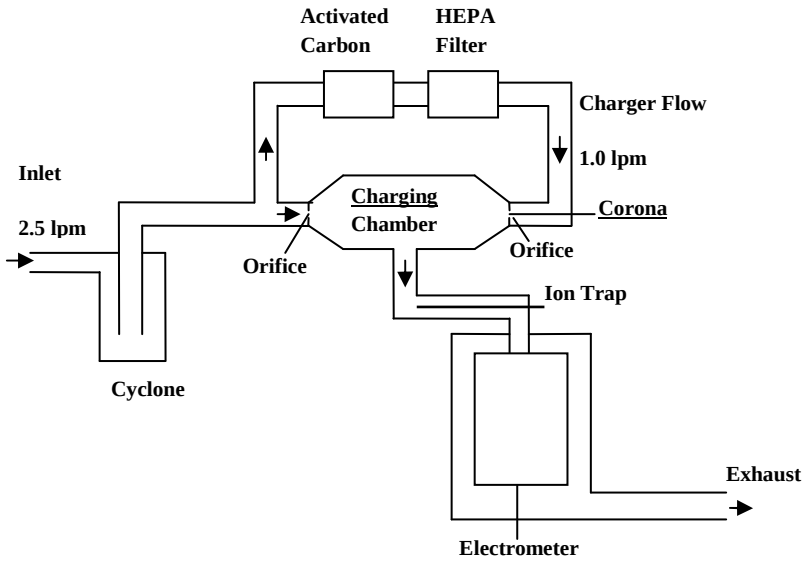

Figure 1 Schematic diagram of the Electrical Aerosol Detector (EAD) or Nanoparticle Surface Area Monitor (NSAM)

It is thus possible to convert an EAD or NSAM into a particle sizer with the feature of variable ion-trap voltage. Such a sizer may not offer a size distribution measurement with high size resolution, but it will meet the demands of the applications of industrial hygiene and exposure studies. Several efforts in a similar direction have been reported recently for the application of measuring particulate emission from diesel engines.

A system consisting of a unipolar diffusion charger, similar to that used in an EAD, with an aerosol electrometer (TSI model 3068A) and an Ultrafine Condensation Particle Counter (UCPC, TSI model 3025A) has been proposed to obtain particle size distributions (Park et al. 2007a). The group proposed a method for predicting the particle mean diameter and size distribution, providing the sizes of particles are in unimodal and lognormal distribution. The total number concentration of particles was given by the

UCPC measurement. The geometric standard deviation of the particle size distribution was further assumed as 1.5, which may be varied in different measurements. The proposed technique requires pre-knowledge of the geometric standard deviation of sampled particles. Further, the use of the bulky UCPC may be not convenient for the industrial hygiene and exposure studies, and the proposed method could retrieve the size distributions of sampled particles only in the unimodal, log-normal distribution functional format. Following the same strategy, a recent study (Park et al. 2007b) further proposed to use a system consisting of two unipolar chargers with two aerosol electrometers to obtain the size distributions of sampled particles. The proposed method has the benefit of not using a UCPC and consequently reduces the cost of having one aerosol system for particle size distribution measurement. The limitations of the proposed system are the same as those mentioned for the former study. The proposed methodology further limits the lower size detection limit to 70 nm due to the fact that the dominant charging mechanism of both chargers is diffusional as the particle size is reduced.

In this study we explored the idea of using an EAD (or NSAM) for nanoparticle size distribution measurement without the limitations inherent in the above-reviewed studies. We first evaluated the average electrical charges of particles passing through the EAD charger, using monodisperse particles with ion-trap voltages varying from 20 to 2500 V. We also proposed an empirical model to correlate the measured average charges on test particles with the parameter of Z_p*V, where Z_p is the particle electrical mobility and V is the ion-trap voltage. A data reduction scheme was then proposed to retrieve the particle size distribution from the EAD readouts as the ion-trap voltage stepped from 100 to 2500 V. In the scheme, the functional format of particle size distribution was assumed

to be log-normal for each mode in an entire size distribution but the number of the modes in a particle size distribution was not limited. A numerical criterion was used to best fit the simulated EAD readouts to experimental ones, thereby obtaining the count median diameter (*CMD*), geometric standard deviation (σ_g), and total particle number (N_t) of each mode in an entire size distribution.

Experimental Setups and Procedures

Setup for average charge evaluation

Fig. 2 is a schematic diagram of the experimental setup to characterize the average electrical charges on monodisperse particles after passing through the EAD charger. A constant-output, home-made atomizer was used to produce polydisperse NaCl particles with sizes ranging from 20 to 200 nm. The mean size of test particles was varied by using the NaCl aqueous solutions with volume concentrations ranging from 0.01% to 1%. The flow rate output from the atomizer was 4.0 lpm when the compressed air was at 30 psig. Droplets produced by the atomizer were passed through a Po^{210} radioactive neutralizer to minimize electrical charges on the droplets, and through a silicon-gel diffusion dryer to remove water from the droplets. A differential mobility analyzer (DMA, TSI Model 3081) was used downstream of the polydisperse aerosol generation system to classify particles with test diameters. Prior to being introduced to the DMA the produced particles were passed through a Kr^{85} radioactive particle charger, ensuring a well-defined charge distribution on particles to be classified (Knutson and Whitby 1975). The DMA was operated at the aerosol flow rate of 0.8 lpm and sheath flow rate of 8.0 lpm. To reduce the electrical charge level on classified particles, a second Po^{210}

radioactive neutralizer was used at the DMA monodisperse aerosol exit. The prepared monodisperse particle stream was then split into two: one stream was introduced to an Ultrafine Condensation Particle Counter (UCPC, TSI model 3025A) for particle number concentration measurement; the other was introduced to the EAD (TSI model 3070A) for obtaining the EAD readout at different ion-trap voltage settings.

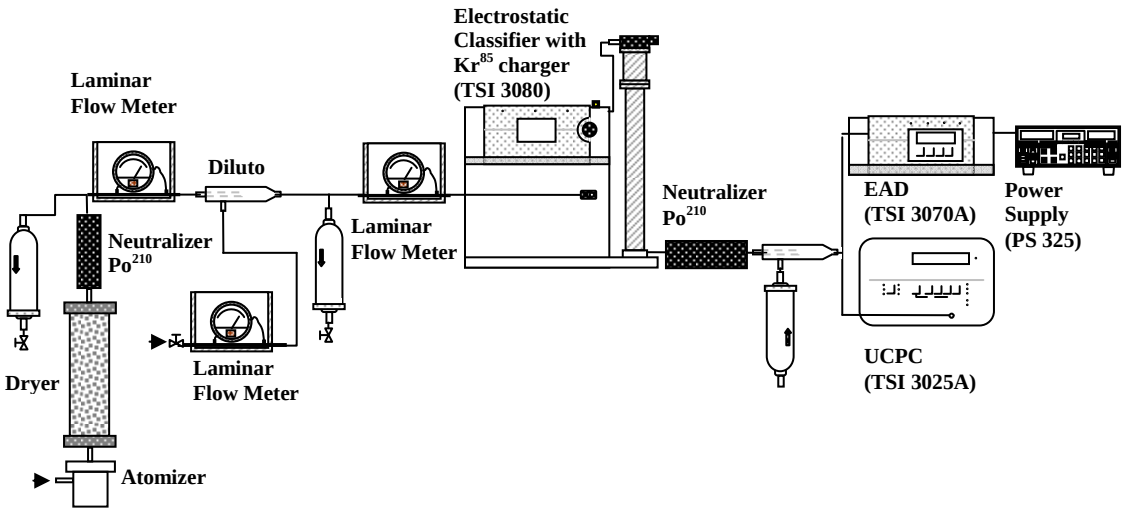

Figure 2 Experimental setup for the measurement of average electrical charge on monodisperse particles after passing through EAD charger and ion trap

Experimental setup for verifying the use of the EAD as a sizer

Fig. 3 shows the experimental setup for collecting data to verify the feasibility of using the EAD as a nanoparticle sizer. For unimodal particle size distributions, the particle-generation system described in the above section was used. For bimodal particle size distributions, a second particle generation system was added into the setup. The second system consisted of a high-temperature tube furnace (CM Furnace 1730-20HT) and a temperature-quenching chamber. Particle material was placed in a ceramic boat, located in the middle of the furnace tube. At a high temperature setting on the furnace,

the particle material in the ceramic boat evaporated and its vapor was carried by the carrier gas. At the furnace tube exit the carrier gas was cooled by mixing it with gas at room temperature. The evaporation-and-condensation process generates polydisperse nanoparticles with mean electrical mobility sizes ranging from 10 to 30 nm (Scheibel and Porstendorfer 1983; Gleiter 1989). In the aerosol generation system nitrogen gas with a flow rate of 2.0 lpm was used as vapor carrier. The flow rate of the carrier gas was controlled by a needle valve and laminar flow meter prior to its introduction into the tube furnace. To vary the mean size of generated particle size distribution, the tube furnace temperature was varied from 1000 °C to 1200 °C for Ag particles. Particles produced by the two generation systems were well mixed before the use as challenge particles. After passing through a mixing-type dilutor, the challenge particle stream was split into two: one stream was introduced to the EAD and the other to an SMPS (TSI Model 3936) to measure the size distribution of test particles. During the course of SMPS measurement, the EAD ion-trap voltage setting was stepped from 100 to 2500 V, with a step size of 100 V. At each ion-trap voltage step the EAD readouts was averaged for 10 seconds. One shall notice that the averaging time for each voltage setting can be varied, depending on the signal-to-noise ratio. The selection of 10-second averaging time for all the ion-trap voltage steps was set for the cases of low signal-to-noise ratio and for the experimental convenience. For both unimodal and bimodal particle size distributions, the concentration of the test aerosol was varied in the mixing-type dilutor.

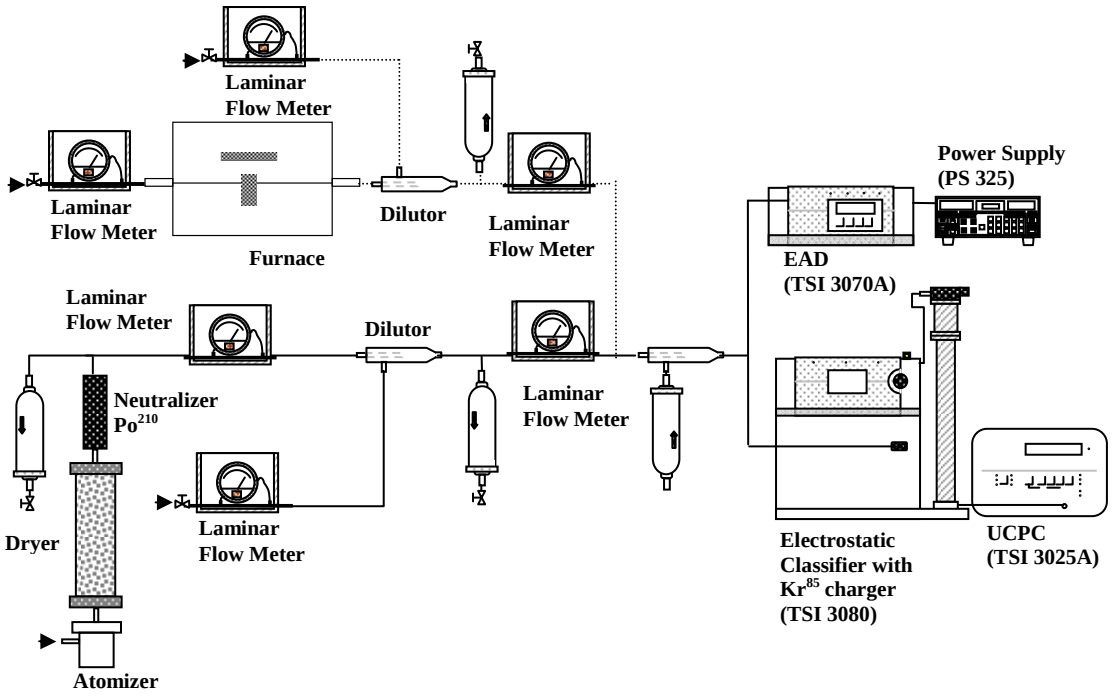

Figure 3 Experimental setup for the verification of using EAD as a submicron-sized particle sizer

Average Charge Calculation and Data Reduction Scheme

Calculation of average electrical charges on monodisperse particles

For obtaining the average charges on monodisperse particles, the concentration of test monodisperse particles was measured by a UCPC, while the electrical current carried by test particles after the EAD charger and ion trap was measured by the EAD. The average charge after ion trap q_{avg} on test particles was then calculated as

$$q_{avg}(d_p) = \frac{I}{N(d_p)eQ_{in}}, \quad (1)$$

where I is the charged particle current measured by the EAD, $N(d_p)$ is the particle concentration measured by the UCPC, Q_{in} is the volumetric flow rate of aerosol entering the mixing chamber in the EAD charger, and e is the charge on an electron ($1.6*10^{-19}$ C).

Size distribution reduction scheme

With the data of average electrical charges on particles passing through EAD charger, we could set up the relationship between the particle size distribution and the EAD readout. In the data reduction scheme, the functional format of the number size distribution of sampled particles was assumed to be log-normal for each mode in an entire size distribution. In the case of unimodal size distributions, they can be mathematically expressed as

$$N(\ln d_p) = \frac{N_t}{\sqrt{2\pi}\ln\sigma_g}\exp\left(\frac{-(\ln d_p - \ln CMD)^2}{2\ln^2\sigma_g}\right), \quad (2)$$

where $N(lnd_p)$ is the number of particles with a diameter of lnd_p, entering the EAD; N_t is the total number concentration; *CMD* is the geometric mean diameter; and σ_g is the geometric standard deviation, assumed to be less than 3.0. In the calculation, particles in the size range from 1 nm to 1 μm were divided into 48 size channels (32 channels per decade in log scale). The total electrical current carried by the particles (C) is then calculated as

$$C = eQ_{in}\sum_{d_p=1nm}^{1\mu m} N(d_p)q_{avg}(d_p). \quad (3)$$

The best-fit values of three parameters (i.e., *CMD*, σ_g, and N_t) in the log-normal distribution function are obtained by minimizing the following function.

$$\chi(\mathrm{C}MD, \sigma_\mathrm{g}, N_t) = \frac{\sum_{i=1}^{m}|C_i - M_i|}{m}, \quad (4)$$

where M_i is the EAD readout at a specific ion-trap voltage setting, pA; C_i is the corresponsive calculated value; and *m* is the number of data points.

For the cases of bimodal size distribution, the following mathematical expression was used:

$$N(\ln d_p) = \frac{rN_t}{\sqrt{2\pi}\ln\sigma_{g1}}\exp\left(\frac{-(\ln d_p - \ln CMD_1)^2}{2\ln^2\sigma_{g1}}\right) + \frac{(1-r)N_t}{\sqrt{2\pi}\ln\sigma_{g2}}\exp\left(\frac{-(\ln d_p - \ln CMD_2)^2}{2\ln^2\sigma_{g2}}\right) \quad (5)$$

where r is the ratio of the total particle number concentration in the first mode to that in an entire bimodal size distribution, N_t is the total number concentration of particles in the entire size distribution, CMD_1 and CMD_2 are the geometric mean diameters of two modes in a bimodal size distribution, $\sigma_{g1}$and σ_{g2} are the geometric standard deviations of two modes. The convergent criterion for the best-fitting of particle current at different ion-trap voltages is the same as that used for unimodal size distribution. It is worth noting that the scheme can be easily generalized for the case when the number of modes in an entire size distribution is more than two, although only the expressions for unimodel and bimodal size distributions are presented herein.

Results and Discussion

The average electrical charges on individual particles

Fig. 4a shows the average electrical charge of NaCl particles at an ion-trap voltage of 20 V. The size and number concentration of test particles range from 20 to 200 nm and from $1.6*10^3$ to $3.2*10^4$ #/cm^3, respectively. The linear relationship between average charge and particle size is evident in Fig. 4a. A linear curve was then applied to best fit the collected data. The average charge curves at several other selected ion-trap voltage settings are shown in Fig. 4b. For a given ion-trap voltage, the relationship

between average electrical charge and particle size does not seem to be linear. In general the curve slope for particles with diameters smaller than 100 nm is lower than that for large particles at a given ion-trap voltage. From the average charge data shown in Fig. 4b it is difficult to retrieve the average electrical charges on particles of an arbitrarily selected particle size when an EAD ion-trap voltage is given. To overcome the difficulty, we attempted to collapse the average electrical charge curves at different ion-trap voltages into one.

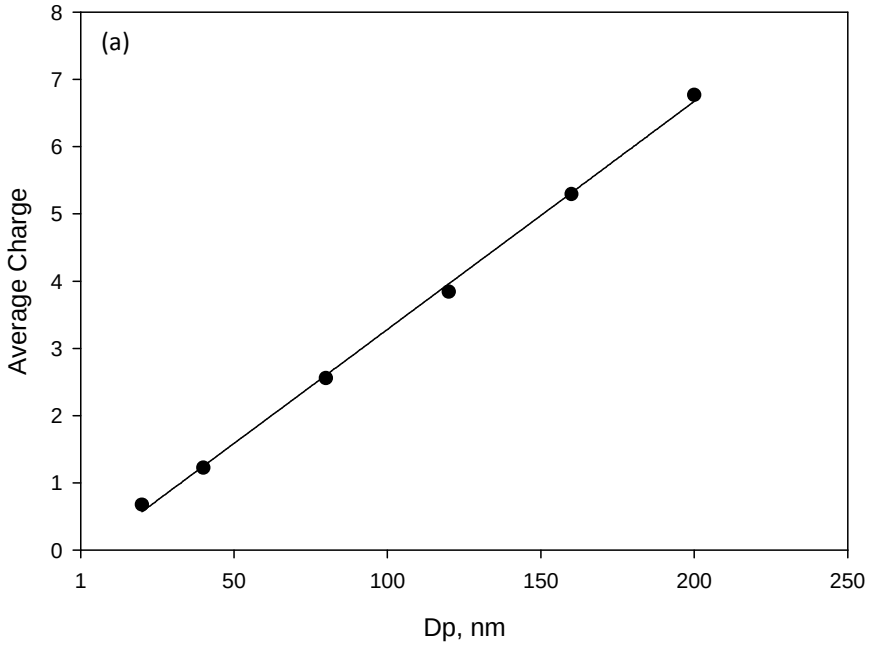

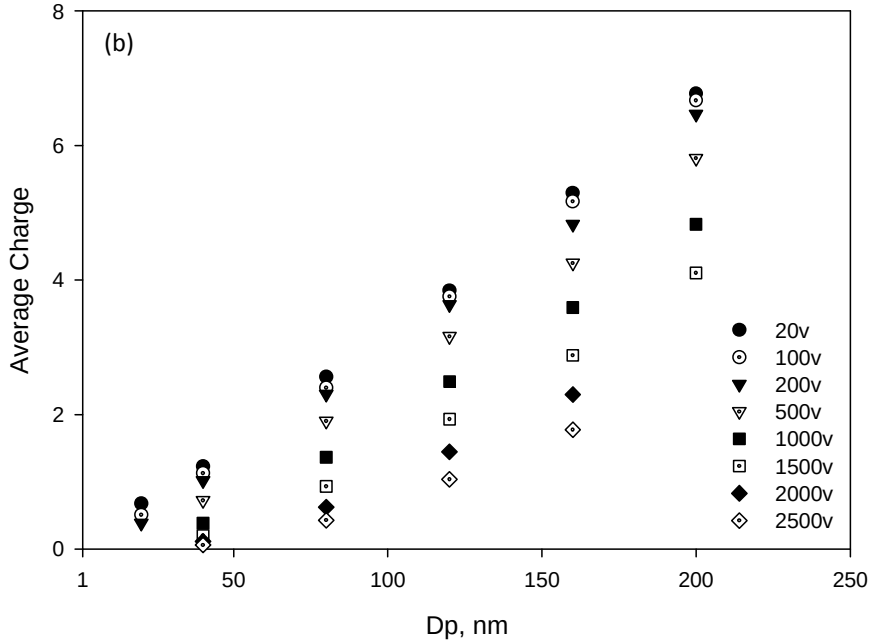

Figure 4 Average charges of NaCl particles, passing through both EAD charger and ion trap, as a function of particle size for the cases of (a) 20 V ion-trap voltage; and (b) other selected ion-trap voltage settings

To accomplish the task, we normalized the average electrical charges at different ion-trap voltages with the data when the ion trap was set at 20 V. Instead of using the particle size, we used Z_p*V as the abscissa, where V is the ion-trap voltage and Z_p the particle electrical mobility, given by

$$Z_p = \frac{neC_c}{3\pi\eta d_p} \tag{6}$$

in which n is the particle electrical charge, C_c the Cunningham correction factor, η the gas viscosity.

Fig. 5 shows the normalized average charge of particles as a function of Z_p*V. Z_p was calculated by assuming the particles carried an average electrical charge the same as

that at the ion-trap voltage of 20 V. As shown in Fig. 5, all the average electrical charge curves at different ion-trap voltages collapse into one. The result is expected because the operational principle of the ion trap in the EAD is essentially the same as that of an electrical precipitator. Using the particle trajectory analysis given by Knutson and Whitby (1975), the penetration of charged particles through an electrical precipitator should be a function of Z_p*V. Moreover, the relationship between the particle penetration and Z_p*V should be linear for an ideal electrical precipitator. However, as shown in Fig. 5, the relation of normalized average charges vs. the Z_p*V parameter is not perfectly linear. This finding may be due to the imperfect construction of the ion trap as compared with that of ideal precipitator. Nonetheless, the monotonic relationship between the normalized average charges and Z_p*V is clearly evidenced. To best fit the normalized curve of average charge, we divided the entire Z_p*V range into two segments and used a different equation for each segment: for values of Z_p*V less than $1.0*10^{-4}$, the normalized average charge was fitted with a linear function of the Z_p*V parameter; for values of Z_p*V larger than $1.0*10^{-4}$, the data were fitted with an exponential curve.

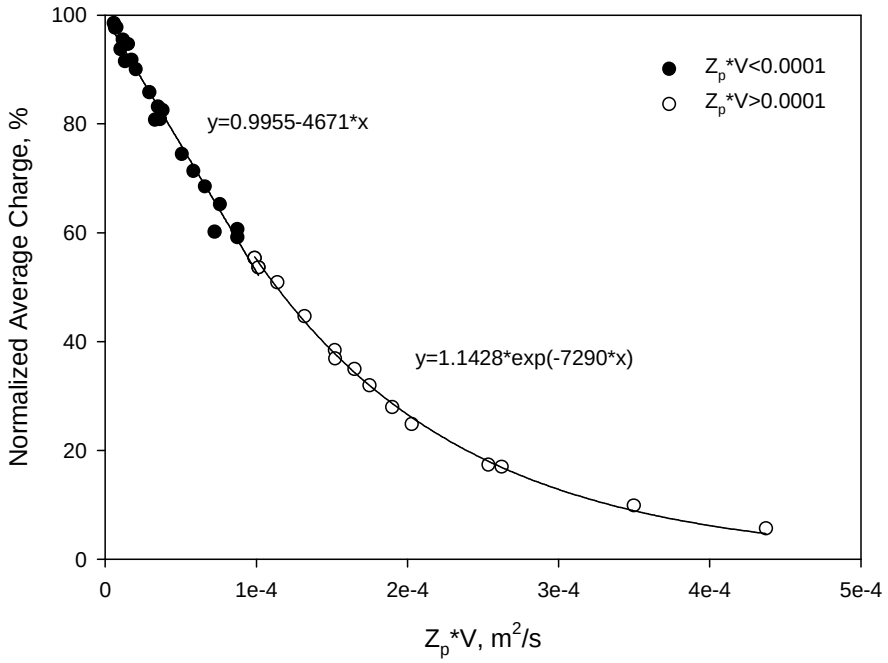

Figure 5 Normalized average charge of NaCl particles, past through the EAD charger and ion trap, as a function of the parameter of Z_p*V; where Z_p is the electrical mobility of particles carrying electrical charges the same as those at the ion-trap voltage of 20 V, and V is the ion-trap voltage

With Figs. 4 and 5 the following calculation procedure was used to retrieve the average electric charges of particles at a specific ion-trap voltage and particle size: for a given particle size d_p, the average electrical charges of particles at 20 V ion-trap voltage was first obtained from Fig. 4. The electric mobility, Z_p, of the particles was calculated based on Eq. (6). With the calculated value of Z_p*V the normalized average charges of particles was then obtained from Fig. 5 for a given ion-trap voltage. The average electrical charges of particles of the given size and at the given ion-trap voltage was finally calculated by multiplying the average electrical charges at 20 V ion-trap voltage with the normalized average charges.

Verification of the proposed data-reduction scheme

Figs. 6 - 8 compare the unimodal particle size distributions measured by the SMPS and recovered by the proposed data-reduction scheme for three different cases. The SMPS data are NaCl particles having geometric mean diameters of 103.2, 59.7, and 39.6 nm, geometric standard deviations of 1.67, 1.62, and 1.69, and total concentrations of, $8.08*10^5$, $1.48*10^6$, and $2.97*10^6$ #/cm^3, respectively. For NaCl particles with a geometric mean diameter of 103.2 nm (shown in Fig. 6), the retrieved particle size distribution with σ_g of 1.8 agrees well with that measured by the SMPS. The retrieved geometric mean diameters of particle size distributions for the other two cases (i.e., Figs. 7 and 8) are slightly smaller than those measured by the SMPS. The σ_g for particle size distributions, obtained by the proposed EAD method, are 1.6 and 1.9 for test particles with σ_g of 1.67 and 1.69, respectively. The σ_g difference is probably because of inaccuracy of average charge data for particles less than 40 nm. The lowest particle size used in the experimental for measuring average charges on monodisperse particles was 20 nm. However, the geometric mean diameter of polydisperse NaCl particles, produced from our aerosol generator, was about 40 nm for classifying test monodisperse particles with a diameter less than 40 nm. Using the DMA to classify particles with diameters less than 40 nm with the above-mentioned polydisperse particles can result in the non-negligible portion of classified particles having larger particle sizes and multiple electrical charges. As a result, the derived average charges on classified particles may be higher than those in reality. Consequently, the mean particle size of the retrieved particle size distribution has the tendency to move to a smaller particle size when a significant portion of sampled particles has diameters less than 40 nm.

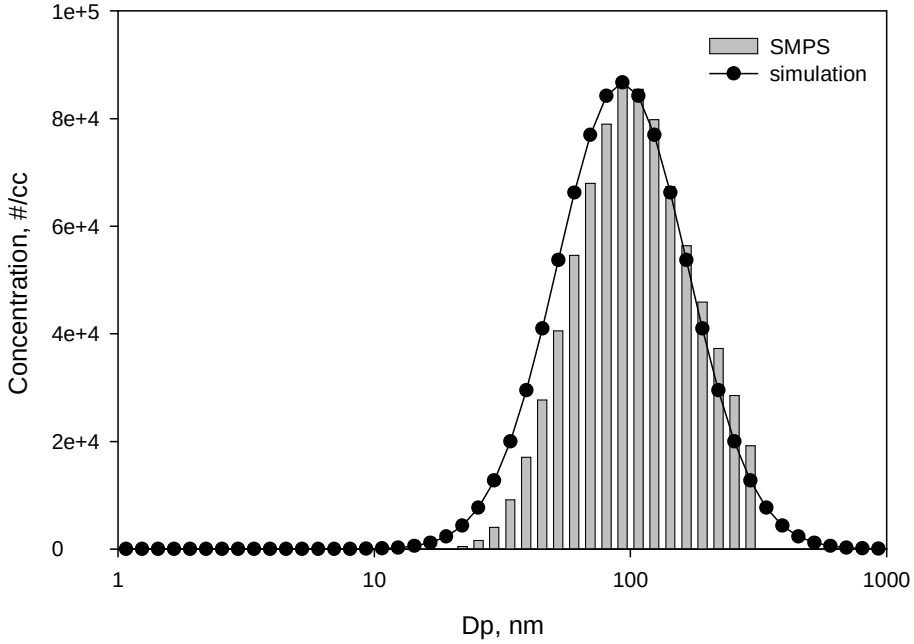

Figure 6 Comparison of unimodal particle size distributions measured by SMPS and retrieved by the proposed data-reduction scheme for the case of particles with geometric mean diameters of 103.2 nm

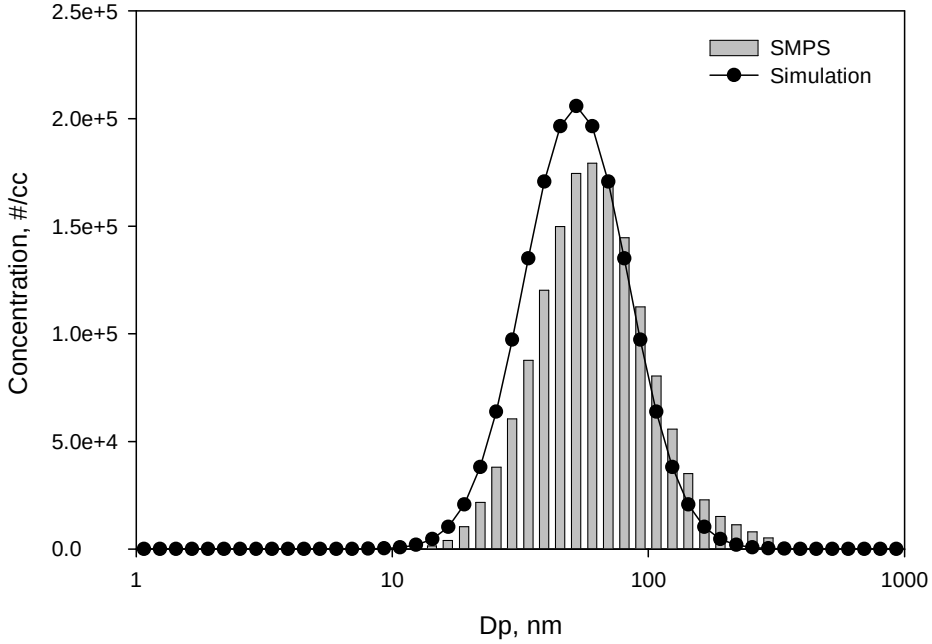

Figure 7 Comparison of particle size distributions measured by SMPS and retrieved by the proposed data-reduction scheme for the case of particles with geometric mean diameters of 59.7 nm

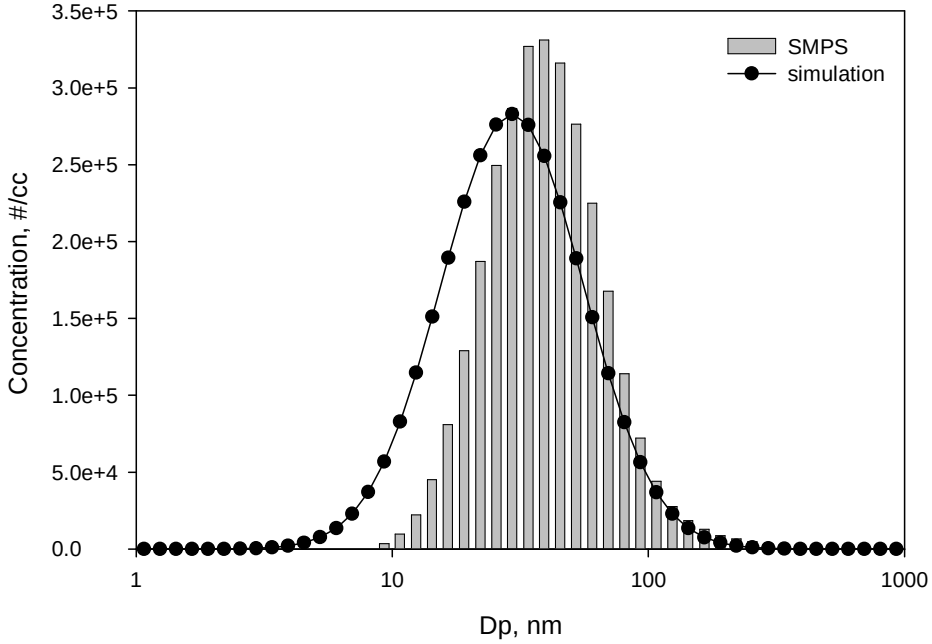

Figure 8 Comparison of unimodal particle size distributions measured by SMPS and retrieved by the proposed data-reduction scheme for the case of particles with geometric mean diameters of 39.6 nm

Fig. 9 shows the comparison of bimodal particle size distributions measured by SMPS and recovered by the proposed data-reduction scheme. The proposed scheme could in general retrieve the characteristics of actual particle size distribution, although the number concentration of particles in each SMPS size bin is lower than that obtained by the proposed scheme. In this case, the small-sized mode in the bimodal test particle size distribution was Ag particles, generated by the evaporation-and-condensation process, and the large-sized mode of the distribution was NaCl particles, generated by the home-made atomizer. In the data-reduction scheme, the average electrical charge curve used was for NaCl particles. The average electrical charge of Ag particles is expected to

be higher than that of NaCl particles because of the much larger dielectric constant of Ag particles. It may be the key reason leading to a higher number of particles in each size bin of the recovered particle size distribution since the average charge curve used in data reduction scheme is for NaCl particles.

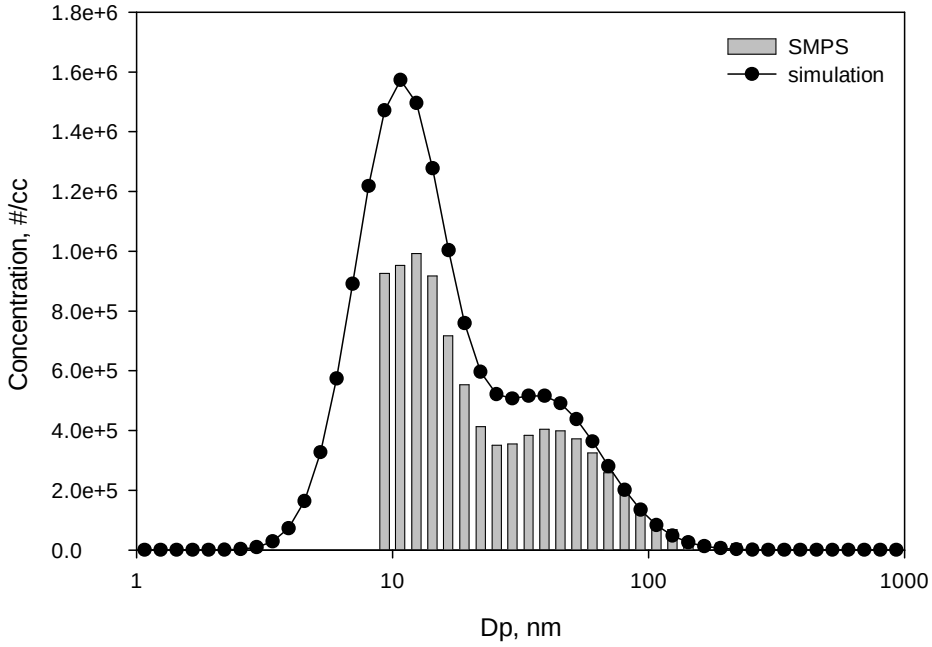

Figure 9 Comparison of bimodal particle size distributions measured by SMPS and retrieved by the proposed data-reduction scheme

To distinguish the unimodal from bimodal size distribution of particles to be analyzed one could use the geometric standard deviation σ_g as an indicator, suggested by Woo et al. (2001). The particle size distribution is most likely to be bimodal if the geometric standard deviation σ_g, retrieved from the data-reduction scheme with the assumption of unimodal size distribution, is more than 2.5. The minimal numbers of voltage steps needed for unimodal and bimodal size distribution measurements by the

proposed EAD method are at least three and seven, respectively. We however recommend to step at least four ion-trap voltage setting for unimodal size distribution and at least eight voltages for bimodal size distribution measurements. The total scan time for each size distribution measurement is therefore 1-2 minutes, assuming the 10-second data averaging for each ion-trap voltage step.

Summary

In conclusion, we have proposed a new and simple strategy to measure the size distributions of submicron-sized particles using a commercially available EAD or NSAM. The proposed strategy was inspired by the fact that the configuration of the EAD is similar to that of an electrical mobility analyzer of the early generation. To explore the feasibility of the strategy, we first characterized the average electrical charges on particles exiting the EAD charger, using monodisperse NaCl particles with diameters ranging from 20 to 200 nm. In this experiment, the ion-trap voltage was set at 20 V for excess ion removal. The linear relationship between the average electrical charges on particles and the particle size was found experimentally. The experiment also measured the average electrical charges on particles at different ion-trap voltage settings. The average charge curves were then summarized into one by normalizing average charges at different ion-trap voltages by those at the ion-trap voltage of 20 V and using the parameter of Z_p*V as the abscissa, where Z_p is the electrical mobility of particles carrying average charges the same as those at the ion-trap voltage of 20 V, and V is the ion-trap voltage. A curve fitting was proposed to best fit the normalized average charge curve.

A simple data-reduction scheme was also proposed to retrieve the particle size distribution from the EAD readouts as a function of the ion-trap voltage, stepped from 100 to 2500 V. In the data-reduction scheme, the functional format of the number size distribution of particles was assumed to be log-normal for each mode in an entire size distribution. The number of the modes in a particle size distribution was not limited. A criterion was also proposed to best fit the simulated EAD readouts to experimental ones by varying the count median diameter (*CMD*), geometric standard deviation (σ_g), and total particle number (N_t) of each mode in the presumed lognormal particle size distribution. By comparing particle size distributions measured by SMPS with those recovered from the EAD readouts, the proposed data-reduction scheme can quantitatively recover the unimodal particle size distributions of particles, and qualitatively retrieve the characteristics of bimodal particle size distributions. From the comparison, it is also concluded that the proposed strategy can be further improved by better measurement of average charges on particles with diameters less than 40 nm and by taking into consideration the particle material.

At last one shall notice that the proposed method does not intend to replace those based on the DMA techniques. The accuracy and sensitvity of particle size measurement by the proposed method can not compete with that measured by scanning mobility particle sizers (SMPSs). It is because of the material dependence of aerosol charging and the sensitivity of aerosol electrometer used in EAD and NSAM. The proposed technique merely offers an economical way to roughly measure the size distribution of particles when SMPSs are not available and the general information on the size distribution of

particles is critical for the interpretation of the particle integral parameters monitored by EAD or NSAM.

References

[1] Donaldson K, Li XY, MacNee W (1998) Ultrafine (nanometer) particle mediated lung injury. J Aerosol Sci 29(5-6):553-560

[2] Fissan H, Trampe A, Neunman S et al (2007) Rationale and principle of an instrument measuring lung deposition area. J Nanoparticle Res 9:53-59

[3] Gleiter H (1989) Nanocrystalline Materials. Prog Mater Sci 33:223-315

[4] Hinds W (1999) Aerosol technology: properties, behavior, and measurement of airborne particles. Wiley-Interscience, New York

[5] Keskinen J, Pietarinen K, Lehtimaki M (1992) Electrical Low Pressure Impactor. J Aerosol Sci 23:353

[6] Knutson EO, Whitby KT (1975) Aerosol Classification by Electric Mobility: Apparatus, Theory, and Applications. J Aerosol Sci 6:443-451

[7] Martin SJ, Granstaff VE, Frye GC (1991) Characterisation of a quartz crystal microbalance with simultaneous mass and liquid loading. Anal Chem 63:2272-2281

[8] Oberdörster G (1996) Significance of particle parameters in the evaluation of exposure-dose–response relationships of inhaled particles. Particul Sci Technol 14(2):135-151

[9] Oberdörster G, Oberdörster E, Oberdörster J (2005) Invited review: nanotechnology: an emerging discipline evolving from studies of ultrafine particles. Environ Health Perspect 113(7):823-839

[10] Park D, Kim S, An M et al (2007a) Real-time measurement of submicron aerosol particles having a log-normal size distribution by simultaneously using unipolar diffusion charger and unipolar field charger. J Aerosol Sci 38(12):1240-1245

[11] Park D, An M, Hwang J (2007b) Development and performance test of a unipolar diffusion charger for real-time measurements of submicron aerosol particles having a log-normal size distribution. J Aerosol Sci 38(4):420-430

[12] Patashnick H, Rupprecht EG (1991) Continuous PM-10 measurements using the Tapered Element Oscillating Microbalance. J Air Waste Manage Assoc 41:1079-1083

[13] Scheibel HG, Porstendorfer J (1983) Generation of Monodisperse Ag and NaCl Aerosol with Particle Diameters between 2 and 300 nm. J Aerosol Sci 14:113-126

[14] Stoltzenburg MR, McMurry PH (1991) An ultrafine aerosol condensation nucleus counter. Aerosol Sci Tech 14:48-65

[15] Wilson WE, Han HS, Stanek J et al (2004) Use of Electrical Aerosol Detector as an Indicator for the Total Particle Surface Area Deposited in the Lung. Symposium on air quality measurement methods and technology sponsored by the Air and Waste Management Association. Research Triangle Park, NC. Paper #37

[16] Woo KS, Chen DR, Pui DYH et al (2001) Use of continuous measurements of integral aerosol parameters to estimate particle surface area. Aerosol Sci Tech 34:57-65

Curriculum Vita

Lin Li

EDUCATION

Ph. D. in Energy, Environmental, and Chemical Engineering	08/2005 - 12/2010
Washington University in St. Louis, MO, USA	
Master of Science in Environmental Engineering	08/2003 - 07/2005
Tsinghua University, Beijing, China	
Bachelor of Science in Environmental Engineering	08/1999 - 07/2003
Tsinghua University, Beijing, China	

AWARDS AND HONORS

- Charles Buescher Jr. Scholarship, Washington University 2005 - 2007
- Tsinghua Friend -- Shunde Wu Married Couple Scholarship 2000 - 2002
- Tsinghua University Excellent Student Scholarship 1999 - 2000

PROFESIONAL SOCIETIES

- American Association for Aerosol Research (AAAR)

PUBLICATIONS

Accepted Journal Articles

1. Jiangang Zhu, Sahin Kaya Ozdemir, Yun-Feng Xiao, **Lin Li**, Lina He, Da-Ren Chen, Lan Yang, On-chip Single Nanoparticle Detection and Sizing by Mode Splitting in an Ultra-high-Q Microresonator, *Nature Photonics*, 4:46-49, 2010.
2. Ta-Chih Hsiao, Da-Ren Chen, **Lin Li**, Paul Greenberg, Kenneth W. Street, Development of a Multi-stage Axial Flow Cyclone, *Aerosol Sci. Technol.*, 44(4):253-261, 2010.
3. **Lin Li**, Da-Ren Chen, Chaolong Qi, Pramod S. Kulkarni, A Miniature Disk Electrostatic Aerosol Classifier for Personal Nanoparticle Sizers, *J. Aerosol Sci.*, 40(11): 982-992, 2009.
4. **Lin Li**, Da-Ren Chen, Perng-Jy Tsai, Evaluation of an Electrical Aerosol Detector (EAD) for the Aerosol Integral Parameter Measurement, *J. Electrostatics*, 67(5): 765-773, 2009.
5. **Lin Li**, Da-Ren Chen, Perng-Jy Tsai, Use of an Electrical Aerosol Detector (EAD) for Nanoparticle Size Distribution Measurement, *J. Nanoparticle Research*, 11(1): 111-120, 2009.

6. Christopher Hogan Jr., **Lin Li**, Da-Ren Chen, Pratim Biswas, Estimating aerosol particle charging parameters using a Bayesian inversion technique, *J. Aerosol Sci.*, 40(4): 295-306, 2009.
7. **Lin Li**, Jiming Hao, Jingnan Hu, Analysis and Prediction of the Influence of Energy Utilization on Air Quality in Beijing, *Frontiers of Environmental Science & Engineering in China*, 1(3): 1-6, 2007.
8. Weiling Li, **Lin Li**, Da-Ren Chen, A New Deconvolution Scheme for the Retrieval of True DMA Transfer Function from Tandem DMA Data, *Aerosol Sci. Technol.*, 40(12): 1052-1057, 2006.
9. Jiming Hao, Litao Wang, **Lin Li**, Jingnan Hu, Xuechun Yu, Air Pollutants Contribution and Control Strategies of Energy-use Related Sources in Beijing, *Science in China Series D: Earth Sciences*, 48(SII): 138-146, 2005.
10. **Lin Li**, Jiming Hao, Jingnan Hu, Analysis and Prediction of Air Quality Influence from Energy Utilization in Beijing, *China Environmental Science*, 25(6): 746-750, 2005 (in Chinese).

Journal Articles Submitted or in Preparation

11. **Lin Li**, and Da-Ren Chen, Performance Study of a DC-corona-based Particle Charger for Charge Conditioning, *submitted to Journal of Aerosol Science.*
12. **Lin Li**, Paul S. Greenberg, Kenneth Street, and Da-Ren Chen, Study of a Magnetic Filter System for the Characterization of Particle Magnetic Property, *submitted to Journal of Aerosol Science.*
13. **Lin Li**, Paul S. Greenberg, Kenneth Street, and Da-Ren Chen, Magnetic Susceptibility Characterization of Lunar Dust Simulants, *submitted to Journal of aerospace engineering.*
14. **Lin Li**, and Da-Ren Chen, Investigation of Aerosol Charging Using Pen-Ray UV Lamps, *in preparation.*

CONFERENCE PRESENTATIONS

1. **Lin Li**, Da-Ren Chen, Chaolong Qi, Pramod S. Kulkarni, A Miniature Disk Electrostatic Aerosol Classifier for Personal Nanoparticle Sizers, the 2009 Annual Conference of the AAAR, Minneapolis, MN, October 2009.
2. **Lin Li**, Da-Ren Chen, Preliminary Study of a UV Aerosol Charger, the 2009 Annual Conference of the AAAR, Minneapolis, MN, October 2009.
3. **Lin Li**, Da-Ren Chen, Study of a New Corona-Based Unipolar Aerosol Charger, the 2008 Annual Conference of the AAAR, Orlando, FL, October 2008.
4. **Lin Li**, Da-Ren Chen, Perng-Jy Tsai, Use of Electrical Aerosol Detector for Particle Size Distribution Measurement, the 3rd International Symposium on Nanotechnology, Occupational and Environmental Health, Taipei, Taiwan, August 2007.
5. **Lin Li**, Da-Ren Chen, Perng-Jy Tsai, Evaluation of TSI Electrical Aerosol Detector for Measuring the Surface Area of Particles Deposited in Human Lungs, the 5th Asian Aerosol Conference, Kaohsiung, Taiwan, August 2007.